LASER-INDUCED ROTATIONAL DYNAMICS AS A ROUTE TO MOLECULAR FRAME MEASUREMENTS

by

VARUN MAKHIJA

B.A., Drew University, Madison, NJ, 2008.

AN ABSTRACT OF A DISSERTATION

submitted in partial fulfillment of the
requirements for the degree

DOCTOR OF PHILOSOPHY

Department of Physics
College of Arts and Sciences

KANSAS STATE UNIVERSITY
Manhattan, Kansas

2014

Abstract

In general, molecules in the gas phase are free to rotate, and measurements made on such samples are averaged over a randomly oriented distribution of molecules. Any orientation dependent information is lost in such measurements. The goal of the work presented here is to a) mitigate or completely do away with orientational averaging, and b) make fully resolved orientation dependent measurements. In pursuance of similar goals, over the past 50 years chemists and physicists have developed techniques to align molecules, or to measure their orientation and tag other quantities of interest with the orientation. We focus on laser induced alignment of asymmetric top molecules.

The first major contribution of our work is the development of an effective method to align all molecular axes under field-free conditions. The method employs a sequence of nonresonant, impulsive laser pulses with varied ellipticities. The efficacy of the method is first demonstrated by solution of the time dependent Schrödinger equation for iodobenzene, and then experimentally implemented to three dimensionally align 3,5 difluoroiodobenzene. Measurement from molecules aligned in this manner greatly reduces orientational averaging. The technique was developed via a thorough understanding and extensive computations of the dynamics of rotationally excited asymmetric top molecules.

The second, and perhaps more important, contribution of our work is the development of a new measurement technique to extract the complete orientation dependence of a variety of molecular processes initiated by ultrashort laser pulses. The technique involves pump-probe measurements of the process of interest from a rotational wavepacket generated by impulsive excitation of asymmetric top molecules. We apply it to make the first measurement of the single ionization probability of an asymmetric top molecule in a strong field as a function of all relevant alignment angles. The measurement and associated calculations help identify

the orbital from which the electron is ionized. We expect that this technique will be widely applicable to ultrafast-laser driven processes in molecules and provide unique insight into molecular physics and chemistry.

LASER-INDUCED ROTATIONAL DYNAMICS AS A ROUTE TO MOLECULAR FRAME MEASUREMENTS

by

VARUN MAKHIJA

B.A., Drew University, Madison NJ, 2008.

A DISSERTATION

submitted in partial fulfillment of the
requirements for the degree

DOCTOR OF PHILOSOPHY

Department of Physics
College of Arts and Sciences

KANSAS STATE UNIVERSITY
Manhattan, Kansas

2014

Approved by:

Major Professor
Vinod Kumarappan

Copyright

Abstract

In general, molecules in the gas phase are free to rotate, and measurements made on such samples are averaged over a randomly oriented distribution of molecules. Any orientation dependent information is lost in such measurements. The goal of the work presented here is to a) mitigate or completely do away with orientational averaging, and b) make fully resolved orientation dependent measurements. In pursuance of similar goals, over the past 50 years chemists and physicists have developed techniques to align molecules, or to measure their orientation and tag other quantities of interest with the orientation. We focus on laser induced alignment of asymmetric top molecules.

The first major contribution of our work is the development of an effective method to align all molecular axes under field-free conditions. The method employs a sequence of nonresonant, impulsive laser pulses with varied ellipticities. The efficacy of the method is first demonstrated by solution of the time dependent Schrödinger equation for iodobenzene, and then experimentally implemented to three dimensionally align 3,5 difluoroiodobenzene. Measurement from molecules aligned in this manner greatly reduces orientational averaging. The technique was developed via a thorough understanding and extensive computations of the dynamics of rotationally excited asymmetric top molecules.

The second, and perhaps more important, contribution of our work is the development of a new measurement technique to extract the complete orientation dependence of a variety of molecular processes initiated by ultrashort laser pulses. The technique involves pump-probe measurements of the process of interest from a rotational wavepacket generated by impulsive excitation of asymmetric top molecules. We apply it to make the first measurement of the single ionization probability of an asymmetric top molecule in a strong field as a function of all relevant alignment angles. The measurement and associated calculations help identify

the orbital from which the electron is ionized. We expect that this technique will be widely applicable to ultrafast-laser driven processes in molecules and provide unique insight into molecular physics and chemistry.

Table of Contents

List of Figures

List of Tables

v

Acknowledgments

Over the course of the last six and a half years I have been lucky to learn a great deal of physics, both in and out of the lab. For this I am most grateful to my Advisor, Dr. Vinod Kumarappan, whose wealth of knowledge and depth of creativity never cease to surprise me. He has always patiently, and with clarity, provided answers to even the most inane questions. I owe a large chunk of my knowledge acquired in the lab to the senior student in our group, Xiaoming Ren. His intuition for solving problems in the lab and getting the experiment going is astounding. I can only hope some part of it has been transfered to me. I would also like to thank him for putting up with me as I don't believe I have spent more time with any other individual over the course of my PhD. His patience is truly remarkable. I would also like to acknowledge Matthew Rothfuss , an undergraduate student who was part of our group and happily helped with numerous tedious technical issues. Both Ren and Matthew have surpassed their roles as colleagues and have become friends who I'm sure I will meet again in the future. I would alos to thank the new member of our group, Aram Vajdi. Aram is a fast learner and great to work with. I must also acknowledge our collaborators. Dr. Carlos Trallero and his group member Jan Tross. The high harmonic generation experiment introduced in the last chapter could not have been performed without their efforts, and Jan has now taken the reins of the experiment. Dr. Martin Centurion and Jie Yang whose work comprises the more significant part of our collaboration on diffractive imaging of aligned molecules. The experiment on electronic waveackets presented in the last chapter was the brainchild of Dr. Artem Rudenko. My numerous fruitful discussions with him have greatly enhanced my understanding of strong field physics. His effervescence and enthusiasm are infectious. I am also grateful to the technical staff at James R. Macdonald Lab — Al Rankin, Mike Wells, Bob Krause and Scott Chainey — for their help. Being a

graduate student I spent the majority of my time in the lab, and was notorious for ignoring or forgetting the world outside it. Off course such a situation is not sustainable for over six years without the strong support of close friends. I am grateful to Adrian and Christian Madsen, for often pulling me out of the lab and for sometimes bringing food to the lab to make sure I didn't skip meals. Also Mohammad Zohrabi (Mo) and Amy Rouinfar for organizing numerous road trips into the Rocky Mountains. Fellow classmates and rommates for four years, Shuo Zeng and Bachan Lomsadze for their companionship. And last but not least my friends and family at home in India for their long distance support, even though they did not have the slightest idea about what I was doing.

Chapter 1

Introduction

The primary goal of the work presented in this thesis is to develop techniques that will allow fully differential measurements of physical processes in molecules in the gas phase. Our specific concern will be untangling how the particular process depends on the orientation of the molecules. Consider, for instance, photoionization – the removal of an electron from a molecule by light. The probability of this process occurring depends on the orientation of the molecule relative to the polarization of the light[1]. Further, the emission direction of the electron and the probability of it being emitted at a particular energy depend on the molecular orientation as well. The measurement of the direction of emission and energy of the electron for all possible molecular orientations relative to the polarization of the light constitutes a fully differential measurement. In general, these measurements are challenging since gas phase molecules are in a state of perpetual motion, the vigor of which depends on the temperature of the gas.

Techniques have been developed to make such measurements with linear molecules[2,3,4]. For non-linear molecules the success of these techniques depends on the rotational symmetry of the molecule, on the basis of which they can be classified as symmetric or asymmetric tops. Asymmetric tops have three distinct principal moments of inertia, two of which are equal for a symmetric top. While the techniques developed for linear molecules prove somewhat

successful for symmetric tops[5,6] the discussion to follow will make it clear that extending these techniques to more complex systems proves intractable in some cases, or at least highly non-trivial[7,8,9,10]. As we tend towards the study of polyatomic molecules it becomes less probable to have two axes with equal moments of inertia, making the development of feasible molecular frame measurement techniques for asymmetric tops an important problem. With these facts in mind, we focus on asymmetric top molecules.

Even for such species, several experiments in the molecular frame have already been conducted[11,12,13,14]. However, these experiments are carried out in the presence of a laser pulse used to hold the molecules in place, and therefore the measurement is performed on a perturbed molecular system. To avoid this complication we focus on making measurements under field-free conditions.

The first step on the route to making these measurements is a thorough examination of the field-free dynamics of a gas of rotationally excited asymmetric top molecules. In the limit where the molecules are impinged upon by a laser pulse of significantly shorter duration than the time scale of molecular rotation, the laser pulse kicks them into rotation causing them to line up with the polarization axis after the pulse has passed. This technique has been widely used to study processes in diatomic molecules[15,16,17] though its extension to asymmetric tops has proven to be challenging[7,8,9]. In what follows we trace the development of and need for molecular frame measurements. We then discuss contemporary work using laser-induced alignment and the technique of photon-photoelectron coincidence spectroscopy in order to motivate the specific avenues followed in this thesis.

1.1 The Development of Molecular Frame Measurements

The initial need for making molecular frame measurements appears to have arisen in physical chemistry. Dudley Herschbach and others in the field of reaction dynamics were at-

tempting to study the fundamental physical processes involved in chemical reactions. They approached the problem using atomic and molecular beam techniques developed by Otto Stern and used to confirm the existence of spin (the renowned Stern-Gerlach experiment[18]). In their pioneering experiment Herschbach and his colleges collided beams of potassium (K) and methyl iodide (CH_3I) and measured the yield of the KI product at different ejection angles[19]. They found that the scattering was markedly anisotropic with the product scattering off most favorably at 83° with respect to the K velocity vector. However the C-I bond of the CH_3I molecule was randomly oriented causing any orientation dependant or *steric* effects to average out.

With the goal of being able to measure such steric effects Kramer and Bernstein used a hexapole electric field to focus CH_3I molecules of a given orientation[20]. This appears to have been the first successful attempt to orient a molecule. Shortly after its invention the hexapole technique was used by Brooks and Jones to measure that the rate of production of KI is strongly dependent on the orientation of CH_3I relative to the K beam[21]. The results of these experiment generated considerable interest in the possibility of measuring the angular distribution of photoelectrons in the molecular frame. Early theoretical studies[1] showed the sensitivity of such distributions to the electronic structure of the molecule. The culmination of these studies was the first experimental measurement of photoelectrons ejected from oriented molecules by Kaesdorf *et al.*[22]. They used the hexapole technique to orient CH_3I molecules and ionize them with a 21.2 eV lamp source. They measured a strong asymmetry in the photoelectron currents parallel and anti-parallel to the C-I bond. A portion of their results are reproduced in Fig. 1.1, where the closed circles represent the asymmetry measured with oriented molecules, and the open circles with the hexpole voltage applied and an additional randomizing field. The hexapole technique has since been used in numerous steriochemical studies[23,24,25].

Despite its utility the hexapole technique has some serious limitations, perhaps the most serious is that it applies only to symmetric top molecules. Additionally, as indicated in the

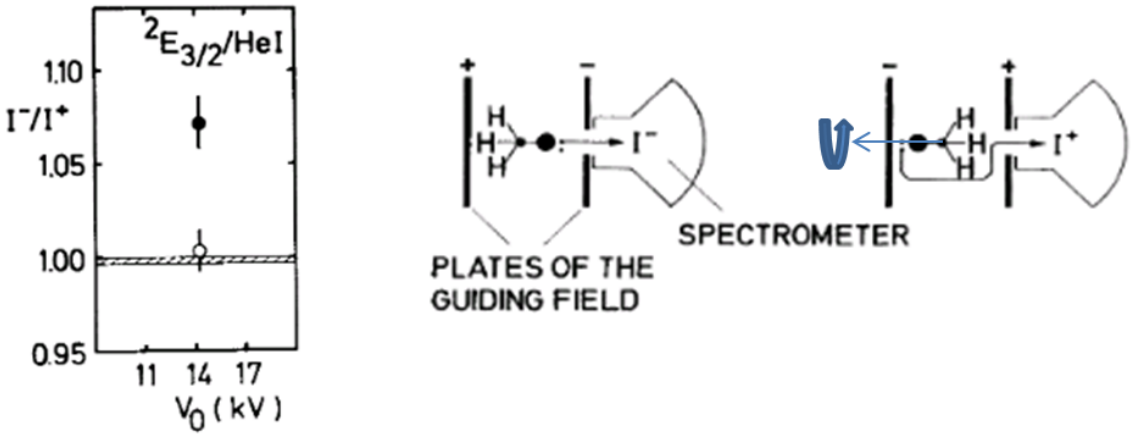

Figure 1.1: *Shown here are some results from Kaesdorf* et al.[22]. *The left panel shows the asymmetry in electron ejection measured between configuration shown in the right panel,*V_0 *is the hexapole voltage.*

I^+ configuration in Fig. 1.1, while the C-I bond axis is oriented the molecule is still able to spin like a top about this axis; we approach the molecular frame but don't quite get there. A nearly parallel experimental development, also stemming from Herschbach's work would later overcome these hurdles. At the time Herscbach's PhD student R.N. Zare was studying molecular photodissociation[26]. The result of their work and related experimental studies[26] was the detailed understanding of photodissociation, and an understanding of the limits of the 'axial recoil approximation' – the assumption that the fragment will recoil in the direction of the bond axis. The axial recoil approximation allows the use of photoelectron-photion coincidences to make molecular frame measurements that are not limited to a single axis[5], nor to symmetric tops[10].

The experimental technique of photoelectron-photoion coincidence spectroscopy was developed as a tool to study photodissociation[27]. This method allowed the measurement of the momenta (energy and emission direction) of photoions in coincidence with photoelectrons of a specific energy. The energy of the photoelectrons indicated the state of the molecular ion from which the dissociation initiated enabling state specific studies of the fragmentation

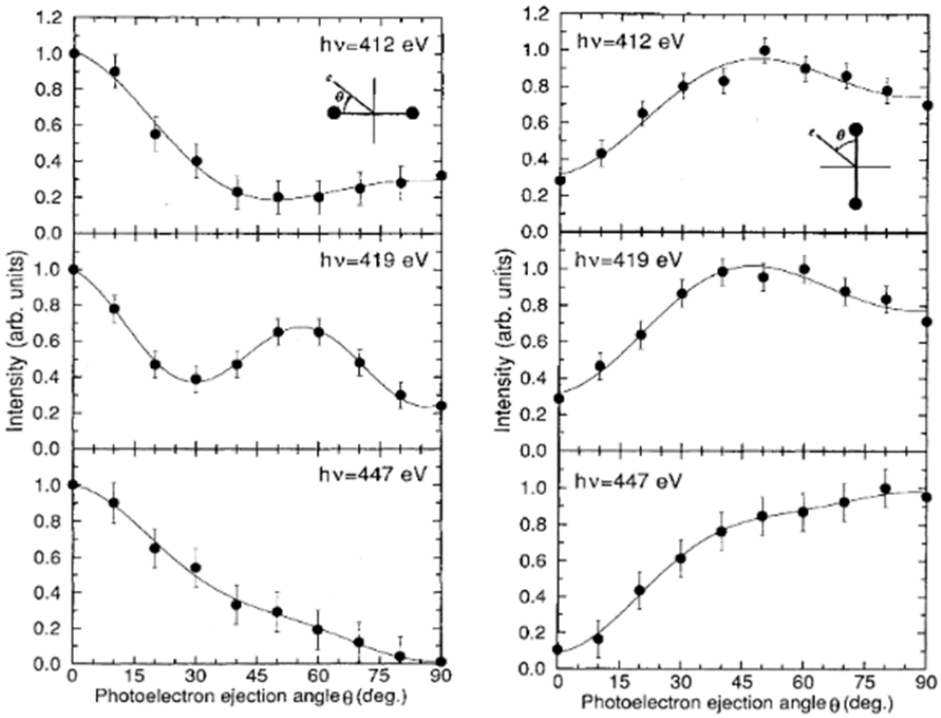

Figure 1.2: *MFPADs for K-shell photoionization from N_2 measured by Shigememasa* et al.[2]*. The left panel is for molecules aligned parallel to the polarization of the light and the right panel for molecules aligned perpendicular.*

process[28]. The same technique was later used by Golovin *et al.* to measure molecular frame photoelectrons angular distributions (MFPAD)[29]. Soon after Shigemasa *et al.* measured MFPADS for an electron ionized from the inner most shell of N_2 with near 400 eV photons from a synchrotron[2]. The fragmentation following removal of the electron occurs much faster than molecular rotation, the key requirement for the axial recoil approximation to hold[26]. The ejection direction of the atomic fragments with respect to the polarization of the light could therefore be assumed to be the direction of the molecular axis. With the emission angle and energy of the photoelectrons being measured, all the information required to reconstruct the MFPAD is collected. Some of their results are shown in Fig. 1.2, where the left and right panels show MFPADs with the molecule aligned along and perpendicular to the polarization of the light. By analyzing the varying shapes of the PADs the authors

were able to determine the orbital angular momentum of the photoelectrons.

While it is not limited to symmetric top molecules and with the measurement of multiple fragment momenta allows reconstruction of the full molecular orientation[5], the coincidence technique presents its own set of limitations. Most evidently, it is necessary that the molecule dissociate in order to measure the direction of alignment of the molecular axis. This excludes the set of physical processes in which the molecule does not fragment such as the emission of radiation from an excited neutral molecule or the removal of a valence electron leaving behind a stable ion. Additionally, even if the molecule does fragment, accurate reconstruction of the molecular orientation depends on the of validity of the axial recoil approximation, the range of which is known to be limited[26,28]. In the following section we review the development of the method of laser-induced alignment, which overcame some of these limitations.

1.1.1 Laser Induced Alignment

The advent of lasers producing pulses with durations between picoseconds and femtoseconds allowed intensities of focused beams to reach $\approx 10^{14}$ to 10^{15} W/cm^2. At these intensities field strengths are on the order of 0.1 atomic units(a.u.), 1 a.u. being the electric field felt by an electron 1 Bohr Radius away from a proton. These intensities are sufficient to remove valence electrons from atoms and molecules even with photon energies much lower than the binding energy[30]. Experimentalists studying photodissocaition began doing so at these intensities, and it was noticed by Normand *et al.*[31] that the laser pulses tended to align the molecules with the polarization axis *prior* to fragmentation. Friedrich and Herschbach were able to explain the physical mechanism causing this alignment and suggested its use for the alignment of neutral molecules at non-ionizing intensities ($\approx 10^{10}$W/cm^2)[3]. An experimental demonstration by Kim and Felker followed fast afoot[32].

Friedrich and Herschbach found that the alignment was induced via the nonresonant polarizability of the molecule[3]. Since the permanent dipole is independent of the laser electric field and the molecule does not rotate significantly over a laser cycle, its interaction

cycle averages to zero. However the strong electric field induces a dipole in the molecule which oscillates with the electric field. The cycle averaged potential felt by a rigid linear molecule as a result of this interaction is[3,32]

$$V = -\frac{E_0^2}{4}\left[(\alpha_{\parallel} - \alpha_{\perp})\cos^2\theta + \alpha_{\perp}\right], \tag{1.1}$$

where θ is the angle between the electric field and the molecular axis, E_0 is the maximum field strength experienced by the molecule and $\alpha_{\parallel}$ and $\alpha_{\perp}$ are polarizability components along and perpendicular to the molecular axis respectively. The function $\cos^2\theta$ has minima at 0° and 180° forming a double welled potential. The lower states in this potential can be approximated as harmonic oscillators, with the molecular axis oscillating about the minimum position. In both the initial theoretical and experimental papers[3,32] the duration of the pulses used was significantly longer (∼ns) than the timescale of molecular rotation(∼ps), allowing the field-free states to adiabatically transform into the aligned field dressed states permitting the approximation that the field in Eq. 1.1 is static. In this case the peak alignment is reached at the peak of the laser pulse. Classically one might think of the field as slowly torquing the molecules into alignment.

Following these initial demonstrations the sub-field of molecular alignment progressed rapidly. At this point it is necessary to clarify some terminology. Fig. 1.3 shows distributions of iodobenzene with different degrees of alignment and orientation. For 1D alignment, a single molecular axis is constrained to be parallel to one space fixed axis, with the axes not necessarily pointing in the same direction. The first panel of Fig. 1.3 in which the iodine atom is allowed to point 'up' or 'down' and the molecular plane is free to rotate is called 1D aligned. This is the kind of alignment discussed above. The second panel, in which the iodine atom is forced to point up is an example of 1D orientation. In this case the molecular axis is constrained to point in the same direction as one space fixed axis. 1D orientation was first achieved by the hexapole focusing technique as shown in Fig. 1.1. The third panel, in which the C-I axis is only aligned but the molecular plane is fixed to plane of the page is an

example of 3D alignment. Here all three molecular axes must be parallel to corresponding lab fixed axes, without necessarily pointing in the same direction. The last panel in which the C-I axis is oriented and the molecular plane is fixed shows 1D orientation combined with 3D alignment, which brings the molecular frame into the lab for iodobenzene. In general the number of axes that need to be aligned or oriented to make the lab and molecular frames coincide depends on the symmetry of the molecule.

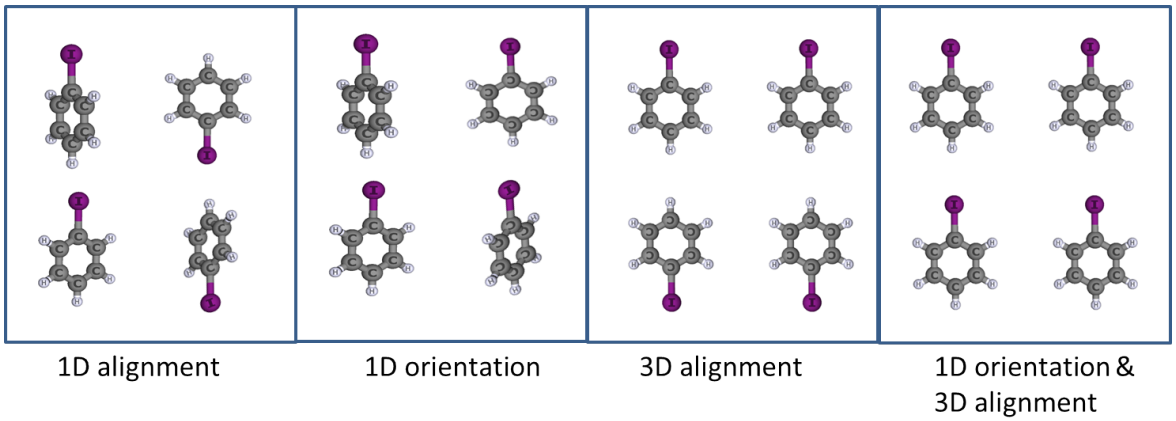

Figure 1.3: *Some of the alignment distributions accessible by laser-induced alignment*

Soon after the initial demonstration of adiabatic alignment experiments in Henrik Stapelfeldt's group demonstrated very strong confinement of the molecular axis for numerous rotationally cooled molecular targets[33,34]. Using an elliptically polarized, intense laser pulse the group was able to demonstrate adiabatic 3D alignment of 3,4 dimbromothiophene[35]. These measurements were performed using the pump-probe technique developed by Ahmed Zewail[36]. The alignment pulse (the pump) was followed by a time delayed dissociating pulse (the probe) and the momenta of ejected fragments was used to estimate the degree of alignment. For asymmetric tops such as those dealt with in these experiments the interaction potential for both linearly and elliptically polarized light becomes significantly more complicated than Eq. 1.1. This will be examined in detail in the following chapters. While these results tend to show strong confinement of the molecules it is important to remember that it only persists in the presence of an intense laser pulse, which can certainly contaminate the results

of any further measurements made on the aligned distribution. For instance since most of these experiments are performed just below the threshold intensity for ionization putting the molecule in an electronically excited state will surely lead to ionization precluding any measurements aimed at understanding the dynamics of the excited state.

To overcome this Seideman proposed a method that is now termed *impulsive alignment*[37]. She suggested the use of a non-ionizing intense pulse of much shorter duration (∼fs) than the time scale of molecular rotation to excite a wave packet of angular momentum states. The interaction potential remains unchanged, and the squared cosine provides selection rules for transitions between states. Specifically the total angular momentum J can change by 2 and its projection on the polarization axis M must remain constant. Additionally the static field amplitude must be replaced by the time dependent field envelope of the pulse. Therefore, for the duration of the pulse a molecule starting in a specific J state continually exchanges angular momentum with the field in accordance with the selection rules such that by the end of pulse it finds itself in a broad superposition of angular momentum states. If phases of each component J state of the state distribution match up, the wave packet in the conjugate variable – the alignment angle – becomes narrow, resulting in alignment usually observed shortly after (∼ps) the pulse has gone. The molecules then continue to rotate away from alignment. However, due to the spacing of rotational levels the time dependent phases of the wave packet components periodically match up resulting in revivals of the initial alignment[38,39]. Revivals form the basis for rotational coherence spectroscopy (RCS)[40], a spectroscopic tool used to determine the structure of molecules. A great deal of what is know about revivals in asymmetric tops was learned through RCS[40]. The nature of rotational wave packets is discussed in detail in the next chapter.

Rosca-Pruna and Varkking first demonstrated laser-induced field-free 1D alignment with iodine as their test subject[41]. They were able to very clearly observe revivals of the initial alignment via pump-probe measurements of fragment ions over a long time window. The first scheme for field-free 3D alignment was proposed four years later by Underwood,

Sussman and Stolow[8]. After investigating a few possible avenues they concluded that two time delayed, perpendicularly polarized impulsive pulses would result in a 3D aligned distribution. The first pulse would align the most polarizable axis and the next pulse would arrive just before the peak of this alignment and spin the molecular plane into alignment. This method was experimentally demonstrated by Lee *et al.* the following year using sulfur dioxide as a test subject[9]. While the technique worked the degree of alignment achieved was not substantial. Additionally since the second pulse degraded the alignment of the most polarizable axis induced by the first, there was no clear route to enhancing the alignment.

An important contribution of the work presented in thesis was to break this impasse by developing a new technique to induce a high degree of field-free 3D alignment; comparable to that measured with the adiabatic technique[42]. The resultant aligned distribution can be used to probe the dynamics of the excited state in the fashion of the seminal experiment performed by Bisgaard *et al.*[17]; where an impulsively aligned linear molecule is pumped to an electronically excited and subsequently probed over a time window during which the alignment persists. Chapter 3 covers the theoretical development and experimental demonstration of the alignment technique. Here we note that while impulsively aligned molecules are field-free, they are in highly excited rotational states. This can perturb the ground and excited vibronic states as well. In the end the choice of method depends on the experiment in question and is a matter of the experimentalists discretion.

As the field of laser-induced alignment has progressed, it has also been applied to make measurements in the molecular frame. In the next section we present an example of such a measurement and provide further motivation for the work described in this thesis.

1.2 State of the Art Molecular Frame Measurements

We first describe a recent experiment by Wiliams *et al.*[5] in which cold target recoil ion momentum spectroscopy (COLTRIMS)[43] was used to make coincidence measurements. In

their experiment K-shell carbon electrons from methane (CH_4) were ionized using 295 eV light from a synchrotron. The subsequent relaxation of an electron in to the inner shell hole results in the ejection of an Auger electron. The relaxation process repeats resulting in triply charged methane which breaks rapidly into (H^+,H^+,CH_2^+) fragments all of which are measured in coincidence with the initially ejected electron. The fragmentation is rapid enough that the axial recoil approximation holds and the angular distribution of the electron can be reconstructed for every molecular orientation. Some of the results are shown in Fig. 1.4.

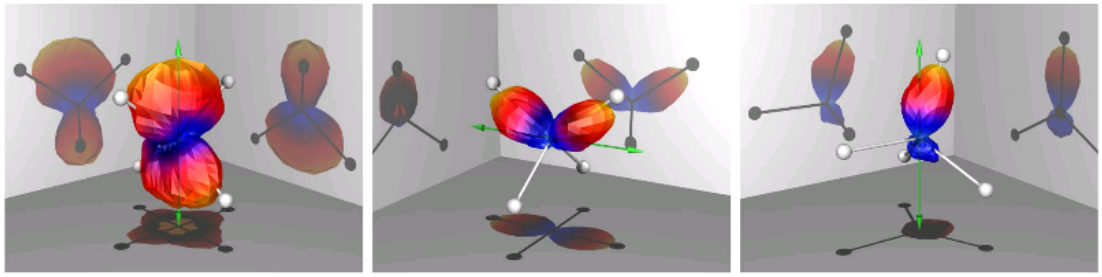

Figure 1.4: *MFPADs for K-shell photoionization from carbon in CH_4 for several orientations of the molecule relative to the laser polarization measured by Williams* et al.[5].

While the authors emphasize that the PAD averaged over all orientation bears a striking resemblance to the structure of the molecule, in principal these PADs contain a wealth of information about the *electronic* structure of molecule[44]. The shortfall of this experiment is that the same information cannot be extracted for ionization of the outer most electron, since this results in stable CH_4^+. This is the kind of ionization that occurs in intense fields with photon energies ∼1 eV. Theoretical analyses and numerical simulations show that the orientation dependent yield of the molecular ion for complex molecules in a strong field follows the shape of the orbital from which the electron is removed[45,46]. This can certainly not be measured using COLTRIMS, but can it be corroborated by measurements from aligned molecules?

Shown in Fig. 1.5 are measurements made by Hansen *et al.* of the orientation dependent

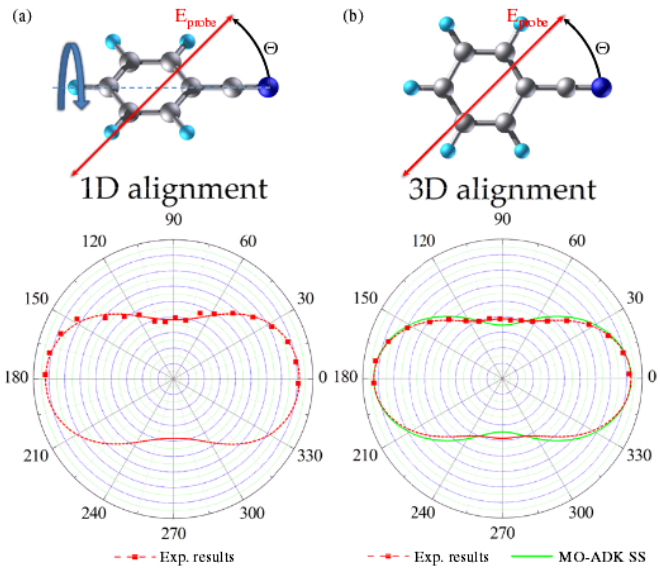

Figure 1.5: *The orientation depedndent ion yield for strong field ionization of (a) 1D oriented and (b) 1D oriented and 3D aligned benzonitrile as measured by Hansen* et al.*[13].*

yield of the benzonitrile molecular ion generated by valence ionization in an intense field[13]. As depicted in the cartoon drawings, in panel (a) the molecule is 1D aligned and in panel (b) it is 3D aligned. Note that even for case (b) the yield is measured only as a function of the angle between the molecular symmetry axis and the laser polarization axis. The reason for this is that even though the molecular plane is fixed the experimental geometry precludes *control* over it. It can only be fixed in the polarization plane, and therefore a fully angle resolved measurement cannot be made.

Therefore while in principal all molecular orientations can be accessed by coincidence measurements only dissociative processes can be measured, and even those must conform to the axial recoil approximation. On the other hand, while 3D alignment allows molecular frame measurements of non-dissociative processes all molecular orientations cannot be accessed. The solution to this dichotomy is the next important contribution of this thesis. We exploit the dynamics of rotational wave packets to measure the fully angle resolved yield for non-dissociative, strong field ionization of ethylene. To the best of our knowledge this is

the first such measurement. Furthermore the method developed is applicable to the large subset of processes that conform to the Born-Oppenheimer approximation (cf chapter 2, section 2.2). Chapter 5 covers the theoretical and experimental details of the method.

1.3 Summary and Conclusion

In this chapter we traced the development of molecular frame measurements from their beginnings in reaction dynamics. We emphasized important experimental techniques used to make these measurements, specifically photoelectron-phototion coincidence techniques and intense-laser-induced alignment. The adiabatic method of alignment, while producing strongly aligned distributions, cannot be used to measure excited state dynamics as the presence of the intense aligning pulse can ionize the excited state. Impulsive alignment on the other hand provides field-free aligned molecules which can be used to probe excited state dynamics. With this in mind we develop, in chapter 3, a method to achieve a high degree of field-free 3D alignment.

We also highlighted the essential drawbacks of both field-free 3D alignment and coincidence measurements. In the former all molecular orientations are not accessible due to experimental constraints and the latter cannot be used for non-dissociative measurements. In chapter 5 we develop and demonstrate an entirely new measurement technique that overcomes both these issues.

Chapter 2

Theoretical and Experimental Fundamentals

In this chapter we first examine the motion of a quantum mechanical asymmetric top. The chapter begins with a brief description of the classical motion, and moves briskly on to the Schrödinger equation for a quantum top. The solutions of this equation are discussed, and then an interaction with pulsed light is added to the Hamiltonian. The mechanism of this interaction and the ensuing rotational motion is examined in detail, as the understanding of these forms the foundation of all the following work.

We then describe the core experimental apparatus used for the experiments presented in later chapters. We describe the operation of a pulsed source of rotationally cooled molecules essential for controlled experiments with rotational wave packets. We also describe a spectrometer used to measure the momenta of charged particles emitted from the gas source as a result of interaction with an intense pulsed laser. Finally, the specifications and a brief description of the operation of the laser are provided.

2.1 What is an asymmetric top?

This discussion is adapted from David Tong's online lecture notes on classical mechanics[47].

An asymmetric top is the most general rigid body. Formally stated it is a rigid body with three distinct principal moments of inertia. We would be remiss in considering asymmetric tops as 'special' as numerous everyday objects - chairs, tables, tennis rackets - fall under this classification. A fundamental property of asymmetric tops is often demonstrated with the aide of a tennis racket. If held against the floor and spun about an axis passing through the handle, the racket will spin about this axis. If thrown up in the air in such a way that it rotates about an axis perpendicular to the racket face, it will again rotate obediently. However, any attempt to make it rotate about the axis in the plane of the racket face and perpendicular to the handle fails miserably and the racket begins to dance about somewhat chaotically.

This seemingly strange behavior can be predicted by the classical equations of motion for a free top - Euler's Equations.

$$I_x\dot{\omega_x} + \omega_y\omega_z(I_z - I_y) = 0 \tag{2.1}$$

$$I_y\dot{\omega_y} + \omega_z\omega_x(I_x - I_z) = 0 \tag{2.2}$$

$$I_z\dot{\omega_z} + \omega_x\omega_y(I_y - I_x) = 0, \tag{2.3}$$

where the I_j are the principal moments of inertia and the ω_j are angular velocities about the principal axes. Throughout this thesis small letters will label body fixed axes and capital letters space fixed axes. These equations are easily derived from the fact that the total angular momentum is conserved for a free top. Without having to solve these equations exactly, we may investigate the effect of a small perturbation $\alpha(t)$ to a top with angular velocity Ω about one of the principal axes, say the y-axis - $\omega_x = \alpha_x$, $\omega_y = \Omega + \alpha_y$, $\omega_z = \alpha_z$.

Ignoring quadratic terms, Euler's Equations then become

$$I_x\dot{\alpha_x} + \Omega\alpha_z(I_z - I_y) = 0 \tag{2.4}$$

$$I_y\dot{\alpha_y} = 0 \tag{2.5}$$

$$I_z\dot{\alpha_z} + \Omega\alpha_x(I_y - I_x) = 0. \tag{2.6}$$

From the above equations we can get the following second order differential equation in α_x,

$$I_x\ddot{\alpha_x} - \frac{\Omega^2}{I_z}(I_y - I_x)(I_z - I_y)\alpha_x = 0. \tag{2.7}$$

The solution of this equation is either periodic, or exponential depending on the sign of the product $(I_y - I_x)(I_z - I_y)$. In the case of a periodic perturbation the motion is stable with a small oscillation about Ω; the frequency of which depends on how asymmetric the top is, i.e. on how large the differences between the principal moments of inertia are. However, if $I_x < I_y < I_z$ or $I_z < I_y < I_x$, implying that Ω is about the intermediate principal axis, the perturbation grows exponentially resulting in the familiar chaotic dance of the tennis racket. This peculiar behavior translates to the quantum mechanical rotor as well, where it is expressed as a highly aperiodic and complicated energy level structure. This in turn leads to interesting and nonintuitive temporal evolution of a coherent wave packet of these energy states. As the understanding of this temporal evolution is the backbone of the work presented in this thesis, we conclude our discussion of classical tops here and switch gears to quantum mechanics for the remainder of this chapter.

2.2 The asymmetric rigid rotor in quantum mechanics

Under the Born-Oppenheimer Approximation[48,49,44] the wave function of a molecule can be separated into rotational, vibrational and electronic parts. We do not delve into the the mathematical details of the approximation here. Fundamentally it assumes that the nuclei

are at rest on the time scale of the motion of the orbiting electrons. Through out this thesis we assume the validity of the separation of the rotational and vibronic wave functions, with the rotational wave function being approximated as that of a rigid rotor. In this section we investigate the properties of such wave functions and their eigenvalues. Much of the material is sourced from Zare[50] and Van Winter[51].

2.2.1 The coordinate system

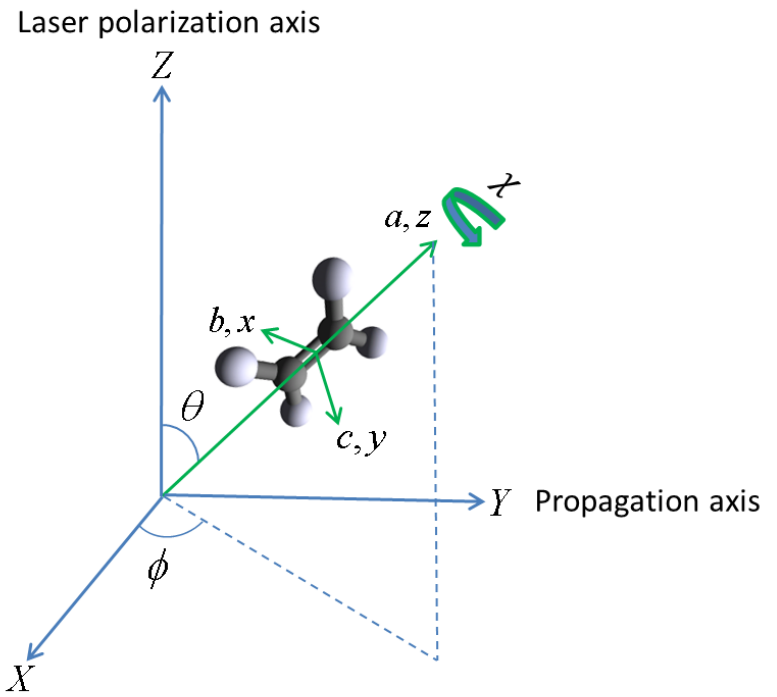

Figure 2.1: *A drawing of the coordinate system used throughout the thesis*

We use the usual definition of a general rotation in terms of the Euler angles, which are shown in Fig. 2.1. In accordance with standard notation we will refer to the principal axes as a,b and c; a being the axis of least moment of inertia, b the intermediate and unstable axis and c the axis of greatest moment of inertia as labeled in Fig. 2.1 for the ethylene molecule. The non-resonant interaction of the molecule with a laser, which will be our

primary concern, occurs through the molecular polarizability. For all molecules studied in this thesis the a axis will coincide with the most polarizable z axis, the b axis with the intermidately polarizable x axis and the c axis with the least polarizable y axis. For the angle χ, we choose a convention where $\chi = 0$ when the a-b plane coincides with the plane containing the both the a and Z axes.

Additionally, atomic units in which $\hbar$, the electron charge and mass e and m_e are set to 1 are used for all quantities unless specifically mentioned.

2.2.2 Rotational eingenstates and energies

We can begin by stating the Hamiltonian for a rigid rotor,

$$H_{rot} = \frac{J_a^2}{2I_a} + \frac{J_b^2}{2I_b} + \frac{J_c^2}{2I_c} = AJ_a^2 + BJ_b^2 + CJ_c^2. \tag{2.8}$$

Here the J_i are angular momentum operators representing the angular momentum about each principal axis and A, B and C are frequencies of rotation about each principal axis. In the case of a symmetric top, either $A = B$ and $J_a = J_b$ (oblate top) or $B = C$ and $J_b = J_c$ (prolate top), allowing two of the component angular momenta to be eliminated from the above equation in favor of the total angular momentum $\mathbf{J}^2$. Then $\mathbf{J}^2$, its projection on the space fixed axis J_Z^2 and the one remaining J_i^2 which we consider to be J_a^2 all commute with the Hamiltonian and therefore represent conserved quantities. Simultaneous eigenfunctions of these operators — $|JKM\rangle$ — are then also eigenfunctions of the Hamiltonian. Here J, K and M are eigenvalues of $\mathbf{J}^2$, J_Z^2 and J_a^2 and thus are conserved. However, since the J_i^2 do not commute with each other there is no obvious choice for eigenfunctions of H_{rot}. We proceed in the standard manner[50,51] and write the eigenfunctions as a linear superposition of the $|JKM\rangle$,

$$\Psi_{JM} = \sum_K c_K \left|JKM\right\rangle. \tag{2.9}$$

Representation	E	C_a^π	C_b^π	C_c^π
A	1	1	1	1
B_a	1	1	-1	-1
B_b	1	-1	1	-1
B_c	-1	- 1	1	1

Table 2.1: *Character table for the D_2 group*

The sum is only over K as the total angular momentum for a free top must be conserved and symmetry about the space fixed axis requires that M be conserved as well. Matrix elements of H_{rot} can be found in this basis using commutation relations between angular momentum components in the molecular frame, as presented in chapter 6 of Zare[50]. In doing so we find, as expected, that H_{rot} does not couple states with different J and M, and within a single J, M block only states with K different by two are coupled. Diagonalizing this matrix provides the coefficients c_K in the above expression, and hence the asymmetric top eigenfunctions.

We diagonalize the H_{rot} matrix numerically, since we need to solve the time dependent Schrödinger equation (TDSE) numerically to determine the rotational wave function after a laser pulse. However the diagonalization can be carried out analytically and is substantially simplified if the symmetry group of H_{rot} is considered. A rotation by π about the a,b or c axis transforms the principal axes back into themselves leaving H_{rot} unchanged. These three operations therefore commute with H_{rot} and along with the identity operator form its symmetry group[52] - the four group, D_2. Table 2.1 is the character table for this group where C_a^π, C_b^π and C_c^π are π rotations about the a,b, and c axes and E is the identity operator.

Each eigenstate of H_{rot} will generate an eigen value of ± 1 when acted on by a D_2 operator in accordance with one of the four representations A, B_a, B_b and B_c which are not coupled by H_{rot}. Consequently, if a symmetrized basis set is constructed from a linear superposition of the $|JKM\rangle$, H_{rot} can be subdivided into four smaller matrices each of which can be independently diagonalized providing eigenstates and energies of each representation. This procedure is carried out in detail by Zare[50] and Van Winter[51]. Our primary application of

the symmetry classification of the states will be to couple them with the appropriate nuclear spin states such that the total molecular wave function is appropriately symmetrized with respect to the exchange of identical atoms. This procedure will allow us to construct the thermal mixed state which represents our gaseous sample.

The symmetry class of a numerically calculated Ψ_{JM} can be determined by considering the oblate and prolate symmetric top limits - $\Psi_{JM} \longrightarrow |JK_1M\rangle, |JK_{-1}M\rangle$. K_{-1} and K_1 are symmetric top quantum numbers in the prolate and oblate limit respectively. For an oblate top the energy in a given J manifold decreases as a function of K, whereas for a prolate top it increases as a function of K. Therefore, for the asymmetric top the energy must increase with K_{-1} and decrease with K_1, requiring that $K_{-1} = 0, 1, 2...J$ and $K_1 = J, J-1, J-2...0$ with increasing energy. Using these the states of H_{rot} can be labeled by $\tau = K_{-1} - K_1$ which runs from $-J$ to J in order of increasing energy. Fig. 2.2 shows a generic energy level diagram for asymmetric tops with the corresponding oblate and prolate symmetric top energies on the left and right axes respectively.

Noting that K_1 is associated with rotation about the c axis and K_{-1} with rotation about the a axis, we can classify the symmetry of the state based on their parity. If both are even the state generates the A representation since in this representation all rotations generate the character 1 leaving the wave function unchanged. If both are odd the B_b representation is generated, since in this representation both C_a^π and C_c^π change the sign of the wave function. Similarly, if only K_1 is even the B_c representation is generated and if only K_{-1} is even the B_a representation is generated.With this, from fig. 2.2 we can deduce the representation of each state in order of energy and hence τ as given in table 2.2. Evidently if J is even the states can be classified in the order A, B_a, B_b, B_c with decreasing energy and τ, and in the opposite order if J is odd. We use this result to classify numerically calculated eigenstates of H_{rot} which are stored in order of increasing energy. This classification will be used in the next section to prepare the mixed state which will serve as the initial state for the TDSE describing the interaction of molecules with a laser field.

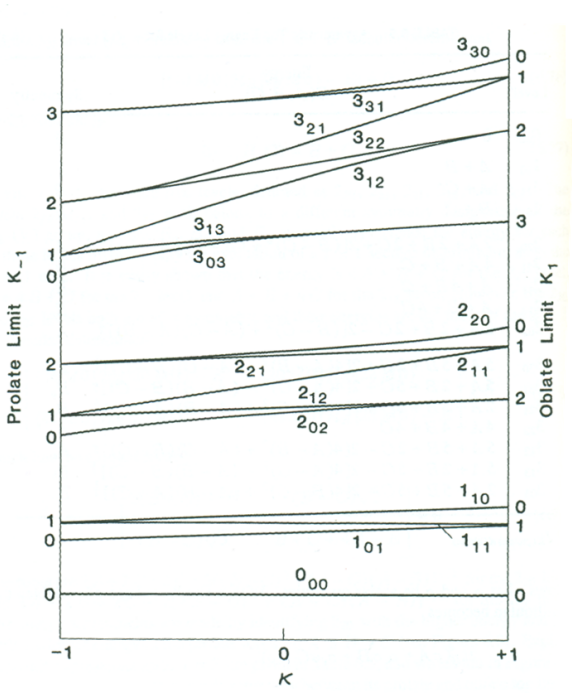

Figure 2.2: *Energy levels for an asymmetric top as a function of Ray's asymmetry parameter κ, where $\kappa = -1$ corresponds to a prolate symmetric top and $\kappa = 1$ to an oblate symmetric top. Reproduced from Zare*[50]

2.2.3 The quantum asymmetric rotor in a non-resonant laser field

In this section we examine the interaction of the quantum asymmetric rotor with a classical, pulsed laser field. The theoretical details are given here and details of the numerical code are left to appendix F.

The interaction is assumed to be non-resonant and occurring through the molecular dipole. The dipole can be written as

$$\mu_i = \mu_i^0 - \frac{1}{2}\alpha_{ij}E_j(t) \tag{2.10}$$

where μ_i^0 are components of the permanent dipole moment of the molecule and α_{ij} components of the polarizability tensor in the space fixed (Lab) frame defined by polarization

J,τ	Symmetry Representation
3,3	B_c
3,2	B_b
3,1	B_a
3,0	A
3,-1	B_c
3,-2	B_b
3,-3	B_a
2,2	A
2,1	B_a
2,0	B_b
2,-1	B_c
2,-2	A

Table 2.2: *The symmetry representations deduced from fig 2.2 for $J = 2$ and 3. As is evident the order of the symmetry representations is decided by the parity of J.*

components $E_i(t) = \sqrt{8\pi\alpha I_0(t)}\epsilon_i \cos\omega t$ of the electric field, ω being the central frequency of the pulse, α the fine structure constant, ϵ_i the weight of each polarization component and $I_0(t)$ the intensity envelope. The Einstein summation convention is always assumed unless otherwise stated. The above is a truncated Taylor expansion of the dipole as a function of the electric field, with terms after μ_i^0 representing the field induced dipole. We may ignore μ_i^0 as it does not follow the oscillating field of the laser and will be averaged out. The induced dipole interaction potential can then be written as

$$\begin{aligned} V &= \mu_i E_i(t), \\ &= -\frac{1}{2}\alpha_{ij} E_i(t) E_j(t) \end{aligned} \tag{2.11}$$

Converting the above equation into a spherical tensor product allows the matrix elements in the $|JKM\rangle$ basis to be easily determined. If we define a field tensor $U_{ij} = E_i E_j$ (not related to the Maxwell field tensor), we can convert both α_{ij} and U_{ij} to second rank spherical tensors α_M^L and U_M^L, where $L = 0, 1, 2$ and $M = -2, -1, 0, 1, 2$ are tensor indices. Avoiding a discussion of the fundaments of spherical tensors we refer the reader to Zare[50] or Brink &

Satchler[53] for a detailed discussion and simply provide the relevant formulae in appendix B. The components of the polarizability tensor are generally calculated in the molecular frame and must be rotated to lab frame. Calling the molecular frame tensor $\alpha^L_{m'}$, the interaction Hamiltonian can be written as

$$V = -\frac{1}{2}(-1)^{L+M}\alpha^L_M U^L_M = -\frac{1}{4}(-1)^{L+M} D^L_{M,m'}(\mathbf{\Omega})\alpha^L_{m'} U^L_M, \tag{2.12}$$

where $\mathbf{\Omega} = \{\theta, \phi, \chi\}$ are the Euler angles and $D^l_{m,m'}$ are the Wigner rotation matrix elements. If α_{ij} is diagonal in the principal axes coordinate system only spherical components α^0_0, α^2_0 and $\alpha^2_2 = \alpha^2_{-2}$ are non zero. Further since we always work in the limit where $2\pi/\omega$ is much less than the duration of the pulse the oscillating part of the field has been averaged over a single cycle. This diagonalizes U_{ij} leaving only the spherical components U^0_0, U^2_0 and $U^2_2 = U^2_{-2}$. Finally, putting all this together we get

$$\begin{aligned} V(t) \;=\; & -2\pi\alpha I_0(t)\Bigg[\frac{2-3\epsilon_X^2}{\sqrt{6}}\left[\alpha^2_0 D^2_{0,0} + \alpha^2_2(D^2_{0,2} + D^2_{0,-2})\right] \\ & + \frac{\epsilon^2}{2}\left[\alpha^2_0(D^2_{2,0} + D^2_{-2,0}) + \alpha^2_2(D^2_{2,2} + D^2_{2,-2} + D^2_{-2,2} + D^2_{-2,-2})\right]\Bigg]. \end{aligned} \tag{2.13}$$

Here the constraint $\epsilon^2_X + \epsilon^2_Z = 1$ is used to eliminate ϵ_Z. If the light is linearly polarized along the Z axis $\epsilon_X = 0$ and the second term drops out. Wrting out the $D^L_{M,m'}$ explicity in terms of the Euler angles[50,53] and setting $\epsilon^2_X = 0$ gives a simplified expression for interaction with linealry piolarizaed light,

$$V(t) = -\frac{2\pi\alpha I_0(t)}{\sqrt{6}}\left[\alpha^2_0(\frac{3}{2}\cos^2\theta - 1) + \alpha^2_2\sqrt{\frac{3}{2}}\sin^2\theta\cos 2\chi\right]. \tag{2.14}$$

A density plot of this potential for ethylene at a field strength of 0.1 a.u. is shown in Fig. 2.3.The clear minimum at $\theta = 0$ garners the expectation that the molecules will roll down the potential hill such that the a and Z axes align. As we will see in the next section

this is indeed case.

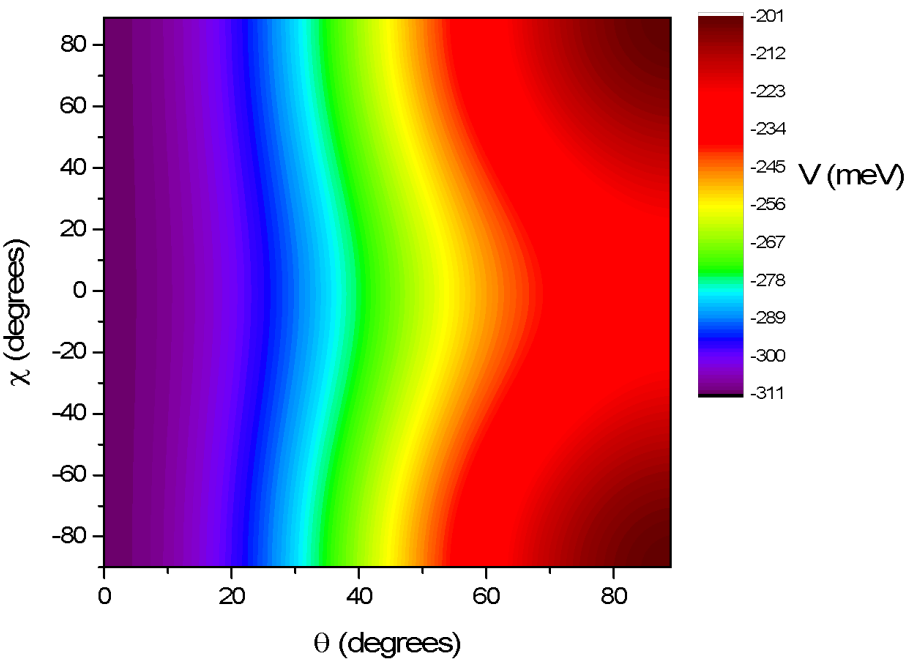

Figure 2.3: *The potential for a rigid ethylene molecule at 0.1 a.u field strength.*

We can now insert the potential into the TDSE,

$$(H_{rot} + V(t))\Psi(t) = i\frac{d\Psi(t)}{dt}, \tag{2.15}$$

and we can expand the time dependent wave function in the $|JKM\rangle$ basis with time dependent coefficients -

$$\Psi(t) = a_{JKM}(t)\,|JKM\rangle\,. \tag{2.16}$$

Substituting this in the TDSE and taking the inner product with $\langle J'K'M'|$ provides the following coupled differential equations in the $a_{JKM}(t)$

$$i\frac{da_{JKM}}{dt} = a_{JK'M}H_{K,K'} + a_{J'K'M'}\,\langle JKM|V|J'K'M'\rangle \tag{2.17}$$

where $H_{K,K'}$ are matrix elements of the field-free Hamiltonian. An analytic form for the matrix elements of the interaction Hamiltonian can be derived in terms of Clebsch-Gordon (CG) coefficients from Eq. 2.14 using the functional form of $|JKM\rangle$,

$$\langle \mathbf{\Omega}|JKM\rangle = \sqrt{\frac{2J+1}{8\pi^2}} D^{J*}_{M,K}(\mathbf{\Omega}) \tag{2.18}$$

and the expression for the integral of three Wigner functions given in appendix A. Using these Eq. 2.14 becomes

$$\begin{aligned}
&\langle JKM|V(t)|J'K'M'\rangle = -2\pi\alpha I_0(t)\sqrt{\frac{2J+1}{2J'+1}}\Bigg[\frac{(2-3\epsilon_X^2)}{\sqrt{6}}\langle J,M;2,0|J'M'\rangle \\
&[\alpha_0^2\langle J,K;2,0|J'K'\rangle + \alpha_2^2(\langle J,K;2,2|J',K'\rangle + \langle J,K;2,-2|J',K'\rangle)] \\
&+\frac{\epsilon_X^2}{2}(\langle J,M;2,2|J',M'\rangle + \langle J,M;2,-2|J',M'\rangle) \\
&[\alpha_0^2\langle J,K;2,0|J'K'\rangle + \alpha_2^2(\langle J,K;2,2|J',K'\rangle + \langle J,K;2,-2|J',K'\rangle)]\Bigg].
\end{aligned} \tag{2.19}$$

The expression for the matrix elements of V provides selection rules for transitions between rotational states. The first term (first two lines) on the right excites coherences between states with $\Delta J = 0,1,2$, $\Delta M = 0$ and $\Delta K = 0,2$. Only these coherences are excited by a linearly polarized pulse ($\epsilon_X = 0$). The excitations occur via Raman transitions and produce a broad angular momentum wave packet. This results in a narrow distribution in the conjugate angles creating a spatially confined distribution. Classically we might imagine that the pulse kicks the molecule into rotation about the θ (excitation in J), as well as χ (excitation in K). The wave function evolves in time as a function of these angles during and after the laser pulse. For an elliptically polarized pulse the additional coherences $\Delta M = 2$ are excited in combination with all the other possible coherences. The role of each of these coherences is elaborated in chapter 3.

The above expression can then be used to numerically propagate Eq. 2.17 to calculate the values of the $a_{JKM}(t)$ at the end of the pulse, $t = t_0$. The CG coefficients are calculated

using the well known analytic expression[50]. The equations 2.17 are solved using a fifth order Dormand-Price stepper from the *Numerical Recipies*[54] code package. After the pulse the a_{JKM} are converted to the asymmetric top basis, the columns of the conversion matrix being the eigenvectors of H_{rot}. The field-free coefficients are then propagated with the usual quantum mechanical phase factor

$$a_{J\tau M}(t) = a_{J\tau M}(t_0)e^{-i2\pi E_{J\tau M}(t-t_0)}, \tag{2.20}$$

where the indices are *not* summed over. The time dependent expectation value of a physical quantity can then be calculated from these coefficients.The relevant expectation values vary depending on the experiment and will be dealt with in the corresponding sections. The $a_{J\tau M}$ are converted back to the symmetric top basis before calculating the expectation values,

$$\langle Q \rangle_{J_0,\tau_0,M_0}(t) = a^*_{JKM}(t)a_{J'K'M'}(t) \langle JKM| Q |J'K'M'\rangle \tag{2.21}$$

where Q is the quantity of interest and J_0,τ_0 and M_0 are indices of the initial state – at $t = 0$, $a_{J\tau M} = \delta_{J,J_0}\delta_{\tau,\tau_0}\delta_{M,M_0}$, $\delta_{i,j}$ being the Kroneker delta function.

The number of basis functions required for numerical propagation depends on the highest rotational levels excited by the field, which depend on the intensity and duration of the laser pulse as well as the initial temperature of the gas. Generally we chose an arbitrary limiting value $J = J_{max}$. Typically if the chosen J_{max} is too small the functions $\langle Q \rangle_{J_0,\tau_0,M_0}(t)$ exhibit fast oscillations as a result of population being driven back down into lower states. Higher temperatures also require larger J_{max} as the initial thermal population consists of higher energy states.

2.2.4 Thermal and nuclear spin statistics

Finally, we must construct a thermal average of the expectation values to reflect the experimental conditions. We assume a Boltzmann distribution of initial asymmetric top states, allowing a thermally averaged quantity to be expressed as

$$\langle Q \rangle (t) = g_i \frac{e^{(\frac{-E_i}{kT})}}{Z} \langle Q \rangle_i (t) \tag{2.22}$$

where $i = \{J_0, \tau_0, M_0\}$ and g_i,E_i, Z and Q are the spin statistical weight, energy, partition function and the quantity being averaged. The value of g_i depends on the symmetry of the rotational state. As explained in the previous section (cf. fig 2.2 and related discussion) this can be determined by the parity of J and value of τ. The associated value of g_i depends on the molecule in question. In general the molecular Hamiltonian commutes with a number of operators that form its symmetry group[52]. Specifically, all permutations of identical nuclei that are physically allowed (those that do not break or twist bonds) combined with the inversion operation form the molecular symmetry group[49]. Ground state vibrational and electronic wave functions are always symmetric with respect to all group operations. The associated combination of nuclear spin and rotational wave functions then need to be symmetric with respect to all operations that permute an even number of fermions or any permutation of bosons, and antisymmetric with respect to an odd number of permutations of fermions. In cases where none of the operations in table 2.1 correspond to a permutation of identical nuclei all $g_i = 1$.

As an example we can consider the case of the ethylene molecule, C_2H_4. Fig. 2.4 shows a ball and stick model of ethylene in its electronic ground state with the atoms and axes labeled. Written alongside are the permutations of identical nuclei that correspond to the operations of D_2, where (ij) is a permutation of the nuclei i and j. Since carbon is a boson and hydrogen is a fermion, all the group operations correspond to an even number of fermion permutations requiring that the total wave function be symmetric under all operations, i.e.

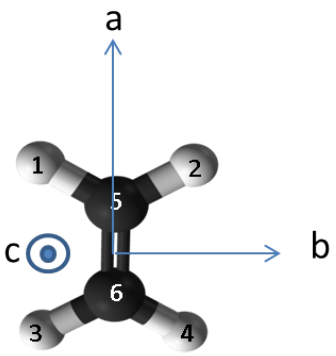

$$C_a^{\pi} = (12)(34)$$
$$C_b^{\pi} = (13)(24)(56)$$
$$C_c^{\pi} = (14)(23)(56)$$

Figure 2.4: *A ball stick model of ethylene, the white atoms are hydrogen and the black carbon. Also shown is the correspondence between the permutation and rotation group operations under which the wave function is symmetrized.*

generate the A representation. This requirement can only be fulfilled if both nuclear spin and rotational wave functions that transform the same way under the group operations, and therefore generate the same representation are combined. Essentially, we must determine the number of possible spin states in each representation. The possible total spin states of the four spin 1/2 hydrogen nuclei are not explicitly derived, but we note that there are five $S = 2$ states, two $S = 0$ states, and nine $S = 1$ states, where S is the total spin angular momentum. The seven states of even S all generate the A representation, while sets of three $S = 1$ states each generate the B_a,B_b and B_c respectively[49]. Hence $g_i = 7$ for A states, and three for all other states. A quick way of determining this using more general group theoretic considerations is given in Bunker and Jensen[49]

The g_i being determined the partition function –$Z = g_i e^{(\frac{-E_i}{kT})}$ – is summed in order of energy up to $J_0 = J_{max}$. The population factor –$P_i = g_i e^{(\frac{-E_i}{kT})}/Z$– is then summed until it reaches a value of 0.99. The state at which this occurs is considered the highest energy state in the thermal distribution. The partition function is then re-summed up to this state and $\langle Q \rangle (t)$ is calculated using Eq. 2.22.

2.2.5 Some sample calculations

Depicted in fig. 2.5 is $\langle \cos^2 \theta \rangle (t)$ for a gas of ethylene molecules at 9 K excited with a 120 fs, 4 TW/cm^2 linearly polarized laser pulse (polarizability and inertia tensors used for calculations performed with all molecules studied in this thesis are provided in appendix C). This is a widely used metric for one dimensional alignment as it tracks the proximity of the molecular symmetry axes (in this case the C=C axis) to the laser polarization direction. For an isotropically distributed sample $\langle \cos^2 \theta \rangle = 1/3$, and 1 if all molecules in the sample are aligned with the polarization axis. In fig 2.5 after the initial kick the value rises and peaks at about 0.45, bringing the a axis into weak alignment with the Z axis. It then begins to drop as the molecules continue to rotate away from the laser polarization. However as time goes by there are small and large recurrences of alignment. As marked in the figure, the initial alignment and the peak of the second recurrence are separated by approximately 18.2 ps, which corresponds to $1/(B + C)$, where B and C are rotational constants of the molecule. Additionally, a minimum in $\langle \cos^2 \theta \rangle$ occurs at $1/2(B + C)$.

Though well understood, the physical manifestation of these recurrences or revivals in the lab is rather astounding to witness. The molecules align shortly after a kick pulse as anticipated by analyzing the interaction potential. However at some later time they re-align without any coaxing, as though of their own volition. This strangeness is a distinctly quantum mechanical effect with no classical analogue. An examination of equation 2.20 provides an explanation for this ostensible anomaly. Essentially, at any time $t - t_0$ when the phase factor for every state goes to 1, we have a replica of the wave packet at $t - t_0 = 0$. Therefore if the initial wave packet exhibits alignment it should recur at these times. For linear and symmetric rotors the energy levels are even integer multiples of the rotational constant B ($E_J = J(J + 1)B$ for a linear rotor). Substituting $2nB$ for $E_{J\tau M}$ in 2.20 yields the conclusion that the initial alignment should revive when $t - t_0 = 1/2B$.

No simple expression exists for the energies of an asymmetric top, however there are known subsets of energy levels that can be approximated as even integer multiples of some

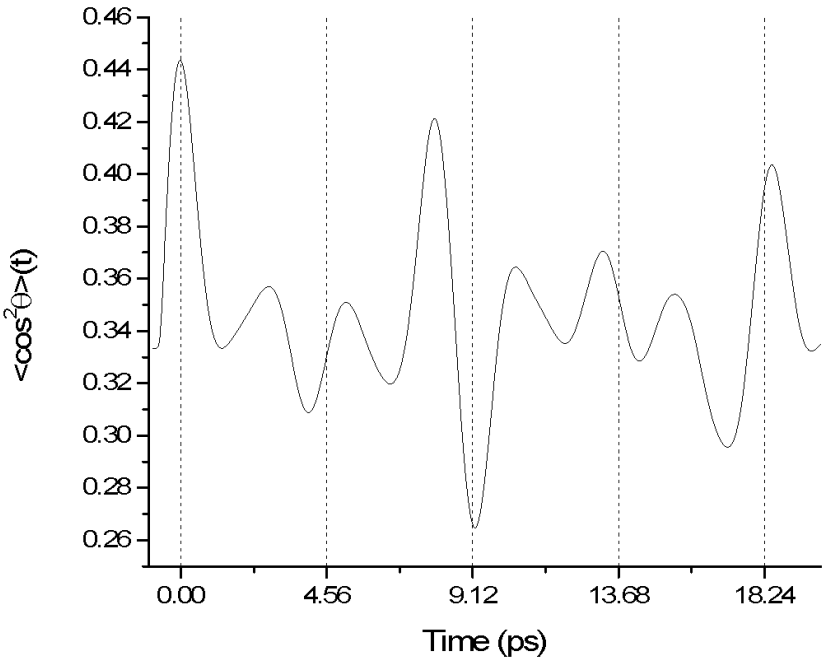

Figure 2.5: $\langle \cos^2 \theta \rangle (t)$ *with the J-type revivals (see text) marked by the dashed black lines.*

combination of rotational constants of the molecule[40].The revivals in fig. 2.5 result from energy levels that can be approximated as even integer multiples of $(B + C)/2$, with a corresponding revival period of $1/(B + C)$. The half revival at $1/2(B + C)$ occurs when the phase factor of each state is -1, resulting in the observed exactly opposite behavior. The energy levels are high lying levels in a given J manifold, separated by $\Delta J = 2$ with $\frac{\tau}{J} \approx 1$, but are prominent at lower J values and for nearly symmetric prolate molecules such as ethylene. We may picture the motion of the top during these revivals as a precession of the a axis about the laser polarization. The smaller revivals occurring between these result from subsets of initial states of the thermal distribution. Specifically, at $t - t_0 = 1/4(B + C)$ J-type states excited out of initial states belonging to a particular symmetry representation are in phase producing a revival, but these are out phase with revivals from initial states of a different symmetry representation. However since the distribution of ethylene consists

dominantly of states belonging to the totally symmetric A representation (cf. discussion about thermal statistics), the contributions do not exactly cancel leaving a small excess from the symmetric representation.

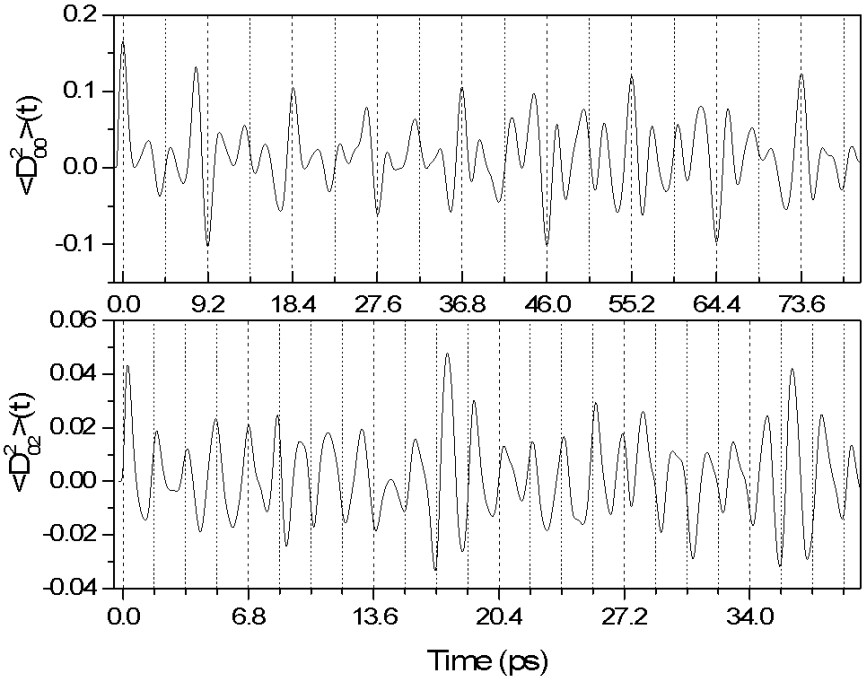

Figure 2.6: *Top panel -* $\left\langle D^2_{0,0}\right\rangle(t)$ *with the J-type revivals marked by the dashed black lines, Bottom panel -* $\left\langle D^2_{0,2}\right\rangle(t)$ *with the A-type revivals marked by the dashed black lines*

The features of the rotational dynamics discussed thus far are not unique to asymmetric rotors. In fact, from fig 2.5 it would be difficult to discern that the molecule is an asymmetric top. Fig. 2.6 shows expectation values of the Wigner functions $\left\langle D^2_{0,0}(t)\right\rangle$ and $\left\langle D^2_{0,2}(t)\right\rangle$ over longer time windows. Since the Wigner functions form a complete basis set on the three dimensional rotation group they can be used to represent any angular function, for instance $\cos^2\theta = \frac{1}{3} + \frac{2}{3}D^2_{0,0}$. $\left\langle D^2_{0,0}\right\rangle(t)$ therefore has exactly the same behavior as $\left\langle\cos^2\theta\right\rangle(t)$ as is evident by comparing both plots over the 20 ps time window. At later times the revival amplitudes diminish and after 40 ps any sign of periodic behavior vanishes. This is a

manifestation of the incommensurate energy level spacing unique to asymmetric tops. The lower panel of fig. 2.6 shows $\left\langle D^2_{0,2} \right\rangle (t)$ over a 40 ps window. Here we see much faster oscillations dominating the J-type recurrences. These revivals have a period of about 1.7 ps corresponding to $1/4A$ for the first 7.5 ps, after which they persist but begin to shift. They correspond to rotations about the molecular a axis, in this case about the C=C bond. They occur due to the mixing of states separated by ΔJ and $\Delta K = 2$ by the laser pulse and are named A-type revivals. A single linearly polarized laser pulse cannot induce these revivals in symmetric tops. Additionally revivals corresponding to rotations about the molecular c axis can also occur but are not seen here as the states that correspond to the requisite near commensurate energy spacing exist only for large J are not excited by this laser pulse[40]. There are no known revivals corresponding to rotations about the classically unstable b axis. In general, a measurement made from a rotationally excited gas can exhibit several kinds of recurrences. Here, $\left\langle D^2_{0,0} \right\rangle (t)$ does not exhibit A-type revivals since $D^2_{0,0}(\mathbf{\Omega})$ is independent of χ, the angle of rotation about the C=C axis. $\left\langle D^2_{0,2} \right\rangle (t)$ however is sensitive to both A and J-type revivals $D^2_{0,2}(\mathbf{\Omega})$ being a function of both θ and χ. This idea will be revisited in the context of experimental measurements in chapters 4 and 5 on degenerate four wave mixing and alignment dependent measurements from asymmetric tops. Further, in the following chapter on 3D alignment revivals involving all three Euler angles will emerge when trains of pulses with different polarizations are used to excite a rotational wave packet.

2.2.6 Cosmological Aside - The Mixmaster Universe

Though the problem of the quantum mechanical rigid rotor was essentially solved by the fifties, interest in the problem was rekindled in the early seventies due to cosmologist Charles Misner's suggested solution to the horizon problem[55]. In the standard model of cosmology there is no mechanism by which points in the sky far enough away from each other could ever have been in contact. However the uniformity and isotropy of the cosmic background radiation suggests that they were in contact long enough to thermalize before the universe

became transparent and the radiation was released. Misner attempted to solve the problem by inducing chaotic dynamics in his model of the early universe hoping to 'mix' up the contents. It was hence termed the Mixmaster universe. Shortly after Hu[56] noticed that the equations of scalar waves in a static or frozen Mixmaster universe are identical to those of an asymmetric quantum rotor. A further generalization was by made by Dowker and Petengill[57] who were able to solve the equations for spinor waves in a frozen Mixmaster universe, which turned out to be equivalent to an asymmetric quantum top with spin!

They essentially noticed that the inclusion of spin lowers the D_2 symmetry to D_2' — the eight-group or quaternion group. This will likely be of relevance in molecular physics when considering the orientation of asymmetric tops with non-negligible spin-orbit coupling. More so, it is an intriguing example of subtle connections in nature that fuel this authors interest in physics.

2.3 Experimental Apparatus

We now outline the features of the experimental apparatus used in all or many of the experiments that are presented in this thesis.These include a pulsed laser producing intense, femtosecond duration pulses, a pulsed gas source that produces cold gas targets and a velocity map imaging spectrometer used to measure the momentum of charged particles from the cold target and produced by the laser pulses.

2.3.1 Supersonic Even-Lavie Valve

Generally rotationally cooled molecular samples allow for stronger coherent laser excitation of rotational states, and thus stronger alignment[58]. A cooled sample is acquired by expanding a seeded molecular gas into a vacuum chamber through a pulsed Even-Lavie valve[59]. A 0.5 mm diameter skimmer selects the central portion of the expanding gas allowing it to pass into the VMI chamber. The valve provides a rotationally cooled thermal distribution of

molecules by supersonic expansion through a 100 μm diameter trumpet nozzle. The cooling is driven by the pressure gradient across the nozzle, and may to some extent be understood by ideal gas thermodynamics. For a very detailed and thorough analysis we direct the reader to *Atomic and Molecular Beam Methods*[60], which is the source of the following material.

Qualitatively, as the nozzle shrinks down to 100 μm the gas contracts and speeds up. The velocity at the mouth of the nozzle depends on the pressure ratio of the source to the background pressure in the chamber – $G = P_o/P_b$. If G is less than a gas dependent critical value the flow into the chamber will be subsonic (Mach number, $M < 1$) and the pressure at the exit will match the ambient chamber pressure. However if the ratio exceeds the critical value the flow at the mouth reaches $M = 1$. In this scenario the pressure at the mouth is P_o/G, and thus significantly higher than the ambient pressure in the chamber. The gas then expands supersonically and cools, with the curious property that it accelerates as it expands reaching $M >> 1$ a few nozzle diameters away. Since the flow is supersonic it travels a certain distance into the chamber before 'registering' the ambient pressure it must equilibrate to, at which point a disk like shock occurs known as the Mach Disk. The region preceding the Mach Disk is the 'zone of silence', named for its ignorance of the surrounding pressure. Placing a skimmer in the zone of silence provides the cooled molecular beam. The distance to the Mach Disk from the nozzle exit and hence the length of the zone of silence is given by,

$$\frac{x_m}{d} = 0.67\sqrt{G}. \tag{2.23}$$

At normal operating conditions in our chamber $P_o \approx 52 \times 10^3$ torr and $P_b \approx 10^{-5}$ torr. For $d = 100\ \mu m$, $x_m = 4.8\ m$, which is significantly longer than the length of the chamber! This illustrates one of the advantages of a pulsed jet. The average ambient pressure in the chamber is kept low –provided the vacuum pump can evacuate enough gas between pulses allowing for a large pressure gradient– and the significant number density of each pulse results in high signal-to-noise. However we must note that the above expression assumes

the gas is not pulsed, though the G scaling becomes more favorable for a pulsed jet. It is also assumed that the nozzle is purely convergent, ignoring the divergent shape at the exit of the trumpet nozzle.

Another significant approximation made here is that the flow is continuous rather than molecular. Assuming that the gas is ideal we can then approximate the expansive cooling using the first law of thermodynamics and the ideal gas equation,

$$\frac{T}{T_0} = \frac{1}{1 + \frac{\gamma-1}{2}M^2} \tag{2.24}$$

where T_0 is the source temperature and $\gamma = 1 + 2/f$, f being the number of degrees of freedom of the molecule comprising the gas. Calculating the Mach number as a function of distance from the nozzle requires numerical integration of hydrodynamic flow equations. However it can be approximated by a polynomial expansion the coefficients of which can be read from tables for a gas of given γ[60]. This suffices for a crude temperature estimate and it turns out for atomic gases $T/T_0 \approx .01$ far away from the nozzle. For molecular gases the cooling of internal temperature is driven by collisions and is more challenging to estimate. To further complicate things as the gas expands and the number density drops the gas approaches the 'quitting surface' where collisions cease leaving the internal degrees of freedom 'frozen' in a non-equilibrium state. The cooling therefore depends on the rate of collision and the number of collisions that occur before freezing. Rotational cooling thus turns out be more significant in heavier species as the rotational states are closely spaced requiring fewer collisions to relax.

The cone shaped nozzle of the Even-Lavie valve provides enhanced cooling and beam intensity[61]. The valve body contains a spring loaded plunger pushing against a polyamide sealing gasket placed between the nozzle aperture and the plunger surface. The assembly sits in a metal tube filled with the high pressure gas with ceramic holders on either end. The tube is surrounded by a solenoid coil which carries a high current pulse ($\approx$500 A) of μs duration ($\approx$ 7.2 μs for our experiments). While the magnetic field generated by the current pulse

is present the plunger is pulled back letting gas flow into the chamber. The temperature of skimmed beams of some seeded samples from this jet has been measure to be below 1 K[59]. About 1 mm from the nozzle we are able to experimentally determine the rotational temperature of pure N_2 and helium seeded C_6H_5I to be 20 K and 8 K respectively[62]. After the skimmer in the VMI chamber these drop to about 3 K and 1 K[63]. Measurements presented later in this thesis estimate a temperature of 9 K for skimmed and helium-buffered ethylene molecules.

2.3.2 Single Shot VMI Spectrometer

We use the technique of Velocity Map Imaging (VMI), originally conceived by Eppink and Parker, to measure the alignment distribution of molecules[64]. Generally a VMI spectrometer consists of a imaging detector and an electrostatic lens housed in an ultra-high vacuum (UHV) chamber. The lens sends all particles with equal velocity components in the plane of the detector to the same point on it. This 'velocity focusing' action is achieved by a three plate lens consisting of repeller, extractor and ground plates. The ground plate is connected to the wall of the chamber, and the repeller and extractor plates are connected via high voltage feed throughs to a power supply outside the chamber. The voltage ratio between the repeller and extractor for optimum velocity focusing was determined by Eppink and Parker to be 0.71, though this may vary depending on the specific design of the spectrometer.

A schematic of our lens is shown in fig. 2.7. Gas from the Even-Lavie Valve is skimmed through a 0.5 mm skimmer into a separate chamber containing the lens. The 1 mm hole in the ground plate lets gas through into the spectrometer. An intense laser beam is crossed with the gas sample which generates charged fragments that are accelerated by the focusing field towards a 40 mm chevron stack microchannel plate (MCP) detector with a phosphor screen behind it. The MCP converts a single particle or photon hit into a pulse of electrons which are accelerated to the phosphor screen causing it to fluoresce with a lifetime of 120 ns. Since fragments of different mass-to-charge ratio will differ in time of flight (TOF) a time

gated voltage can be applied to the inner MCP plate in order to measure the velocity map of a selected fragment ion. Typically the MCP is operated with -800 V on the front plate, 1200 V on the back plate and 4200 V on the phosphor with the duration of a few hundred ns time gate on the front plate voltage.

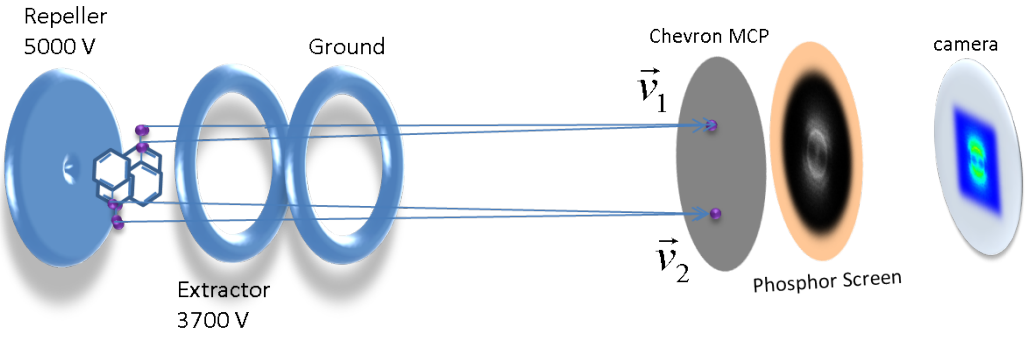

Figure 2.7: *A schematic of our VMI spectrometer. The spacing and inner diameters of the plates and the applied volateges were determined by SIMION simulations performed by Vinod Kumarappan. The voltages were fine tuned during the experiment to optimize velocity focusing.*

The light from the phosphor is detected by a 1280 × 1024 complementary metal oxide (CMOS) chip camera (Basler A504k). Using only a portion of the CMOS chip allows the camera to acquire images at a faster rate. Since our pulsed gas source operates at 1 kHz we set the camera with an imaging lens at the appropriate distance (≈ 30 cm) from the phosphor such that only a 500 × 500 area of the chip is illuminated allowing the camera to acquire a single image for every gas pulse. 1 kHz transfer of these images onto a computer is facilitated by a National Instruments frame grabber (PCIe 1429) connected to the camera via camera link cables (640 MB/s). Only the positions of particle hits on the detector are determined on-the-fly and saved. A Laplacian of Gaussian (LoG) filter is applied to the raw image which smooths it and sharpens edges in order to to make hit counting more effective. An intensity threshold is then applied to the image before hit positions, ellipticities and areas are determined by an algorithm available with the Lab View Vision package. Any hit

with area and ellipticity above a certain threshold is considered a double. These thresholds, as well as the specific LoG filter and the intensity threshold are decided by collecting a large number ($\approx$ 5000) of raw images at very low count rates ($\approx$ 10 hits/image) such that the probability of a double hit is negligible. The entire analysis is run on each of these images and the parameters varied until doubles constitute less than 0.5 % of the total counts.

The on-the-fly hit analysis is made possible by a dual quad core Dell T7400 workstation using a producer-consumer model[65,63] . Each core acts as a consumer and picks up an image acquired by the camera (the producer) out of the buffer memory, analyzes it and saves the hit positions to memory while the camera continually writes images to the buffer. Each processor is sufficiently fast (3 GHz clock rate) to ensure that whole process can take place at 1 kHz. Typical images are shown in chapter 3.

The spectrometer is also used in time-of-flight mode. In this mode 1700 V is applied across the MCP (1700 V on the back plate with the front grounded) and the current from the back plate is picked off through a resistive coupling box. A narrow peak in the voltage across the resistor is observed when a charged fragment hits the detector. The arrival time on the detector t is related to the mass-to-charge (m/q) ratio of the frament in the following way[64],

$$t = k\sqrt{\frac{m}{q}} + t_0, \tag{2.25}$$

where k and t_0 are unknown constants. Given this equation the TOF axis can be calibrated if the m/q for two fragments are known. The spectrometer is used in this manner for experiments described in in chapter 5.

2.3.3 The Kansas Light Source

The gas pulse in the VMI spectrometer is intersected by laser pulses generated by the Kansas Light Source (KLS). KLS produces pulses with a central wavelength of 790 nm and bandwidth (FWHM) $\approx$ 32 nm, translating to a transform limited Gaussian pulse duration

of about 30 fs. The pulses are generated at a repetition rate of 2 kHz with an energy of 2 mJ/pulse. A commercially purchased mode locked titanium doped sapphire (Ti-saph) oscillator[66,67] produces 300 mW pulses at 83 MHz with a central wavelength of 790 nm and bandwidth $\approx$ 85 nm, translating to a transform limited pulse duration of about 11 fs. Two of these pulses are picked every millisecond using a Pockel cell and are amplified to 2 mJ using chirped pulse amplification[68,67]. The amplification occurs in a single stage consisting of fourteen non-colinear passes through a liquid nitrogen cooled Ti-saph crystal pumped by two counter propagating 532 nm picosecond pulsed lasers, each with a $\approx$20 W output. In this mode the laser is gain saturated resulting in a $\leq$0.5% power fluctuation over a minute. This output sustains over a period of about 8 hrs after which the dewar holding the liquid nitrogen cooling the crystal must be refilled. All the experiments presented in this thesis were performed with the KLS laser operating in this mode.

2.4 Summary

This chapter covered the fundamental quantum mechanics of an asymmetric rigid rotor and its interaction with the electric field of a pulsed laser. The mathematical details of this interaction and their physical consequences were analyzed through numerical simulations for the asymmetric top ethylene. We would urge the reader to keep in mind the following general characteristics of the dynamics of asymmetric top molecules — they are *not* of a periodic nature, but may be approximately so for near symmetric tops and a linearly polarized laser pulse excites $\Delta K = 2$ transitions resulting in coherent rotation about χ, which is not excited in symmetric molecules. The former is a result of the irregular spacing of energy levels (cf. fig. 2.2) and is expressed as a de-phasing of the excited rotational wave packet, and the latter is a result of the rotational asymmetry in the molecular frame and is expressed as additional revivals occurring on the time scale of rotation about the molecular axis. In the following chapter we examine the effect of exciting motion about the third Euler

angle ϕ with the goal of determining a feasible route to three dimensional alignment.

We also described the fundaments of important experimental apparatus used in experiments described the following chapters. In the next chapter we use the described laser to induce 3D alignment in gas molecules from the Even-Lavie valve. The degree of alignment is estimated by measuring the momenta of charged fragment produced by the laser.

Chapter 3

Field-Free Three-Dimensional Alignment

We begin this chapter with a brief survey of metrics used to quantify three dimensional alignment, highlighting the various reasons why these are inadequate. We then develop a new metric which lacks these inadequacies and increases monotonically as the distribution approaches perfect 3D alignment. Additionally, the analytic form of the matrix elements of the metric help elucidate the dynamics that need to be initiated to induce 3D alignment. Numerical calculations with the near-prolate asymmetric top iodobenzene demonstrate the effectiveness of the metric and also clarify the field-free rotational dynamics that can occur after a 3D aligning pulse sequence. The understanding of the metric facilitates the development of a scheme used to produce strong field-free 3D alignment (FF3DA), thus breaking a long standing impasse in the field of molecular alignment. The scheme is developed theoretically and demonstrated experimentally employing the theoretical concepts and experimental instrumentation described in the previous chapter.

3.1 A new metric for 3D alignment

As described in the previous chapter 1D alignment is easily quantified using the metric $\langle\cos^2\theta\rangle$, θ being the polar angle of the molecular symmetry axis with respect to laser polarization. This provides a single number that increases from 1/3 for an isotropic distribution to 1 for a perfectly aligned ensemble. Further, numbers below 1/3 characterize planar alignment perpendicular to the laser polarization, with a value of 0 indicating perfect anti-alignment. Combinations of various expectation values have been used in the literature to quantify 3D alignment, though no analogous single metric has been developed. As an intuitive extension of $\langle\cos^2\theta\rangle$ to 3D alignment we may stipulate that $\langle\cos^2\theta\rangle$,$\langle\cos^2\phi\rangle$ and $\langle\cos^2\chi\rangle$ being simultaneously equal to 1 indicates perfect 3D alignment and intermediate values away from the isotropic values indicate weaker alignment. These are often used as measures in the literature[69,35,70]. The pitfalls of this strategy are illustrated in Fig. 3.1. The molecules in panel a) are strongly 3D aligned at $\theta = 20°$, $\phi = 0°$, 180° and $\chi = 0°$, requiring a single rotation of $\theta = 20°$ for each molecule to achieve perfect 3D alignment. Rotating one molecule to ϕ and $\chi = 90°$ as in panel b) significantly reduces the values of $\langle\cos^2\phi\rangle$ and $\langle\cos^2\chi\rangle$, obliging us to claim by our measure that the 3D alignment is significantly degraded. However both molecules are still a single 20° rotation away from the target distribution, and therefore the degree of alignment is unchanged. Any similar measure constructed with independent expectation values of the cosines of the Euler angles will be similarly restrictive, excluding distributions that are in fact 3D aligned.

Expectation values of the direction cosines $\langle\cos^2\theta_{ij}\rangle$ where $i = a,b,c$ and $j = X,Y,Z$ are also used in numerous studies on 3D alignment[8,71,72]. θ_{ij} are angles between lab and molecular frame axes, therefore these expectation values measure the proximity of individual lab and molecular frame axes. In order to determine the degree of 3D alignment it is necessary to calculate multiple $\langle\cos^2\theta_{ij}\rangle$ and due to the complexity of field-free asymmetric top dynamics the degree of alignment is often unclear. A metric for 3D alignment analogous to $\langle\cos^2\theta\rangle$ for 1D alignment can help untangle these complex field-free dynamics, as well as

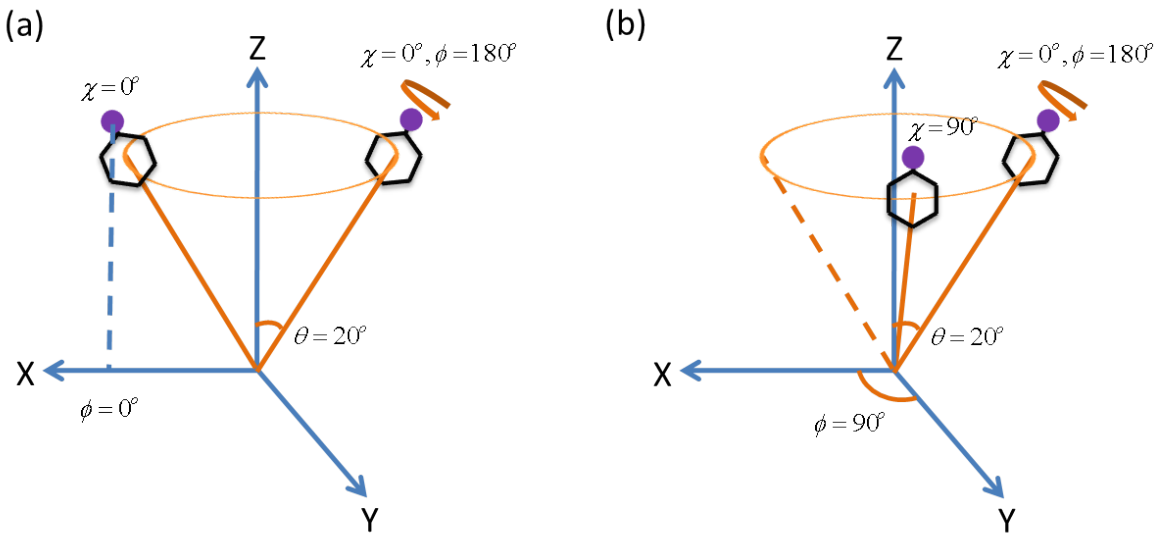

Figure 3.1: *A depiction of the pitfalls of using squared cosines of the Euler angles as a measure of 3D alignment. See text for the associated discussion.*

provide a reliable quantifier for the degree of 3D alignment in theoretical and experimental studies. In the following section we develop such a metric in the axis angle representation of rotations.

3.1.1 Theoretical development of the metric

This section is an extended and edited version of the discussion published in *Physical Review A* [73].

The problem of specifying a metric for 1D alignment of linear molecules is particularly simple. The space of possible orientations is the surface of a unit sphere. Since we are interested in the displacement of the members of the molecular ensemble from a lab-fixed axis, it is very convenient to chose this axis as the Z-axis, and then measure the geodesic distance to each ensemble member on the unit sphere. This geodesic distance is quite intuitive — the cosine of the polar angle θ gives the length of the great circle arc that takes the z-axis to the Z-axis. The expectation value of $\cos\theta$ is widely accepted as a metric for

characterizing 1D orientation of molecules. With this choice, a value of 1 denotes perfect orientation, and -1 denotes perfect anti-orientation. For 1D aligned distributions every molecule at θ has an equivalent companion at $\pi - \theta$ and we use $\langle \cos^2 \theta \rangle$ instead of the identically-zero $\langle \cos \theta \rangle$. In this case, perfectly aligned, perfectly anti-aligned and isotropic distributions have $\langle \cos^2 \theta \rangle = 1$, 0, and 1/3, respectively.

Our goal is to specify a similar scheme for 3D alignment. We show here that the use of the axis-angle representation of rotations in 3D is better suited for this purpose than either the Euler angle or the direction cosine representation. In this representation, arbitrary rotations are in terms of an angle and the unit vector along the axis of rotation. The cosine of the angle δ_{if} is the geodesic distance between the initial orientation $(\theta_i, \phi_i, \chi_i)$ and the final orientation $(\theta_f, \phi_f, \chi_f)$, and is a metric on SO(3)[74], the group of rotations of rigid bodies in space. In terms of the rotation matrices $\mathbf{R}(\theta, \phi, \chi)$,

$$\cos \delta_{if} = \frac{1}{2} \left[tr \left(\mathbf{R}^T(\theta_i, \phi_i, \chi_i) \mathbf{R}(\theta_f, \phi_f, \chi_f) \right) - 1 \right] \tag{3.1}$$

This metric does not depend on the choice of the coordinate system in which the Euler angles are defined — the trace is invariant when the coordinate system is rotated. The angle δ_{if} is in radians, and varies from 0 to π. This angle is, thus, a natural choice for characterizing the degree of three dimensional orientation and alignment of rigid molecules. The initial orientation is the molecular frame (MF), and the final orientation is the lab frame (LF — $\mathbf{R}(\theta_f, \phi_f, \chi_f)$ is the identity matrix in this case).

Two properties of the angle δ make it attractive as a measure of orientation of molecules in space. First, although different vectors in the MF will be rotated by different angles, no vector is rotated by an angle greater than δ. Therefore, δ is both the angle of a single rotation to the target, and the *worst* possible separation of all MF axes from the corresponding LF axes. The expectation value $\langle \cos \delta \rangle$ is, therefore, a good metric for 3D orientation. However the metric in this form is not suitable as a measure of 3D alignment, as will be discussed later.

In terms of the Euler angles, the direction cosines and the Wigner matrix elements, we have

$$\cos\delta = (\cos\theta + 1)\left[\cos(\phi + \chi) + 1\right]/2 - 1 \tag{3.2a}$$

$$= \left[\cos\theta_{xX} + \cos\theta_{yY} + \cos\theta_{zZ} - 1\right]/2 \tag{3.2b}$$

$$= \left[D^1_{11}(\mathbf{\Omega}) + D^1_{00}(\mathbf{\Omega}) + D^1_{-1-1}(\mathbf{\Omega}) - 1\right]/2 \tag{3.2c}$$

The last form, derived using expressions for the rotation matrices from Zare[50], is particularly useful for computation in the symmetric top basis, used in the previous chapter for solving the TDSE for rigid rotor dynamics.

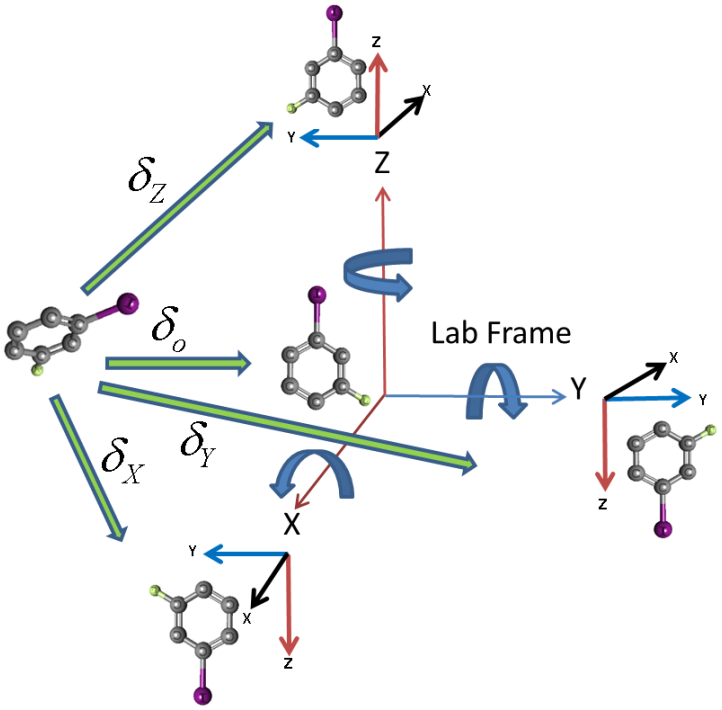

Figure 3.2: *Target orientations for 3D alignment depicted with ball and stick models of 3-Fluoroiodobenzene.*

3D alignment requires that every molecule oriented with the lab frame has an equivalent

companion a π rotation away about any lab frame axis. This provides four target orientations for 3D alignment, the lab frame and the coordinate axes generated by a π rotation about the X, Y and Z axes as shown in Fig. 3.2. An arbitrarily oriented molecule can be brought into any one of these orientations by a single rotation. The angles of rotation into the target orientation are labeled in Fig 3.2 as δ_0 for rotation into the lab frame and δ_X,δ_Y and δ_Z for rotation into the frames rotated about the X,Y and Z axes respectively. The rotation matrices $R(\mathbf{\Theta})$ for the target orientations are diagonal, with elements $(1,1,1)$, $(1,-1,-1)$, $(-1,1,-1)$ and $(-1,-1,1)$ along the diagonal, and expressions for $\cos\delta_j$ are readily obtained using Eqns. 3.1 and 3.2b.

$$\cos\delta_0 = (1+\cos\theta)\left[1+\cos(\phi+\chi)\right]/2 - 1 \tag{3.3a}$$

$$\cos\delta_X = (1-\cos\theta)\left[1-\cos(\phi-\chi)\right]/2 - 1 \tag{3.3b}$$

$$\cos\delta_Y = (1-\cos\theta)\left[1+\cos(\phi-\chi)\right]/2 - 1 \tag{3.3c}$$

$$\cos\delta_Z = (1+\cos\theta)\left[1-\cos(\phi+\chi)\right]/2 - 1 \tag{3.3d}$$

These equations can be recast as

$$\cos(\frac{\delta_0}{2}) = \cos(\frac{\theta}{2})\cos(\frac{\phi+\chi}{2}) \tag{3.4a}$$

$$\cos(\frac{\delta_x}{2}) = \sin(\frac{\theta}{2})\sin(\frac{\phi-\chi}{2}) \tag{3.4b}$$

$$\cos(\frac{\delta_y}{2}) = \sin(\frac{\theta}{2})\cos(\frac{\phi-\chi}{2}) \tag{3.4c}$$

$$\cos(\frac{\delta_z}{2}) = \cos(\frac{\theta}{2})\sin(\frac{\phi+\chi}{2}) \tag{3.4d}$$

These are the well-known Euler parameters e_0, e_1, e_2 and e_3[75]. The Euler parameters are not independent of each other, and satisfy the relation

$$e_0^2 + e_1^2 + e_2^2 + e_3^2 = 1. \tag{3.5}$$

In terms of the $\cos\delta_j$, this relation becomes

$$\cos\delta_0 + \cos\delta_x + \cos\delta_y + \cos\delta_z = -2. \tag{3.6}$$

It is clear that the expectation value of each $\cos\delta_j$ for an isotropic distribution is $-1/2$. Thus, on average, the angle required to rotate a molecule to any one of the target orientations is 120°. In fact, for any distribution with D_2 symmetry, $\langle\cos\delta_i\rangle$ must all be $-1/2$. Therefore, one of these functions alone is not suitable as a measure of 3D alignment. Further, the $\cos^2\delta_j$ do not have the same expectation value for each of the equivalent target orientations rendering them unsuitable as a metric for 3D alignment for distributions lacking D_2 symmetry, such as a distribution of three dimensionally oriented chiral molecules[76].

The constraint in Eqn. 15 can be viewed geometrically as a plane in the 4D space spanned by the $\cos\delta_i$'s. A point in this plane, ($\cos\delta_0$,$\cos\delta_X$,$\cos\delta_Y$,$\cos\delta_Z$), represents a possible molecular orientation. By plugging in numbers for the cosines of the Euler angles in Eqns. 6-9 we see that the points (1,-1,-1,-1), (-1,1,-1,-1), (-1,-1,1,-1), (-1,-1,-1,1) represent the four target orientations and form vertices of the 4D plane. The radius of a 4D sphere centered at the origin proves to be a good metric,

$$\cos^2\delta \equiv \frac{1}{4}\left[\sum_i \cos\delta_i^2\right] \tag{3.7}$$

A scale factor of 1/4 is introduced to ensure that $0 \leq \cos^2\delta \leq 1$. This metric has the required symmetry— it treats the target orientations as equivalent — and the important property that an increase in the value of the metric is accompanied by a reduction in the distance to the nearest target orientation from *all possible* starting points. This property can be visualized for the special case of 1D alignment. In this case there are only two target orientations separated by a π rotation. θ being the angle of rotation into the molecular frame, the hyperplane Eq. 3.6 reduces to the line $\frac{1}{2}(\cos(\theta)+\cos(\pi-\theta))=0$ in $(\cos(\theta),\cos(\pi-\theta))$ space. The 3-sphere defining the metric reduces to a circle of radius R, $\frac{1}{2}(\cos^2(\theta)+\cos^2(\pi-$

$\theta)) = R^2$, which trivially reduces to $\cos^2\theta = R^2$, the widely used metric for 1D alignment. Fig. 3.3 shows the line and a circle of radius $1/\sqrt{2}$, with the target orientations marked. The line represents all allowed values of θ and its intersection with the circle the specific orientations associated with $\cos^2\theta = 1/4$ ($R^2 = 0.5$). From any starting point on the line, movement towards the nearest target results in a in increase of $\cos^2\theta$.This property applies to the 3-sphere defined by $\cos^2\delta = R^2$ and the 3D hyperplane defined by Eqn. 3.6.

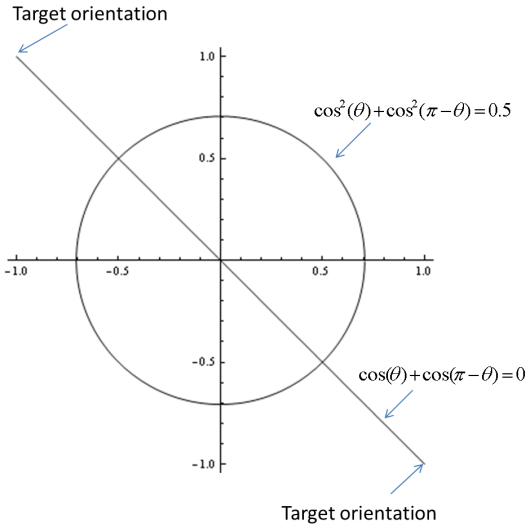

Figure 3.3: *A geometric representation of the 1D reduction of the metric.*

In terms of the direction cosines, it is easily seen that

$$\cos^2\delta = \frac{1}{4}\left(1 + \cos^2\theta_{xX} + \cos^2\theta_{yY} + \cos^2\theta_{zZ}\right). \tag{3.8}$$

In this form, several properties of $\langle\cos^2\delta\rangle$ are apparent. For perfect alignment $\cos^2\delta = 1$. The expectation value of the function for a uniform distribution of molecules is 1/2, while the minimum possible value is 1/4. The minimum is obtained for the worst 3D-aligned molecules — at $\theta = \pi/2$, $\cos(\phi+\chi) = 0$ and $\cos(\phi-\chi) = 0$ — there are eight perfectly anti-aligned orientations, and a 120° rotation about the unit vector $(\pm\sqrt{1/3},\pm\sqrt{1/3},\pm\sqrt{1/3})$ is required to bring them into alignment with any of the four target orientations. If the z axis is

perfectly aligned with the Z-axis, the x and y axes are necessarily confined to the XY plane. If these axes are uniformly distributed in the XY plane, $\langle \cos^2 \theta_{xX} \rangle = \langle \cos^2 \theta_{yY} \rangle = 1/2$. In this case $\langle \cos^2 \delta \rangle = 3/4$. Thus, the difference between 1D and 3D alignment is just a matter of degree — aligning only in one dimension brings the distribution closer to the target distribution in 3D and should be considered a limited form of 3D alignment.

The matrix elements of $\cos^2 \delta$ in the symmetric top basis illuminate the rotational dynamics needed to induce 3D alignment. The procedure to find these is detailed in appendix A and the result is simply quoted here -

$$\begin{aligned}
&\left\langle JKM \right| \cos^2 \delta \left| J'K'M' \right\rangle = \frac{1}{4} \\
&+ \left[\frac{1}{4} \delta_{JJ'} \delta_{KK'} \delta_{MM'} + \frac{1}{4} \sqrt{\frac{2J+1}{2J'+1}} \left\langle J, M; 2, 0 | J', M' \right\rangle \left\langle J, K; 2, 0 | J', K' \right\rangle \right] \\
&+ \left[\frac{1}{8} \sqrt{\frac{2J+1}{2J'+1}} \Big\{ \left[\left\langle J, K; 2, 2 | J', K' \right\rangle + \left\langle J, K; 2, -2 | J', K' \right\rangle \right] \right. \\
&\left. \times \left[\left\langle J, M; 2, 2 | J', M' \right\rangle + \left\langle J, M; 2, -2 | J', M' \right\rangle \right] \Big\} \right]
\end{aligned} \tag{3.9}$$

Each matrix element splits into three terms. The constant 1/4 is the minimum value of $\cos^2 \delta$, reflecting the fact that no molecule is more than 120° away from perfect 3D alignment. The second term reflects the alignment of the z-axis with the Z-axis, and is directly related to the matrix element for $\cos^2 \theta_{zZ}$. The coherences that contribute to this term involve $\Delta J = \pm 2$ and $\Delta K, M = 0$. The last term contains the contributions for coherences that involve $\Delta K \pm 2$ *and* $\Delta M = \pm 2$. Since K and M are projection of J on z and Z respectively this coherence corresponds to the coordinated motion of the molecules about the z and Z axes. There is no contribution from coherences in which $\Delta K = \pm 2$ *or* $\Delta M = \pm 2$. These coherences contribute to $\cos^2 \theta_{xX}$ and $\cos^2 \theta_{yY}$ (cf. appendix A) but cancel out in $\cos^2 \delta$. This elucidates an essential feature of 3D alignment: only *coupled motion* about the z and Z

axes can contribute to 3D alignment.The absence of the third term, and the corresponding uncoupled motion can be traced back to the D_2 symmetry of 3D alignment. The value of one of the $\cos\delta_j$ (and hence 3D orientation) can be improved by uncoupled rotation about either the z or the Z axes, but the requirement that a 3D alignment requires D_2 symmetry introduces the three additional target orientations. Bringing molecules to each of these orientations simultaneously necessitates coupled motion about the z and Z axes. This feature is evident in Eqn. (3.3), where the Euler angles χ and ϕ —variables conjugate to K and M respectively — appear only in pairs.

3.1.2 Numerical Example

We may now use Eq. 3.9 with the methods described in the previous chapter to calculate $\langle\cos^2\delta\rangle$ for a rotationally excited molecular ensemble. The results of TDSE calculations for iodobenzene (rotational constants and polarizabilities provided in appendix C), a near-prolate top, subject to a single linearly polarized pulse and two time separated orthogonally-polarized pulses are shown in Fig. 3.4 for the direction cosines and in Fig. 3.5 for the metric. Each pulse has a Gaussian temporal envelope with a duration(full width at half maximum of the intensity) of 170 fs and a peak intensity of 8 TW/cm^2. From Figs. 3.4 and 3.5 it is clear that for a linearly polarized pulse $\langle\cos^2\delta\rangle$ reflects the behavior of $\langle\cos^2\theta_{zZ}\rangle$, indicating that 1D alignment brings the molecules closer to one of the target orientations for 3D alignment. The changes in $\langle\cos^2\theta_{xX}\rangle$ and $\langle\cos^2\theta_{yY}\rangle$ induced by a linearly polarized pulsed contribute negligibly, if at all, in driving the molecules to 3D alignment.

For two crossed polarized pulses however, we see that the behavior of $\langle\cos^2\delta\rangle$ does not reflect that of any individual direction cosine. Clearly, after the second pulse $\langle\cos^2\theta_{xX}\rangle$ and $\langle\cos^2\theta_{yY}\rangle$ rise sharply indicating that the molecular x and y axes are being driven to the lab X and Y axes. $\langle\cos^2\theta_{zZ}\rangle$ however begins to drop away after the second pulse indicating the molecular z axis is being driven away from the lab Z axis. In this case, since the z axis of iodobenzene rotates much slower than the other two axes, it has not strayed very far from

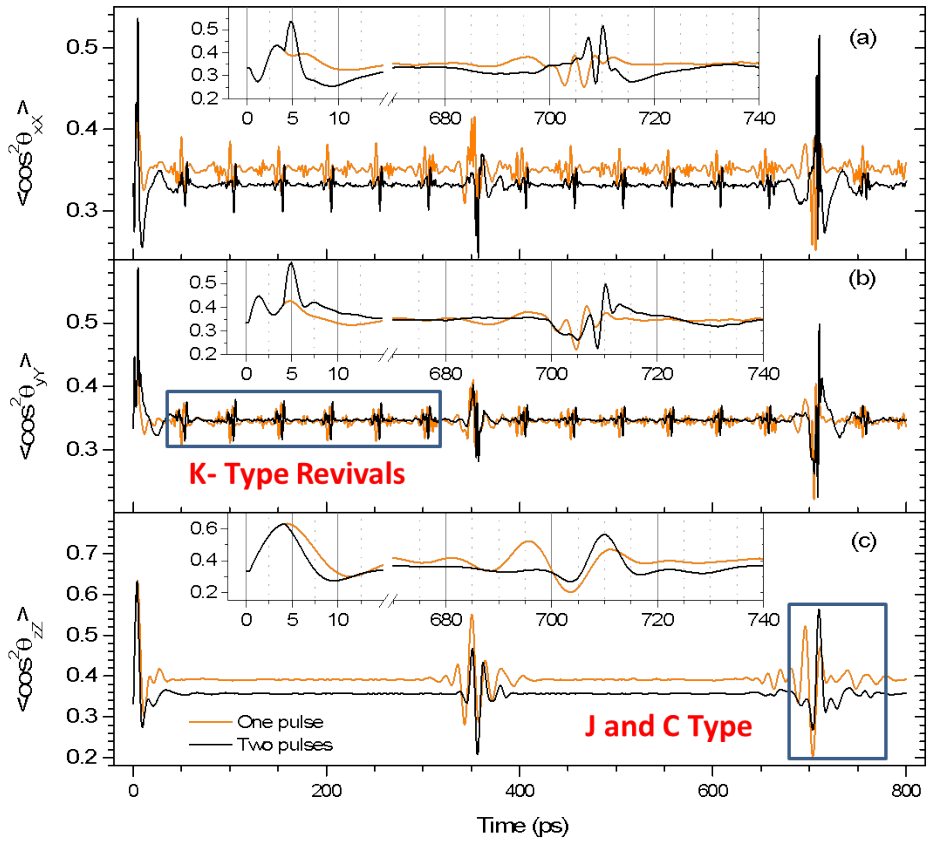

Figure 3.4: *The expectation values of the direction cosines after one linearly polarized pulse and two cross polarized pulses for a thermal gas of iodobenzene molecules at 0.5 K. Adapted from Makhija* et al.[73].

the Z axis when the other axes are at their peak alignment (at about 4.8 ps), thus producing a 3D aligned population. This information can be easily gleaned from $\langle \cos^2 \delta \rangle$ alone. We see that after the second pulse $\langle \cos^2 \delta \rangle$ rises sharply and peaks at 4.73 ps, indicating that the second pulse drives the molecules further toward 3D alignment, and the best 3D alignment occurs at 4.73 ps.

In the two pulse case $\langle \cos^2 \delta \rangle$ has a unique revival structure as well. In the one pulse case both $\langle \cos^2 \theta_{xX} \rangle$ and $\langle \cos^2 \theta_{yY} \rangle$ show K type revivals (occurring at 50.3 ps) in opposite directions. These do not appear in the $\langle \cos^2 \delta \rangle$ trace indicating that these revivals do not

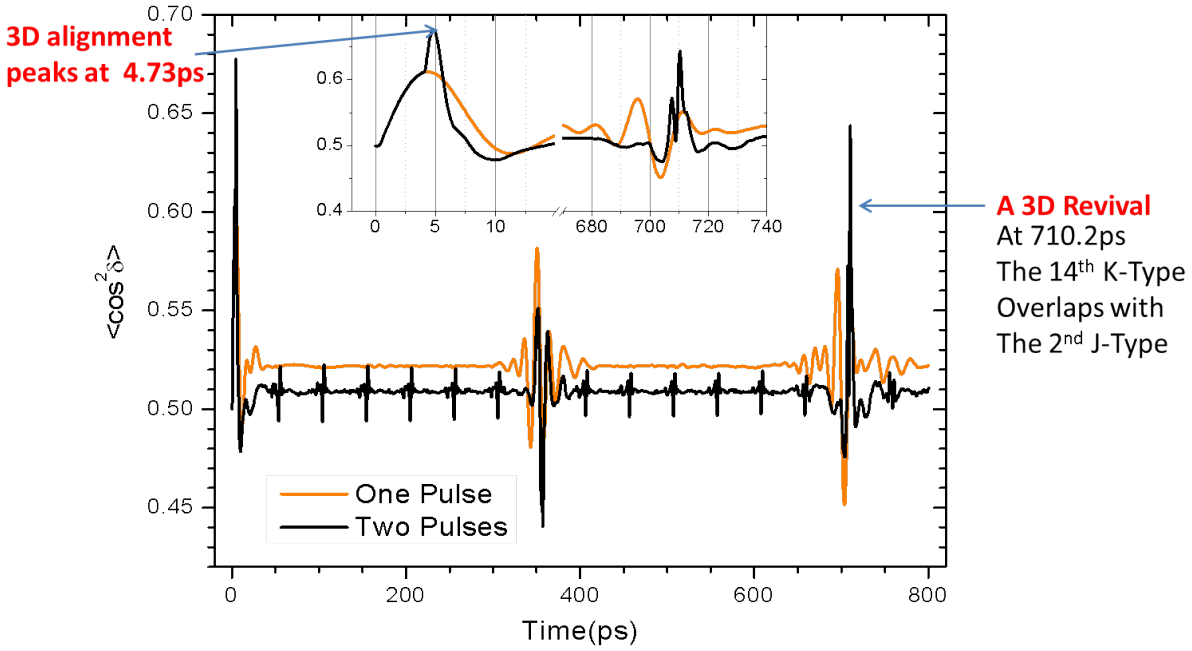

Figure 3.5: *The expectation values of the our metric after one linearly polarized pulse and two cross polarized pulses for a thermal gas of iodobenzne molecules at 0.5 K. Adapted from Makhija* et al.[73].

result from the coupled motion of the x and y axes. $\langle \cos^2 \delta \rangle$ does shows J and C type revivals (occurring at 377.3 and 353.8 ps respectively) mimicking those in $\langle \cos^2 \theta_{zZ} \rangle$, signifying the alignment of the z axis. In the two pulse case the K type revivals in $\langle \cos^2 \theta_{xX} \rangle$ and $\langle \cos^2 \theta_{yY} \rangle$ are the in same direction and appear in $\langle \cos^2 \delta \rangle$ as well, indicating coupled motion about the z and Z axes. In addition, the fourteenth K type revival overlaps with the second J type revival producing a sharp spike in $\langle \cos^2 \delta \rangle$ at 710.2 ps representing a revival of the initial 3D alignment. In general, 3D alignment revivals have to rely on such coincidences, where two different types of revivals together involve all three molecular axes and occur in close proximity to each other. Due to the finite temporal extent of the revivals, it is only necessary for the revival periods to be approximately commensurate for these overlaps to occur.In the manner of revivals in the 1D alignment of asymmetric tops, these 3D revivals

will neither be complete nor truly periodic but might nevertheless be substantial.

Measuring $\langle \cos^2 \delta \rangle$ is a challenge as it requires knowing the full orientation of the molecules. However, the insight provided by the development of this metric proves useful in developing an effective technique to induce field-free 3D alignment. The development of such a technique has been a long standing problem in the field, as will be outlined in the following section.

3.2 A Multi-pulse Method for field-free 3D Alignment

In this section we describe a new technique to achieve strong FF3DA. A report of the experiment described here appears in *Physical Review Letters*[42].

3.2.1 Theoretical development

In the previous section we showed that two time separated orthogonally polarized impulsive laser pulses can be used to generate field-free three dimensional alignment (FF3DA). This technique was first shown to be effective using numerical simulations by Underwood, Sussman and Stolow[8]; and was subsequently experimentally demonstrated using sulfur dioxide by Lee et.al[9]. Though effective, this method has a significant drawback. As evident in Fig. 3.4, the alignment of the z axis begins to degrade. This precludes further enhancement of the x and y alignment axes by subsequent pulses as they will further degrade the z axis alignment. It has also been shown by Rouzee et. al that a single elliptically polarized can be used to induce a weak degree of FF3DA[72]. Further, Pabst and Santra showed by numerical simulation that a sequence of time separated identical elliptically polarized only induce planar alignment of sulfur dioxide rather than FF3DA[77]. Here we show that the impasse represented by Fig. 3.4 can be overcome by using a sequence of laser pulses of different polarizations, which need to be carefully chosen based on the symmetry of the molecule. We also show, in contrast with the conclusion of Pabst and Santra, that a sequence of identical

elliptically polarized pulses does induce FF3DA provided they are impinged on molecules with the appropriate symmetry.

In order to understand how to avoid degradation of the z axis alignment in a multipulse scheme we compare the matrix elements of $\cos^2\delta$ in Eq. 3.9 to those of the interaction potential of the laser pulse with the molecular polarizability derived in the previous chapter and restated here -

$$\begin{aligned}
&\langle JKM|V(t)|J'K'M'\rangle = -2\pi\alpha I_0(t)\sqrt{\frac{2J+1}{2J'+1}}\Bigg[\frac{(2-3\epsilon_X^2)}{\sqrt{6}}\langle J,M;2,0|J'M'\rangle \\
&[\alpha_0^2\langle J,K;2,0|J'K'\rangle + \alpha_2^2(\langle J,K;2,2|J',K'\rangle + \langle J,K;2,-2|J',K'\rangle)] \\
&+\frac{\epsilon_X^2}{2}(\langle J,M;2,2|J',M'\rangle + \langle J,M;2,-2|J',M'\rangle) \\
&[\alpha_0^2\langle J,K;2,0|J'K'\rangle + \alpha_2^2(\langle J,K;2,2|J',K'\rangle + \langle J,K;2,-2|J',K'\rangle)]\Bigg].
\end{aligned} \tag{3.10}$$

The first pulse in the sequence used above is polarized along the Z axis, therefore $\epsilon_X = 0$ completely nullifying the second term (last two lines) on the right of Eq. 3.10. The remaining first term contains coherences that involve $\Delta J = \pm 2$ and $\Delta K, M = 0$ also present in the first term of the matrix element of $\cos^2\delta$ and responsible for the alignment of the molecular z axis. This term induces the 1D alignment evident in the orange curves in fig 3.4, with the additional $\Delta K = \pm 2$ coherences responsible for the K-type revivals and x and y axis alignment seen in $\langle\cos^2\theta_{xX}\rangle$ and $\langle\cos^2\theta_{yY}\rangle$. The following pulse in the sequence is polarized along the X axis, therefore $\epsilon_X = 1$. This makes the term responsible for z axis alignment negative, thus undoing the effect of the first term while simultaneously aligning the x and y axes through the $\Delta K, M = \pm 2$ coherences in the second term.This analysis of the two pulse technique begs the question - can we find a second pulse that can simultaneously align the x and y axes without effecting the z axis alignment induced by the first pulse? We could then use multiple such pulses to sequentially improve the coordinated alignment of the x and y axes without effecting the z axis alignment at all.

A brief examination of Eq. 3.10 reveals that if $\epsilon_X^2 = \frac{2}{3}$ the first term vanishes resulting in

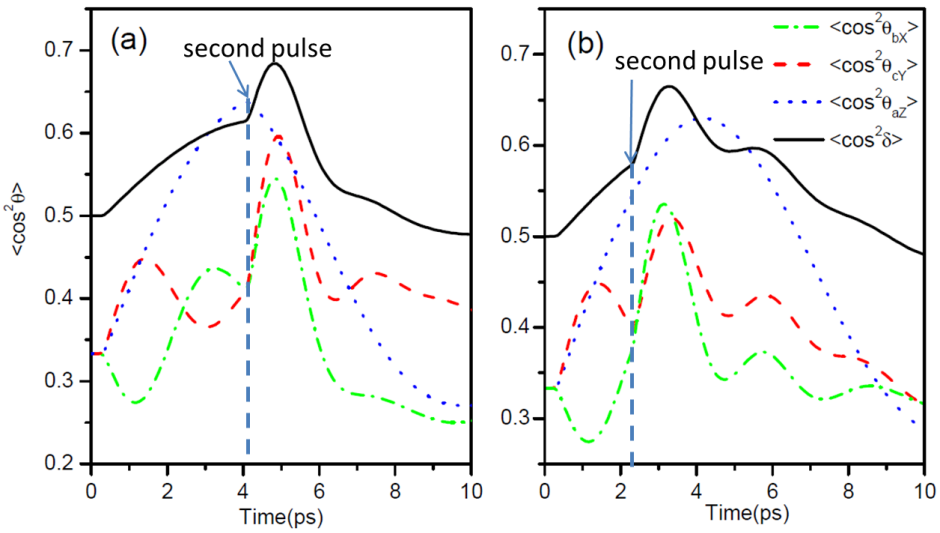

Figure 3.6: *(a) Expectation values calculated using TDSE for iodobenzene molecules subjected to two cross polarized pulses, with the peak of the second pulse arriving 3.8 ps after peak of the first. Each pulse has a Gaussian temporal envelope with durations (full width at half maximum of the intensity) of 170 fs and 75fs and peak intensities of 8 TW/cm^2 and 20 TW/cm^2. (b) The second pulse is changed to an elliptically polarized pulse with $e_x^2 = \frac{2}{3}$, and is separated by 2.5 ps from the first.*

an interaction that has *no* effect on the z axis alignment while retaining the term responsible for the x and y axes alignment. Panel (b) of Fig. 3.6 shows the effect of such a pulse pair. Panel (a) is the same cross polarized pulse pair of Fig. 3.4. The elliptical pulse in (b) comes 1.3 ps earlier than the second pulse in panel (a) to emphasize the lack of perturbation to the z axis alignment. After the second cross polarized pulse $\langle \cos^2 \theta_{zZ} \rangle$ begins to fall rapidly, however after the second elliptically polarized pulse of the same intensity and pulse duration $\langle \cos^2 \theta_{zZ} \rangle$ continues to increase while the x and y axes align as well. This allows for the possibilty of subsequent elliptically polarized pulses arriving just before the peak value of $\langle \cos^2 \delta \rangle$ to improve the x and y axes alignment without perturbing the z axis. This procedure also allows for the peak alignment of all three axes to be synchronized, greatly boosting the degree of FF3DA.This alone substantially increases the value of $\langle \cos^2 \delta \rangle$, but we need not stop here. Instead of leaving the z axis undisturbed, we can reduce the value of

e_x^2 further such that the z axis alignment *improves* with each subsequent pulse. We reduce e_x^2 for all the elliptical pulses sequentially and recalculate $\langle \cos^2 \delta \rangle$ to find the pulse sequence that yields the best alignment. In doing so we are essentially searching for a value of e_x^2 that accentuates terms in $V(t)$ which correspond to coherences that occur in $\cos^2 \delta$, while diminishing those that do not.

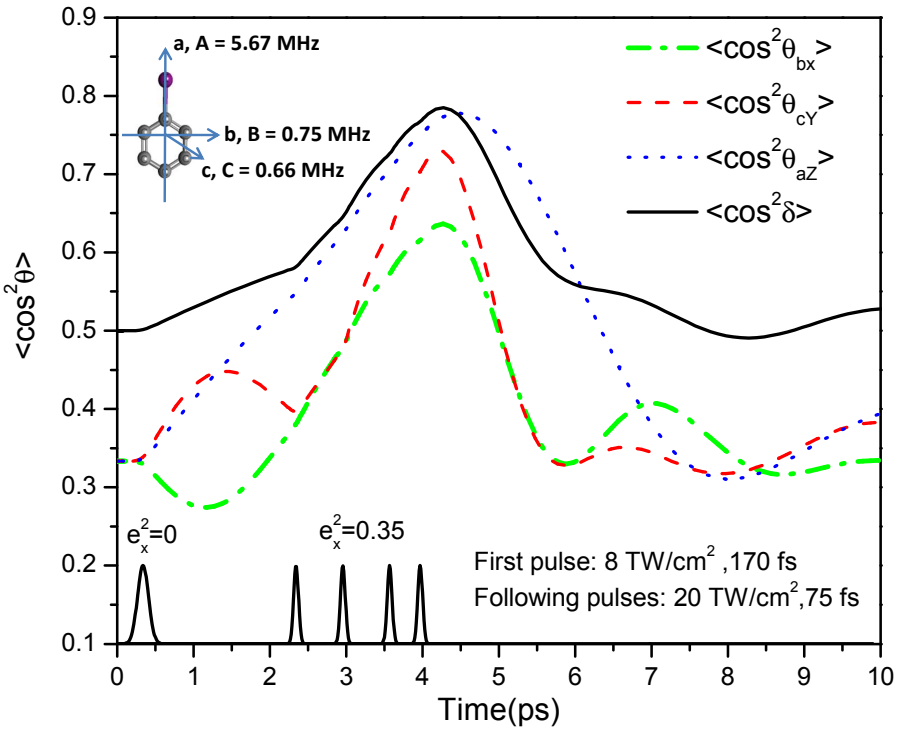

Figure 3.7: *Expectation values calculated using TDSE for iodobenzene molecules subjected to five pulses. The figure on the top left shows an Iodobenzene molecule with its a, b and c axes..*

Doing this for iodoebenzene we end up with a sequence of 4 elliptical pulses with $e_x^2 = 0.35$ following a linearly polarized pulse. The results for this pulse sequence are plotted in Fig. 3.7. Each pulse is timed to arrive just before the peak 3D alignment induced by the previous pulses. Since the alignment peaks faster after each pulse we are obliged to stop kicking when the time window after the pulse gets too short. As is evident from the figure the alignment of all axes improves after each pulse.

In the following sections we demonstrate the efficacy of this technique experimentally.

3.2.2 Experimental Demonstration

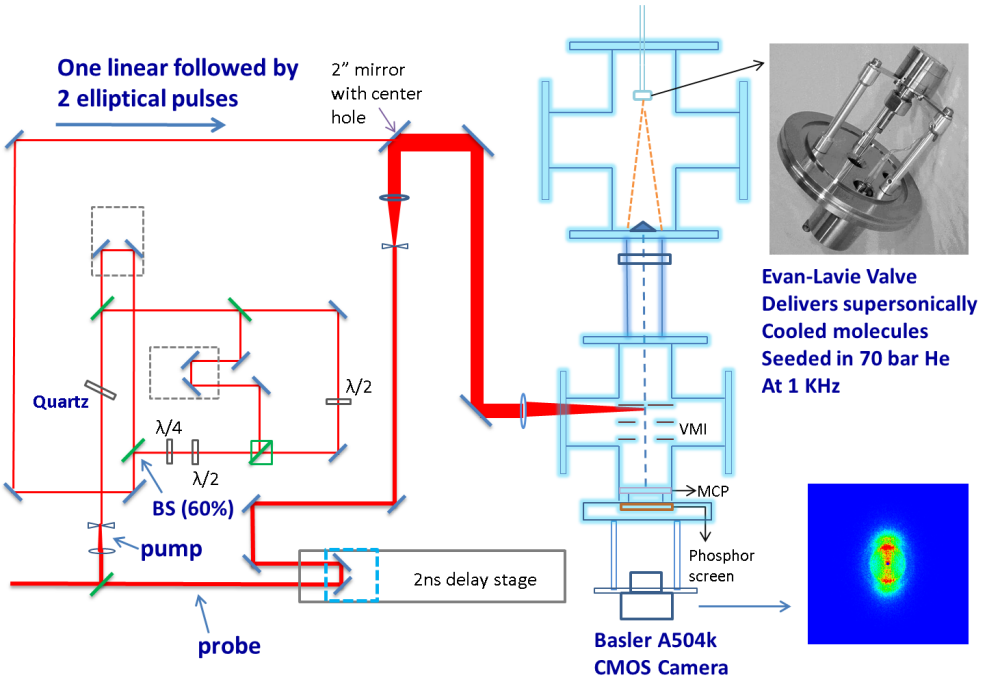

Figure 3.8: *A drawing of our experimetal setup for FF3DA of DFIB.*

A drawing of the experimental setup is shown in Fig. 3.8. The beam is first split into a 'pump' arm used for alignment and a 'probe' arm used for fragmentation by a 80/20 beam splitter (BS) with 80 % of the energy sent to the pump and 20 % to the probe. The probe beam is aligned through a 2 ns electronically controlled delay stage before it is expanded to twice its original diameter of 1 cm and recombined with the pump beam on a 2 inch mirror with a hole in the center. The diameter of the pump beam is shrunk from 1 cm to 0.6 cm using a telescopic lens pair after which a sequence of beam splitters and delay stages split it into three time delayed pulses. Two of the three pulses are recombined on a cube polarizer with orthogonal polarizations, and sent through half and quarter waveplates subsequently

resulting in circularly polarized pulses of opposite handedness. These are recombined with the original, s-polarized pump beam on a BS that reflects 60 % s-polarized and 40 % p-polarized light.This results in a sequence of pulses, the first linearly polarized defining the Z direction and the next two elliptically polarized with $\epsilon_X^2 = 0.35$ and 0.33 respectively. The polarizations were chosen to be near the optimum calculated for Iodobenzene in the previous section. The major axes of the elliptical pulses turn out be tilted with respect to the Z axis due phases picked up by the s and p components from the 60% BS. This is compensated by a tilted quartz plate added to the beam. Additionally the linearly polarized beam is also sent through a cube polarizer before recombination in order to clean up the polarization and stretch the pulse. The pulse durations as measured by cross-correlation with the 30 fs probe pulse are 325 fs for the first pulse and 275 fs for the next two pulses. The pulses are focused into the VMI spectrometer with a 35 cm focal length lens. The intensities estimated by spot size measurements on a CCD camera are approximately 7 TW/cm^2 for the first and third pulses, and 10 TW/cm^2 for the second pulse.

3.2.3 Results and Discussion

In the experiment we use 3,5 difluoroiodobenzene (DFIB), in which hydrogens in the 3,5 positions have been substituted by fluorines. Measuring the momentum distributions of the fluorines upon Coulomb explosion facilitates estimation of the alignment of the molecular plane. Substituting fluorines has a negligible effect on the polarizability tensor of the molecule leaving the interaction Hamiltonian unchanged from iodobenzene in the above calculation provided the same polarizations are used. However the rotational frequencies are significantly slower, though this only effects the optimal timing of the pulses which is determined during the experiment.

Fig 3.9 shows VMI images of singly charged iodine and fluorine fragments resulting from the break up of 3,5 difluoroiodobenzene by the probe pulse. In both figures the probe pulse is polarized perpendicular to the plane of the page. The images have been four-fold

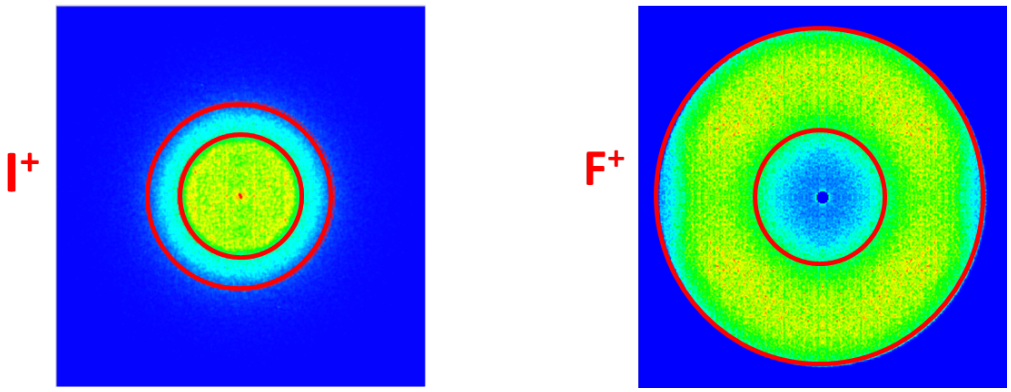

Figure 3.9: *VMI images of I^+ and F^+ for an isotropically distributed gas of DFIB molecules. The red circles mark the fragmentation channels used to estimate the degree of alignment.*

symmetrized in order to compensate for non uniformity in the detector gain. Assuming the fragments fly off along the bond axes the increasing intensity towards the center in the I^+ image and the donut shape in the F^+ image indicate an enhanced fragmentation probability for molecules aligned along the laser polarization. In images which include the pump pulses, I^+ images will always be shown with the polarization of the first pump pulse (the Z axis), and therefore the major axes of the elliptical pulses aligned vertically in the plane of the page. For the F^+ images the vertical direction will indicate the direction of the minor axis of the elliptical pulses (the X axis) and the Z axis will point into the page.

Fig 3.10 shows images after the first pump at a delay where the alignment is maximal. Shown alongside are the polarizations of the pump and probe and a cartoon of the alignment distribution relative to the detector for each image. The I^+ velocity distribution becomes directed along the Z axis. Under the axial recoil approximation this represents the distribution of the C-I molecular axes, thus indicating some degree of molecular alignment. As an experimental estimation of the degree of C-I axis alignment we calculate $\langle \cos^2 \theta_{2D} \rangle$ in the marked outer ring of the image, where θ_{2D} is the angle between the Z axis and 2D velocity vector of an ion hit. The outer ring represents I^+ breaking from a triply charged molecule with a doubly charged partner. The F^+ velocity distribution remains isotropic

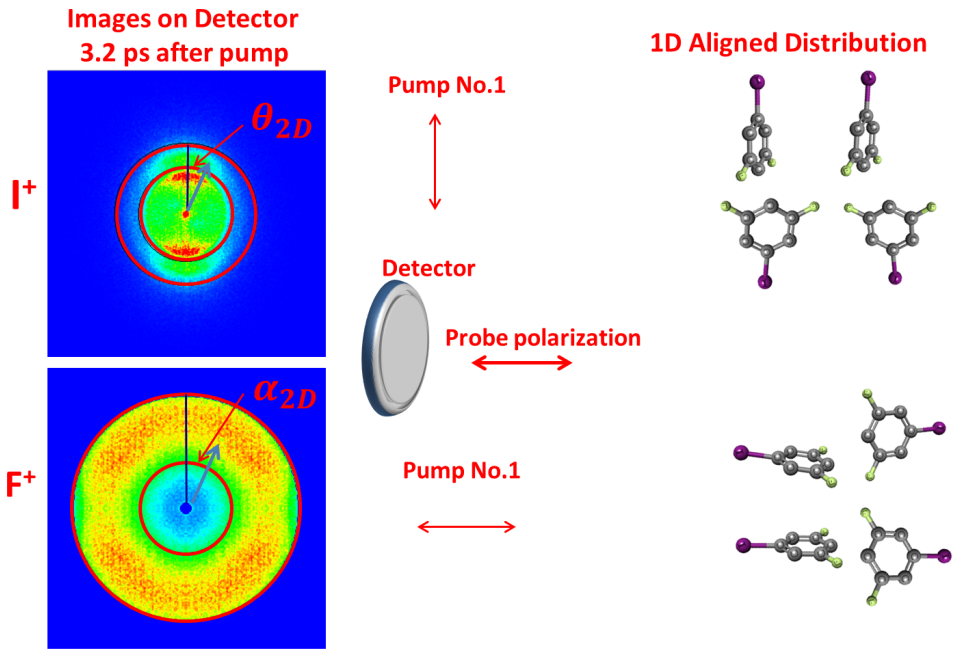

Figure 3.10: *VMI images of I^+ and F^+ for a 1D aligned gas of DFIB molecules. Shown alongside are the polarizations of the pump and probe and the alignment of the molecules relative to the detector for each image.*

within the marked ring, however the number of counts in the ring compared to those in the central hole increases also indicating 1D alignment of the C-I axis with the molecular plane spinning freely about the axis. Alignment of the plane is similarly estimated by $\langle \cos^2 \alpha_{2D} \rangle$. Fig 3.11 shows a sequence of VMI images at the alignment maxima after each pump. The timing of each pump after the first is determined by attempting to maximizing the paek values of $\langle \cos^2 \theta_{2D} \rangle$ and $\langle \cos^2 \alpha_{2D} \rangle$ that follow. Clearly, the alignment of both the C-I axis and the molecular plane is improved after each pulse. $\langle \cos^2 \theta_{2D} \rangle$ and $\langle \cos^2 \alpha_{2D} \rangle$ are plotted in Fig. 3.12 for 1, 2 and 3 pulses. Note that the peak values of both coincide after third pulse at 4.6 ps, where the maximum FF3DA is observed.

Though figs. 3.11 and 3.12 indicate a high degree of FF3DA, some ambiguity still exists concerning the alignment of the C-I axis. Since the polarization plane is perpendicular to the

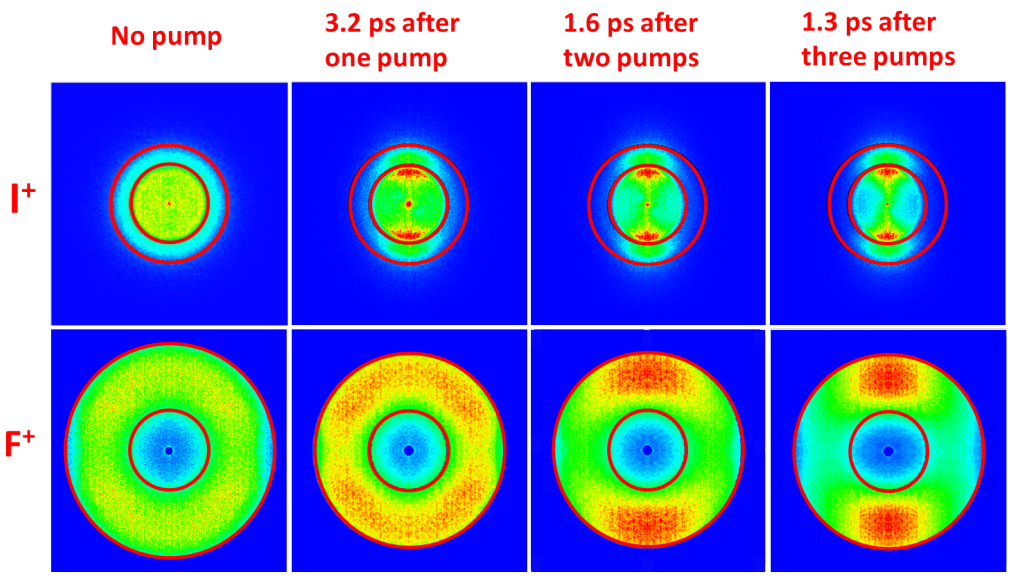

Figure 3.11: *VMI images of I^+ and F^+ from DFIB showing the peak alignment achieved after one, two and three pulses.*

plane of the detector, the distinction between 1D alignment and alignment of the C-I axis in the polarization plane is precarious. To clarify this distinction we measured numerous projections of the velocity distribution at the peak 1D alignment after the first pump and at the peak FF3DA. Using these projections we tomographically reconstructed the 3D velocity distribution using a filtered back projection algorithm available with the MATLAB image toolbox[63,78]. This is conceptually similar to a x-ray CT scan, but rather than rotating the detector, the polarizations of all the pulses are rotated with a step size of 2° and 90 I^+ VMI images are measured to reconstruct the normalized 3D distributions shown in Fig. 3.13. The probe pulse used to measure these distributions was circularly polarized to ensure the fragmentation is not selective in the polarization plane. The reconstructions also allow the determination of $\langle \cos^2 \theta \rangle$, θ being the angle between the 3D velocity vector of the fragment and the Z axis. Provided the axial recoil approximation holds this is a direct reflection of the degree of alignment of the C-I axis. $\langle \cos^2 \theta \rangle = 0.65$, along with the evident alignment of the molecular plane shown in Fig. 3.11 unambiguously demonstrate FF3DA of the molecules

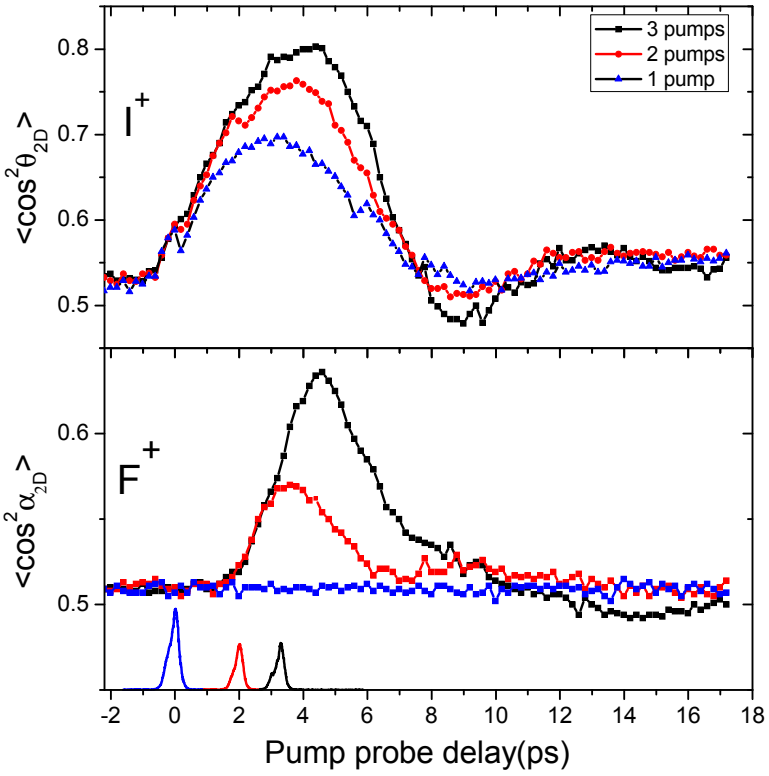

Figure 3.12: $\langle\cos^2\theta_{2D}\rangle$ *and* $\langle\cos^2\alpha_{2D}\rangle$ *for one, two and three pumps pulses.*

at 4.6 ps.

Additionally we present calculations using the rigid rotor TDSE to supplement the experimental demonstration. Fig 3.14 shows calculations for the direction cosines $\langle\cos^2\theta_{iJ}\rangle$ and $\langle\cos^2\delta\rangle$ where i and J represent the molecules principal axes and the lab fixed axes respectively, and $\langle\cos^2\delta\rangle$ is our metric for 3D alignment. Calculations for the three pulses used in the experiment result in a peak $\langle\cos^2\delta\rangle$ value of 0.71, which to the molecule, on average, being not more than a single 32.6° rotation away from one of the target orientations for 3D alignment. However, the calculated and measured values of $\langle\cos^2\theta_{aZ}\rangle$ of 0.65 and 0.70 do not agree indicating that the measured distribution may not be as well 3D aligned.

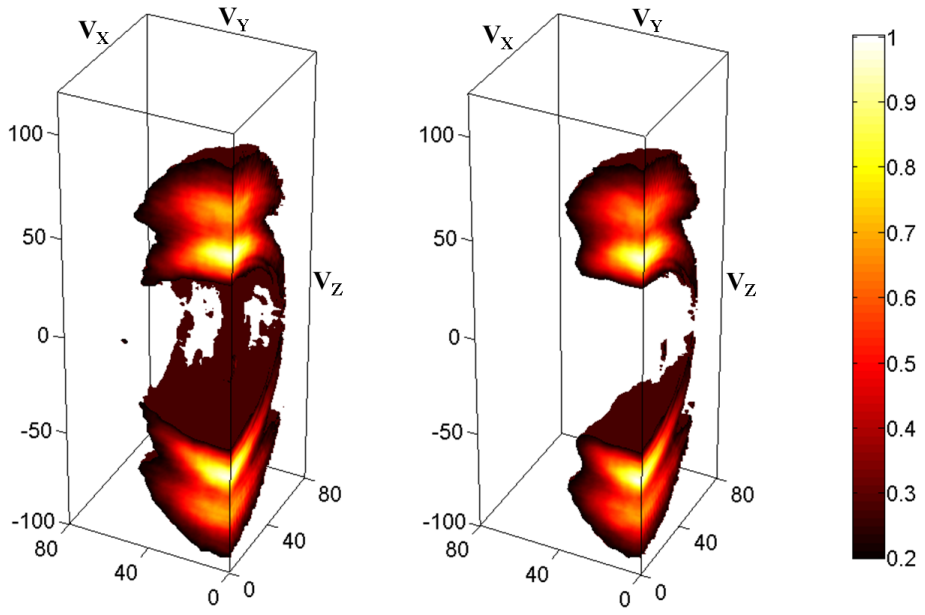

Figure 3.13: *Retrieved 3D velocity distributions of I^+ at the peak alignment after one pulse (left) and three pulses (right). A reduction in the number of counts perpendicular to the alignment axis indicated an increase in the degree of alignment along the Z axis. Reproduced from Ren* et al.[42]

This disagreement likely results from the fact the calculations neglect the spatial intensity distribution of the pump pulses at the interaction region, and that the polarizability values used are those of iodobenzene. Additionally, a rotational temperature of 1 K is assumed without independent corroboration and the selectivity of the probe pulse is not taken into account. We also show the potential for further improvement of the FF3DA demonstrated experimentally by adding a fourth pulse in the calculation. We would also like to emphasize that important parameters such as the pulse timings and ellipticities in both calculations and experiment are 'hand tuned'. This being the case we would be surprised if experimental or theoretical efforts employing optimization algorithms to tune these parameters could not do better.

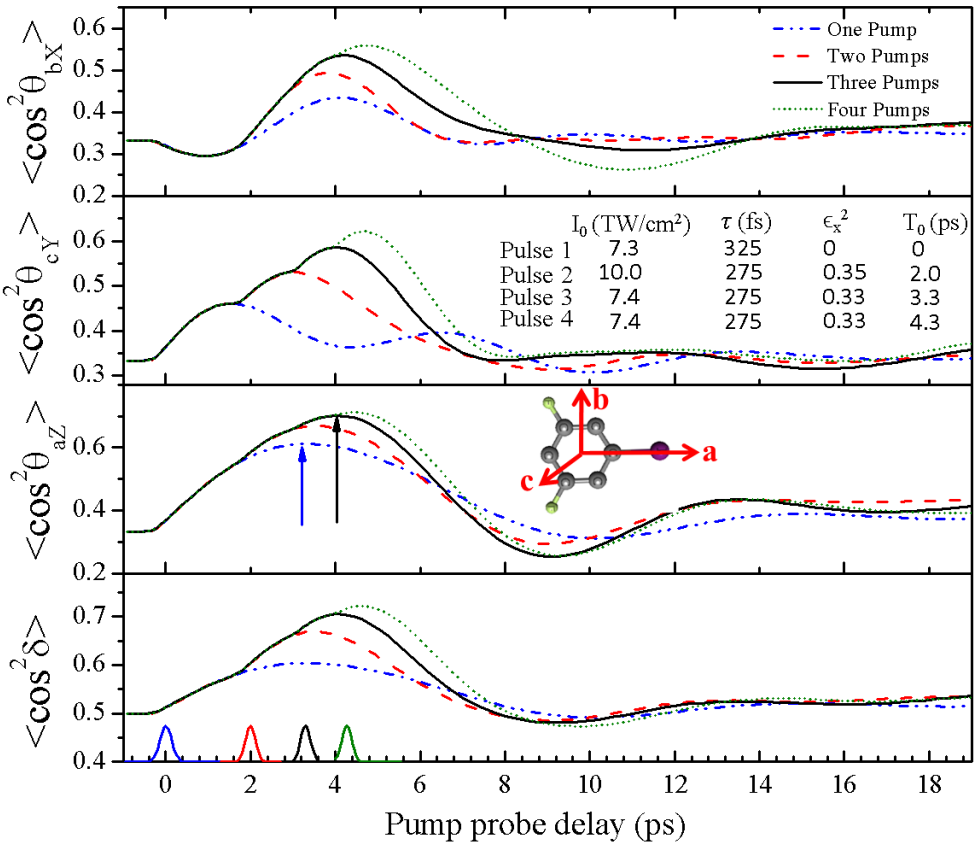

Figure 3.14: *Calculated expectation values of the direction cosines and* $\cos^2\delta$ *for the sequnce of pulses used in the experiment assuming a rotational temperature of 1 K.*

3.3 Symmetry Considerations

As explained in chapter 2 (cf chapter 2 Fig 2.2) asymmetric tops can range from near prolate to near oblate depending on the values of the rotational constants. Ray's asymmetry parameter is often used to quantify where between the two symmetric limits the top lies. In terms of the rotational constants it is written as -

$$\kappa = \frac{2B - A - C}{A - C}. \tag{3.11}$$

$\kappa = -1$ for a prolate top and 1 for an oblate top, and tops with $\kappa < 0$ are often referred to as prolatelike while those with $\kappa > 0$ are oblatelike . We introduce an analogous parameter to characterize the symmetry of the polarizability tensor -

$$\kappa_{pol} = \frac{2\alpha_b - \alpha_a - \alpha_c}{\alpha_a - \alpha_c} \tag{3.12}$$

where the α_i are the polarizabilities along the a,b and c molecular axes. Iodobenzene and DFIB have a value of $\kappa_{pol} = -0.091$ (prolatelike). For molecules with $\kappa_{pol} > 0$ we must reassess the role of the first pulse. For $\kappa_{pol} < 0$, the most polarizable z axis is unique and is picked out easily by the first linearly polarized pulse. In the $\kappa_{pol} > 0$ case however the z axis finds a close companion in the x axis and it is the y axis that is unique in having a significantly weaker polarizability than z and x. In this case a linearly polarized pulse cannot pick out the z axis, but an elliptically polarized can bring the molecule to the plane of polarization[35,72,77], thus picking out the y axis to be aligned along the laser propagation direction. Therefore, for molecules with oblate polarizability the first pulse must be replaced by an elliptically polarized pulse, keeping the rest of the procedure the same.

3.3.1 Thiophene

We demonstrate this numerically using the rotationally prolatelike thiophene molecule which has an oblate polarizability tensor with $\kappa_{pol} = 0.50$. The same prescription is followed here except for the fact that we start with pulses having equal ϵ_X^2, and sequentially increase or decrease the value such that $\langle \cos^2 \delta \rangle$ increases. The result of this procedure is shown in Fig. 3.15. After the five aligning pulses $\langle \cos^2 \delta \rangle = 0.78$. As previously demonstrated[77] a sequence of elliptically polarized pulses does not induce FF3DA in sulfur dioxide. We show by the example of thiophene that such a pulse sequence can induce FF3DA provided the polarizability and inertia tensor of the molecule have the correct symmetry. Preliminary calculations indicate that neither pulse sequence is effective for rotationally oblatelike tops.

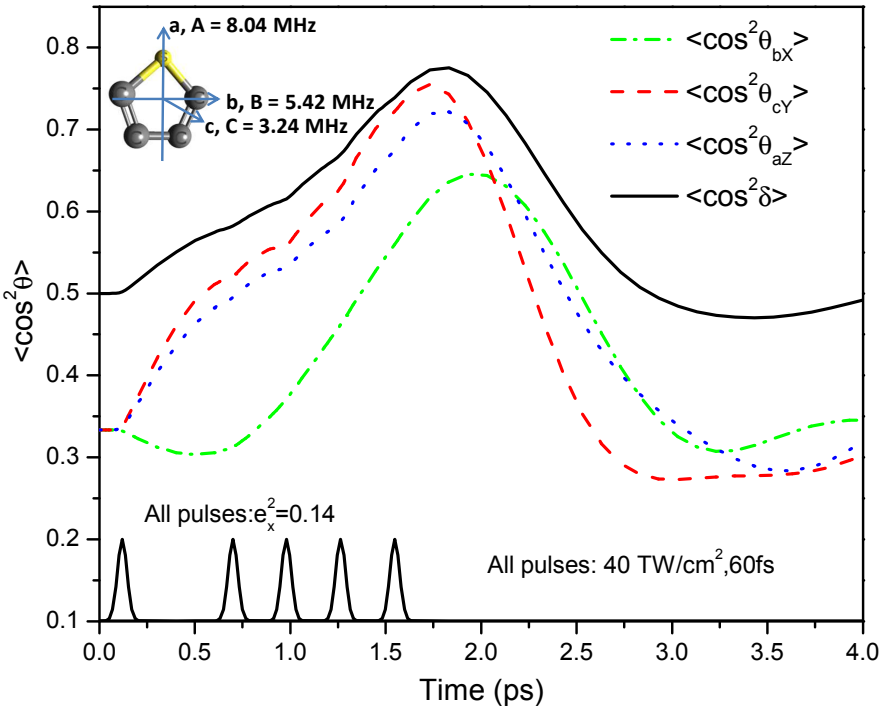

Figure 3.15: *Expectation values calculated using the TDSE for thiophene molecules subjected to five pulses. The figure on the top left shows a thiophene molecule with its a, b and c axes.*

Generalizing the concepts presented here using symmetry arguments may therefore be a task worth attempting.

3.3.2 Uracil

We may go a step further with rotationally prolatelike molecules and study cases for which the polarizability tensor is not diagonal in the principal axes frame. The RNA base uracil is an example of one such molecule. The axes of most and intermediate polarizability (z and x respectively) are in the molecular plane but rotated away from the a and b axes by approximately 4°, and the y and c axes are coincident. Rotating the polarizability tensor into the principal axes frame introduces the additional elements $\alpha_1^2 = -\alpha_{-1}^2$ to the

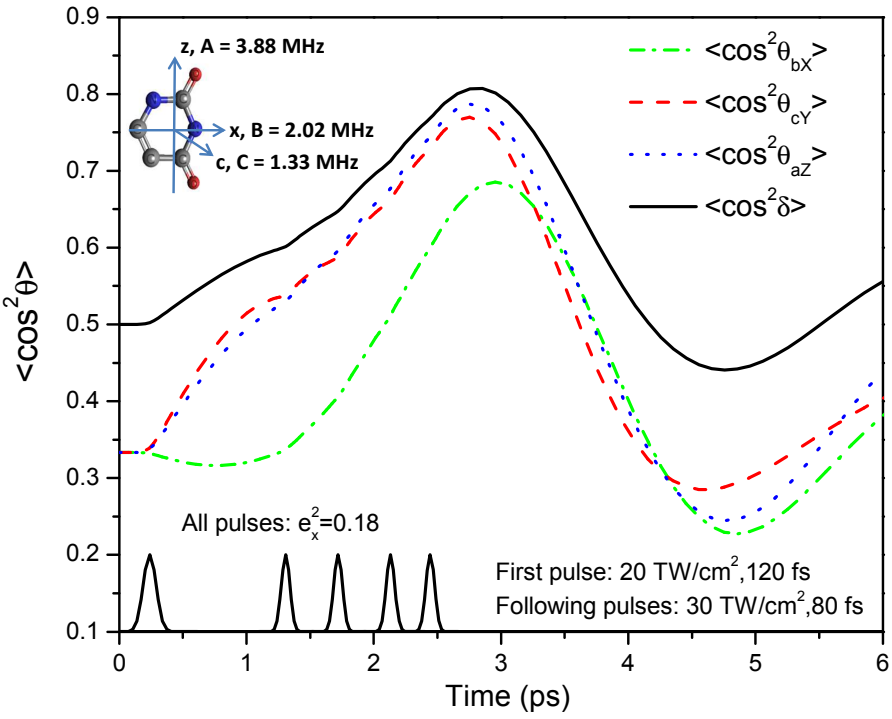

Figure 3.16: *Expectation values calculated using the TDSE for Uracil molecules subjected to five pulses. The figure on the top left shows a uracil molecule with its a, b and c axes.*

spherical polarizability tensor. Using equation 2.12 from chapter 2 yields the interaction potential which now includes terms that excite the coherences $\Delta K = \pm 1$, reflecting the broken symmetry in the molecular frame. Fig 3.16 shows our multipulse prescription applied to uracil. Since uracil has an oblatelike polarizability (even in the principal axes frame), we used an all elliptic pulse sequence. The ellipticity of the pulses was varied in steps and chosen to maximize $\langle \cos^2 \delta \rangle$ which reaches 0.81 indicating that on average the molecules are less than a single 26.5° rotation away from perfect FF3DA. Since the FF3DA persists for about 0.5 ps it could in principal be used in experiments to help illuminate the fast decay of excited uracil molecules, which is a subject of much debate and sometimes controversy in the photochemistry community[44,79,80].

3.4 Summary and Conclusion

In this chapter we developed a new metric for 3D alignment – a single number that indicates the degree of 3D alignment achieved in an experiment or numerical simulation. Perhaps the most valuable insight gained from this development is the nature of the rotational dynamics that need to be induced in order to improve the degree of 3D alignment – the motion of the molecules about their own axes and the space fixed axis must be coordinated. This insight was then applied in the implementation of a scheme to strongly 3D align molecules under field-free conditions. We also discussed the potential and limitations of this scheme.

The possibility of using the metric to optimize FF3DA in an experiment using a feedback algorithm begs the question – Can it be measured? As previously mentioned this requires measuring the full orientation of the molecule, which for some molecules is possible using coincidence techniques under the axial recoil approximation. However the time required to make such measurements precludes their application in such an optimization experiment. In the next chapter we endeavor to find a physical quantity that can be measured relatively quickly and corresponds to $\langle \cos^2 \delta \rangle$.

Chapter 4

An Optical Measurement of Molecular Alignment

In this chapter we present a search for a measurable quantity that that reflects the degree of 3D alignment of a distribution. As a candidate we chose Degenerate Four Wave Mixing (DFWM), a nonlinear process in which three optical waves of the same frequency mix in a material to generate a polarization which also oscillates at the same frequency emitting a fourth optical wave. The characteristics of the fourth optical wave – intensity and polarization– depend on the symmetry of the material, therefore we expect to be able to track the symmetry of a gas as it varies from isotropic to 1D aligned to 3D aligned by measuring the DFWM signal. Though we are unable to show that the signal and the metric are mathematically equivalent, we observe hints that the correct combination of polarization components of the signal may directly reflect the degree of 3D alignment of the sample. The experimental methods and theoretical concepts developed here also serve as tools for experiments detailed in the next chapter.

4.1 Introduction

The general idea behind optical measurements of alignment is that the linear and non-linear optical properties of a material depend on its symmetry[81]. A gas of isotropically distributed molecules has no preferred direction. However if the molecules are aligned, optical properties along and perpendicular to the axis of alignment differ; the gas mimics a birefringent crystal. This fact was first exploited by Heritage, Lin and Gustafson to measure rotational revivals in carbon disulfide[39]. A weak pump pulse excited specific rotational states in CS_2. A weak time delayed probe pulse with its polarization rotated by 45° was sent through the gas and then through a polarizer with its axis orthogonal to the probe polarization. The intensity of light transmitted through the polarizer indicates the birefringence, and thus alignment, induced in the vapor. The same technique was use by Renard et al. to measure impulsive alignment[82]. Other optical measurements followed suit[83,84].

We would like emphasize that optical measurements of alignment have some significant advantages over the VMI measurement used in the previous chapter – they are independent of the axial recoil approximation, they can be used in dense samples and they directly probe the three dimensional moments of the distribution,i.e. $\langle \cos^2\theta \rangle$ rather than $\left\langle \cos^{\theta}_{2D} \right\rangle$. The specific advantages of DFWM will be highlighted in the following section.

4.1.1 Degenerate Four Wave Mixing

To the first order, light impinged on a material generates a polarization that is proportional to the electric field. This polarization is responsible for all the linear optical properties of the material such as the refractive index, and the light emitted by this polarization has the same frequency as the incoming light. However, if the light field is strong enough the generated polarization may be proportional to the square or cube of the incident field, and therefore generate radiation at frequencies different from that of the incident light. In general then the polarization may be written as a Taylor expansion in the incident field[85]. Here we will

focus exclusively on the third order term,

$$P_i^{(3)}(\omega_4, \mathbf{k}_p) = \chi_{ijkl}^{(3)} E_j(\omega_1, \mathbf{k_1}) E_k(\omega_2, \mathbf{k_2}) E_l(\omega_3, \mathbf{k_3}), \tag{4.1}$$

where the Cartesian indices $ijkl$ represent polarization components of the fields $\mathbf{E}(\omega_\mathbf{m}, \mathbf{k_m})$ and the polarization $\mathbf{P}^{(3)}(\omega_4, \mathbf{k}_p)$, ω_m and $\mathbf{k_m}$ are the field frequencies and propagation vectors, ω_4 and $\mathbf{k}_p$ being the oscillation frequency and wave vector of the polarization. $\chi_{ijkl}^{(3)}$ is a material dependent fourth rank tensor, called the third order susceptibility tensor, which characterizes the third order response of the material. We would like to remind the reader that the Einstein summation convention always applies unless specified. The susceptibility must be a tensor since the response of the material can be different in different directions, however the majority of the 81 elements are zero when the symmetry of the medium is considered. We may write the field components in the form $E_j(\omega_m, \mathbf{k_m}) = A_j^{(m)} \exp[i(\mathbf{k_m} \cdot \mathbf{r} - \omega_m t)] +$ (complex conjugate) where A_j is the amplitude of the component.

Adopting the convention that a negative frequency corresponds to the complex conjugate and substituting this in eq 4.1 results in several frequency components for the polarization and thus the generated light. We state only a few interesting cases here,

$$\begin{aligned}
P_i^{(3)}(3\omega_1) &= \chi_{ijjj}^{(3)} (A_j^{(1)})^3 \exp[i(3\mathbf{k_1} \cdot \mathbf{r} - 3\omega_1 t)], \\
P_i^{(3)}(\omega_1 + \omega_2 + \omega_3) &= \chi_{ijkl}^{(3)} A_j^{(1)} A_k^{(2)} A_l^{(3)} \exp[i((\mathbf{k_1} + \mathbf{k_2} + \mathbf{k_3}) \cdot \mathbf{r} - (\omega_1 + \omega_2 + \omega_3)t)], \\
P_i^{(3)}(\omega_1 - \omega_2 + \omega_3) &= \chi_{ijkl}^{(3)} A_j^{(1)} A_k^{(2)} A_l^{(3)} \exp[i((\mathbf{k_1} - \mathbf{k_2} + \mathbf{k_3}) \cdot \mathbf{r} - (\omega_1 - \omega_2 + \omega_3)t)],
\end{aligned} \tag{4.2}$$

The first of these represents third harmonic generation, since the frequency of the generated light is triple the frequency of the incident light.The second represents a process in which three incident fields of frequencies ω_1, ω_2 and ω_3 generate radiation at the sum of the three frequencies. The third represents a process known as Coherent Anti-Stokes Raman Scat-

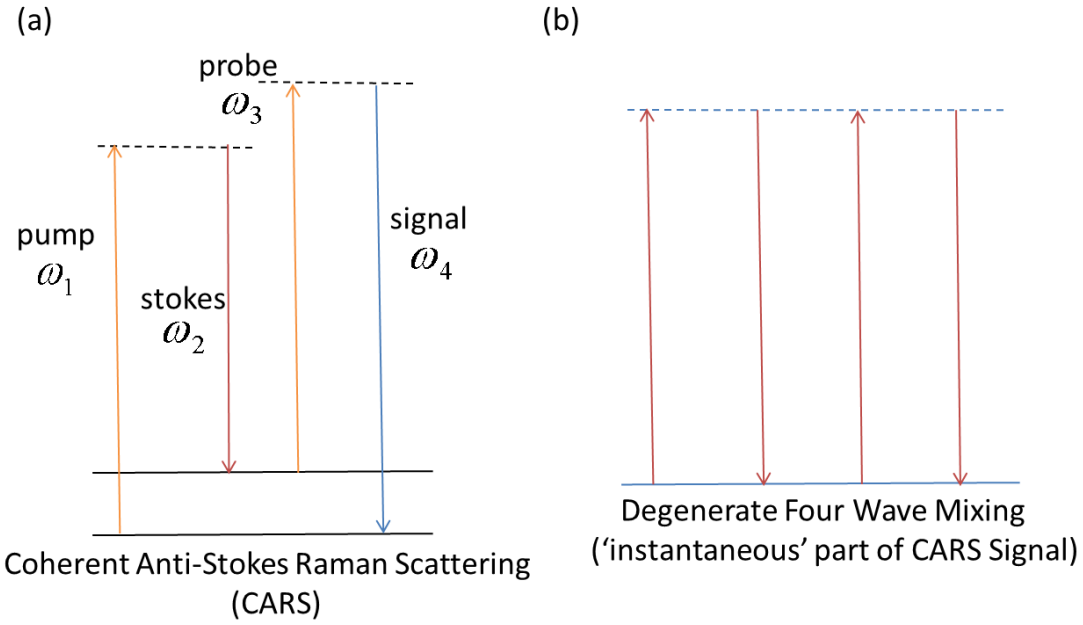

Figure 4.1: *Photon pictures for (a) CARS and (b) DFWM*

tering (CARS) or Coherent Stokes Raman Scattering (CSRS), in which light at frequency ω_1 is absorbed, followed by emission at ω_2, then absorption at ω_3 and finally emission at a blue (anti-Stokes) or red (Stokes) shifted frequency ω_4[86]. A photon diagram of this process is shown in panel Fig. 4.1 (a). As is evident the frequency of the emitted light depends on the spacing of energy levels in the material – $\omega_4 = \omega_3 + \Delta E$. As a result CARS and CSRS prove to be invaluable spectroscopic tools, especially since transitions that are one-photon forbidden can be accessed[86,87,88,89].

Our laser produces pulsed light at 790 nm with a bandwidth (FWHM) of 32 nm. When these pulses are incident on a gas sample CARS can occur via mixing of different frequency components within the bandwidth. However the process in panel (b) of Fig. 4.1 in which the photon frequencies are degenerate is significantly faster as it involves no resonant excitation, and thus dominant. CARS and CSRS spectroscopist work hard to eliminate this contribu-

tion from their measurement, but this is the contribution in which our interest lies. Setting $\omega_1 = \omega_2 = \omega_3 = \omega$ in the CARS polarization gives the polarization for this process which also oscillates at ω, and hence the process is termed Degenerate Four Wave Mixing (DFWM) . Note that this does not necessarily mean $\mathbf{k}_1 = \mathbf{k}_2 = \mathbf{k}_3$ since we may split our laser beam into three weaker beams which propagate in different directions and combine at the gas target to generate the third order polarization. In Eq. 4.2 the generated polarizations have wave vectors which are different combinations of the input wave vectors. Therefore, provided directions of prorogation of all the three incident light waves are different, the direction of the emitted light in the case of third harmonic generation, sum frequency generation and CARS or CSRS will be different. Specifically, for any nonlinear process light will be emitted in a direction specified by the 'phase matching' condition $\mathbf{k}_p = \mathbf{k}_4$, $\mathbf{k}_4$ being the wave vector of the emitted light wave and $\mathbf{k}_p$ being the polarization wave vector controlled by the wave vectors of the incident light. We use BOXCARS phase matching depicted in Fig. 4.2 in which the three input beams occupy three corners of a square on a focusing lens[89]. The beams then focus at the same point and the DFWM signal is emitted at the fourth corner of the square in accordance with the phase matching condition $\mathbf{k}_4 = \mathbf{k}_1 - \mathbf{k}_2 + \mathbf{k}_3$. DFWM can therefore be a background free measurement, a significant advantages over other optical techniques.

The polarization for CARS in eq 4.2 with $\omega_1 = \omega_2 = \omega_3 = \omega$ can be substituted in Maxwell's wave equation to generate a solution for the emitted optical wave. Under the slowly varying envelope approximation and assuming that the energy lost by the input waves is negligible, the amplitude of the emitted wave is given as follows,

$$A_i^{(4)} = \frac{3i\omega_4}{2n_4c}\chi_{ijkl}A_j^{(1)}A_k^{(2)}A_j^{(3)}L \tag{4.3}$$

where n_4 is the refractive index of the medium at ω_4, c is the speed of light and L is the length of the medium along the phase matching direction. A detailed discussion can be found in chapter 10 of Boyd[85]. The relatively low number density in the experiment allows

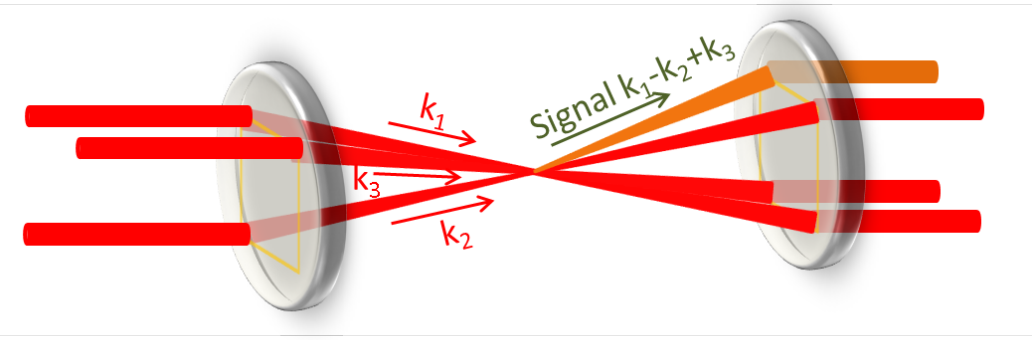

Figure 4.2: *DFWM in the BOXCARS phase matching geometry.*

for this approximaion. Our central concern is that the intensity of the signal is proportional to the square of a susceptibility tensor element. Since the symmetry of the medium changes as the gas goes from isotropic to 3D aligned we expect the susceptibility to vary while all the other parameters remain constant. We will discuss the exact connection between the orientation of molecules in a gas and the susceptibility in section 4.2.2 discussing the modeling of the experimental data. In the next section we describe the experimental setup used to measure the DFWM signal from aligned molecules.

4.2 Measuring alignment with DFWM

In the experiment we use a single 790 nm, 18 TW/cm^2 60 fs pump pulse to populate a rotaional wave packet in iodobenzene. We track the evolution of the molecular axis distribution with three temporally and spatially overlapped 30 fs pulses in a BOXCARS configuration that are delayed with respect to the pump pulse. The experimental setup is shown in Fig. 4.3. Unlike the VMI experiment this experiment is performed 1 mm from the exit of nozzle of the 1 kHz pulsed jet, since the generation of the signal is a manifestly macroscopic process requiring a larger number of molecules. The pump and probe beams

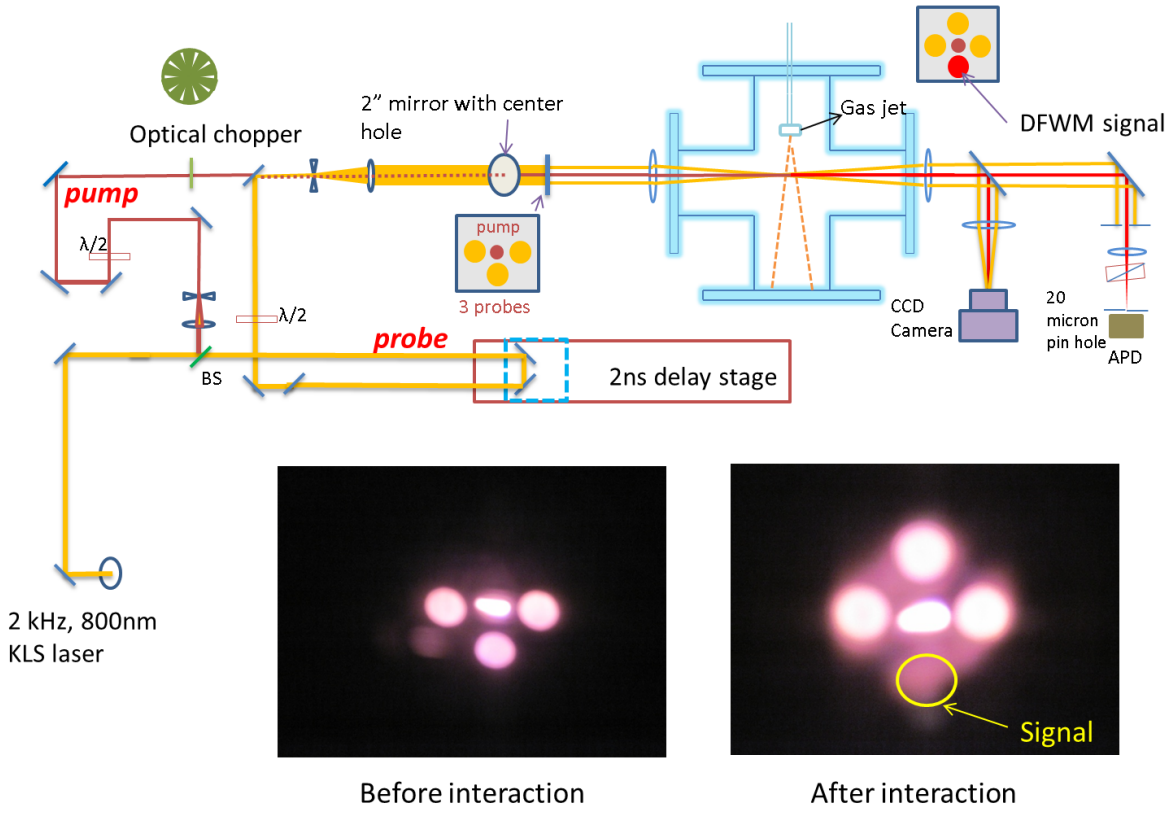

Figure 4.3: *A drawing of the experimental setup for measuring molecular alignment with DFWM. The 'before interaction' photograph shows the input DFWM beams with the alignment beam in the center and the 'after interaction' photograph, taken after the focus, shows the input beams with the signal generated from air at the fourth corner of the square.*

are derived from the 2 mJ, 30 fs, 2 kHz KLS pulses using a 50/50 beamsplitter. The four DFWM beams are then derived from a single probe beam which is expanded to a diameter of 2 inches and incident on an 2 inch mirror with a hole in the center followed by a 50×50 mm aluminum mask with three 8 mm holes drilled at three corners of a 10×10 mm square. The loss in intensity through the mask also ensures that each pulse independently is too weak to excite any third order processes in the medium. The use of such a mask also obviates the need for careful alignment of the DFWM beams as they are automatically spatially and temporally overlapped and jitter free. The pump beam is sent through the 6 mm hole

in the mirror and then through a 6 mm hole drilled in the center of the aluminum plate. All the beams are focused by a 2 inch diameter, 35 cm focal length lens with the pump at the center. A second 35 cm lens after the chamber collimates the beams, after which an iris selects the DFWM signal. A 20 cm lens then images the interaction region on a 50 μm pinhole after which the signal is incident on an avalanche photo detector (APD). The cube polarizer before the pinhole is used to select the polarization component of the signal. Photographs of the beams before and after the interaction region are shown in Fig. 4.3, where the visible DFWM signal is generated from air at atmospheric pressure. This signal is used to align the detection optics.

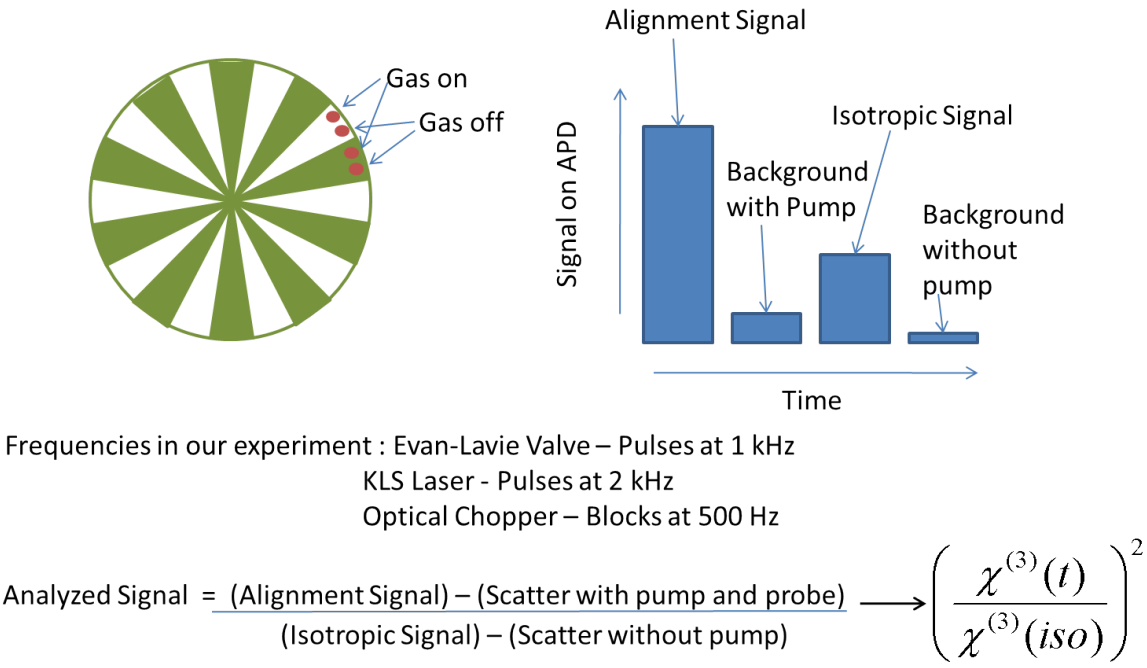

Figure 4.4: *A depiction of the role of the chopper in the experiment along with the signals generated as a result of the different repetition rates of the laser, gas jet and chopper The analyzed signal is proportional to the ratio of susceptibilities of an aligned gas and an isotropic gas.*

The addition of an optical chopper in the pump beam allows for real time normalization

of the signal.The chopper runs at 500 Hz blocking two consecutive pulses and letting the next two through. The pump pulse train thus consists of pairs of pulses with each pair separated by 1 ms with a spacing of 500 μs between pulses in each pair. With a probe pulse arriving at the interaction region every 500 μs and a gas pulse arriving every 1 ms, we measure four different signal pulses separated by 500μs – (1) signal with the pump unblocked and gas pulse present, (2) signal with the pump unblocked and no gas, (3) signal with the pump blocked and gas present and (4) signal with the pump blocked and no gas. (1) is the DFWM signal from the rotational wave packet, (2) serves as a measure of the background with the pump pulse present (3) is the DFWM signal from an isotropic gas sample and (4) is a measure of the background without the pump. The signal is background subtracted and normalized – $\frac{(1)-(2)}{(3)-(4)}$– and is equal to the ratio of the time dependent susceptibility of the rotationally excited gas to that of an isotropic sample – $(\chi_{ijkl}(t)/\chi_{ijkl}(iso))^2$. Fig. 4.4 depicts the operation of the chopper and the resulting area of the signal pulse on the APD as a function of time.

The signal area is measured by sending the APD signal into a Stanford Research Systems (SRS) gated integrator triggered by the laser at 2 kHz. The signal output of the integrator as well as a 2 kHz digital output that is high when the integrator is busy are transfered to a computer via a National Instruments data acquisition card (DAQ card). The chopper and gas jet are triggered at 1 kHz by a SRS delay generator which is triggered by the laser and internally divides the 2 kHz rate to 1 kHz. The digital output from the channel used to divide the rate is also read by the DAQ card. The chopper internally divides the 1 kHz trigger to 500 Hz and provides a synchronized reference output which is also sent to the DAQ card. The three digital signals are used to segregate the integrated APD signal into the four signals in Fig. 4.4 and calculate the normalized signal on-the-fly.

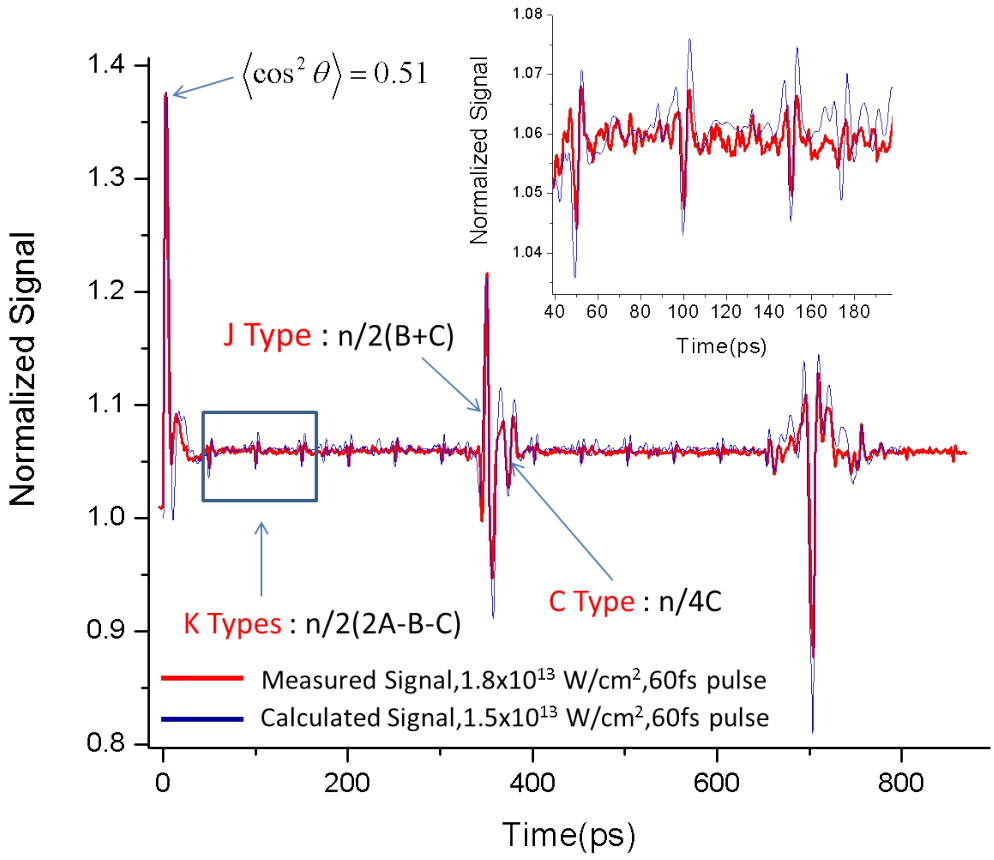

Figure 4.5: *The normalized DFWM signal from a rotationally excited gas of iodobenzene molecules. The observed rotational coherences are marked and the inset zooms in on the K-type coherences.*

4.2.1 Results and Discussion

Fig. 4.5 shows the DFWM signal from a gas of iodobenzene molecules as a function of the delay between the pump and the DFWM pulses. The DFWM pulses are polarized parallel to pump beam (in the Z direction) as is the measured component of the signal. Each data point is averaged over 1000 cycles of four pulses each. When the pump arrives before the probe (negative delays) the signal is near 1 since the molecules have not been rotationally excited. After the pump pulse the signal rises sharply indicating that the χ_{ZZZZ}

susceptibility component of the gas is increasing. As we know from calculations presented in the previous chapter this corresponds to the molecular a-axis (C-I axis) aligning along the Z axis (c.f. $\langle\cos^2\theta_{zZ}\rangle$ in Fig. 3.4, chapter 3), indicating that χ_{ZZZZ} for iodobenzene increases as the molecular a-axis comes into alignment. We also observe the J and C-type revivals of a-axis alignment at the expected delays. However, we additionally observe K-type revivals spaced by 50.3 ps only observed in $\langle\cos^2\theta_{xX}\rangle$ and $\langle\cos^2\theta_{xX}\rangle$ in the calculations in chapter 3 (c.f Fig. Fig. 3.4 therein). This is a clear indication that the measured signal is sensitive to the rotational motion of the b and c molecular axes as well. This is another reason for the choice of DFWM as a potential measure of 3D alignment. It is the lowest order nonlinear process that is sensitive to 3D rotational motion.

4.2.2 Modeling the Data

In attempting to understand the origin of this sensitivity we must begin with the molecular frame dipole and its interaction with the laser fields. Like the polarization of macroscopic materials the molecular dipole can also be expanded as a Taylor series in the electric field, with the induced third order dipole given by,

$$\mu_i^{(3)}(\omega_4, \mathbf{k}_p) = \gamma_{ijkl}^{(3)} E_j(\omega_m, \mathbf{k_m}) E_k(\omega_n, \mathbf{k_n}) E_l(\omega_o, \mathbf{k_o}). \tag{4.4}$$

Here γ_{ijkl} is the second molecular hyperpolarizability tensor. Since the molecule is symmetric under the C_{2v} point group only 6 unique tensor components remain and degeneracy of the field frequencies adds 15 non-unique components[90]. The tensor must be calculated using quantum chemical methods, but those for iodobenzene have been calculated by Matsuzawa and Dixon[91]. They are tabulated in appendix C. The polarization is given by the average of the dipole in the lab frame, thus rotating this tensor to the lab frame and averaging over all molecular orientations gives the susceptibility tensor. Calling the lab frame hyperpolarizability $[\gamma_{ijkl}]^L$ we can rewrite Eq. 4.1 as,

$$P_i^{(3)}(\omega_4, \mathbf{k}_p) = \frac{N_b}{\epsilon_0} \left\langle [\gamma_{ijkl}]^L \right\rangle E_j(\omega_m, \mathbf{k_m}) E_k(\omega_n, \mathbf{k_n}) E_l(\omega_o, \mathbf{k_o}),$$

$$[\gamma_{ijkl}]^L = R_{im} R_{jn} R_{ko} R_{lp} \gamma_{mnop}. \tag{4.5}$$

where N_b is the number density of molecules, ϵ_0 is the permitivity of free space and the R_{ij} are elements of the 3D rotation matrix. For our experiment the angle brackets refer to an average over the rotational wave packet at each time delay, which can be calculated using the method detailed in chapter 2. Specifically, the expectation value of a lab frame component of the hyperpolarizability tensor can be calculated using Eq. 1.20 and 1.21 from chapter 2 provided its matrix elements in the $|JKM\rangle$ basis are known. These are easier to determine if we transform both tenors to spherical tensors,

$$\begin{aligned} \gamma_m^j &= C_{j,m}^{ijkl} \gamma_{ijkl}, \\ \chi_m^j(t) &= \left\langle [\gamma_m^j]^L \right\rangle (t) = \left\langle D_{m,m'}^j \right\rangle \gamma_{m'}^j, \\ \chi_{ijkl}(t) &= C_{ijkl}^{j,m} \chi_m^j(t) \end{aligned} \tag{4.6}$$

Since these are fourth rank tensors $j = 0, 1, 2, 3, 4$ and $m = -j, -j+j, ..0, ..j-1, j$ for every j and t is the time delay after the pump. We state the conversion for the measured component χ_{ZZZZ} here giving expressions used to calculate the conversion coefficients in appendix B,

$$\chi_{ZZZZ}(t) = 0.338061 \left\langle [\gamma_0^4]^L \right\rangle (t) - 0.918645 \left\langle [\gamma_0^2]^L \right\rangle (t) + 0.668219 \left\langle [\gamma_0^0]^L \right\rangle (t). \tag{4.7}$$

We therefore need to calculate the three time dependent expectation values in the above equation to simulate our data. Further, since we measure the square of the susceptibility component we square the lab frame hyperpolarizability matrices before calculating the expectation values. $(\chi_{ZZZZ}(t)/\chi_{ZZZZ}(iso))^2$ is plotted in blue in Fig. 4.5 over the data. The intensity and rotational temperature were adjusted to achieve satisfactory agreement be-

tween the data and calculation resulting in a temperature of 8 K. This may be considered as an experimental estimate of the rotational temperature showing that the experiment serves as a rotational thermometer. The associated calculated value of $\langle \cos^2 \theta \rangle$ at the alignment peak is 0.51, providing an estimate of the degree of alignment.

The origin of the K-type revivals can be elucidated by writing the relevant matrix elements of the lab frame hyperpolarizability,

$$\langle JKM | \, [\gamma_0^j]^L \, | J'K'M' \rangle = \sqrt{\frac{2J+1}{2J'+1}} \, \langle J, M; j, 0 | J'M' \rangle \, \langle J, K; j, k | J,' K' \rangle \, \gamma_k^j. \tag{4.8}$$

For $j = 2$ and $j = 4$, $k = -2, -1, ..., 2$ and $k = -4, -3, ..., 4$ respectively. χ_{ZZZZ} is therefore sensitive to coherences between states in the wave packet that have K values different by $0, 1, 2, 3$ and 4. Since states with $\Delta K = \pm 2, \pm 4$ participate in K-type revivals, they are observed in the measurement. Though the measurement is sensitive to odd ΔK coherences none are excited by the pump interaction Hamiltonian as discussed in chapter 2. Also note that squaring the matrix adds $j = 8$ and 6 and $\Delta K = \pm 6, \pm 8$ which also contribute to the K-type revivals. We also see however that χ_{ZZZZ} is not sensitive to any ΔM coherences. As we learned in the previous chapter a measure of 3D alignment must be sensitive to both ΔK and ΔM coherences. We must therefore attempt to measure other components of the susceptibility tensor.

4.2.3 The possibility of measuring 3D alignment

Another component that is easily accessible given our experimental setup is χ_{XXXX}. We simply rotate the polarization of all the DFWM beams by 90° using the $\lambda/2$ plate in the probe beam and rotate the polarizer in the signal by 90° to detect the X component. Additionally, we split the pump pulse into two time delayed perpendicularly polarized pulses by sending it through a pulse shaper. The design and construction of the shaper will not be presented here since it has been the subject of a previous thesis[63]. Briefly, the spectrum

of the pulse is horizontally dispersed by a 1200 lines/mm grating after which its vertical dimension is focused by a 35 cm focal length cylindrical mirror through a dual mask liquid crystal spatial light modulator. The beam is then re-collimated by another cylindrical mirror-grating pair. The controllable axes of each liquid crystal mask are perpendicular and at 45° to the polarization of the input light allowing a different linear phase to be added to each component producing two time delayed cross polarized pulse. The time delay can be controlled by the phase difference between the components.

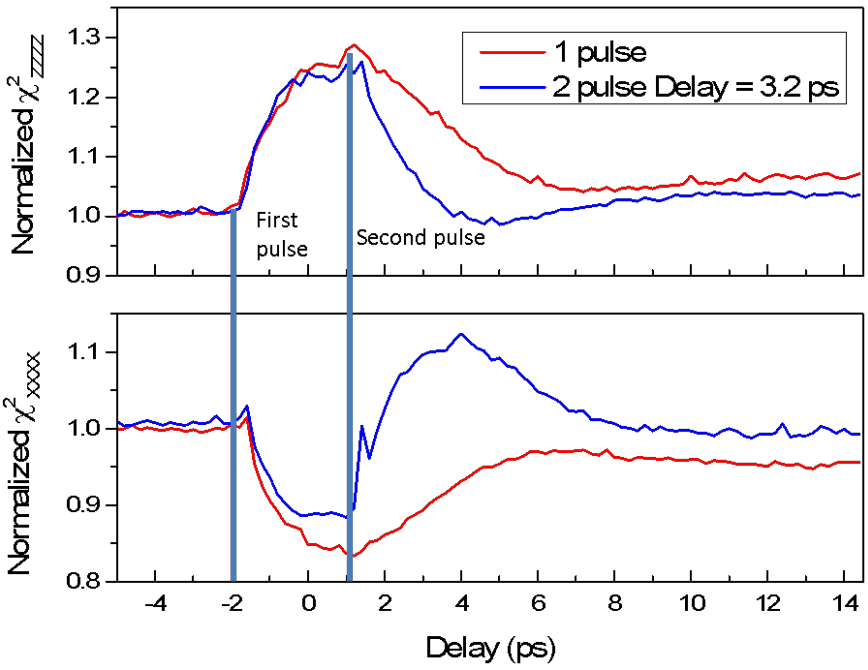

Figure 4.6: *Normalized DFWM signals for the ZZZZ and XXXX susceptibility components from iodobenzene aligned with one pulse and two orthogonal time delayed pulses. The first is a 4.6 TW/cm^2, 340 fs pulse and the second is a 12 TW/cm^2, 130 fs pulse.*

Delay scans between the pumps and DFWM pulses for the χ_{XXXX} and χ_{ZZZZ} components are shown in fig 4.6 for a 3.2 ps separation between the pumps. The only apparently noticeable behavior is that χ_{XXXX} has an opposite alignment dependence to χ_{ZZZZ}. We may calculate χ_{XXXX} by first writing it in terms of spherical hyperpolarizability tensor

components as follows,

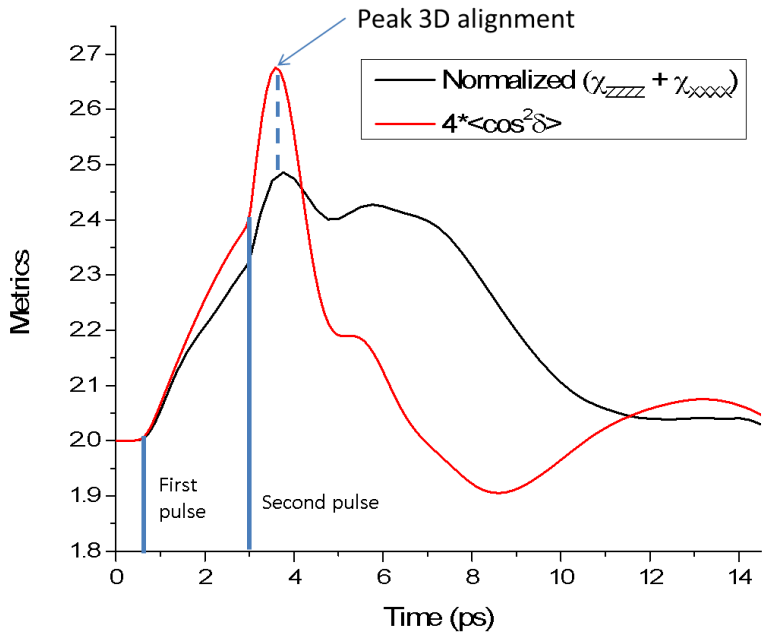

Figure 4.7: *Calculated sum of the XXXX and ZZZZ susceptibilty components compared with* $\langle \cos^2 \delta \rangle$ *for the experimental pulses, but separated by 2.6 ps.*

$$\chi_{XXXX} = 0.179284 \left\langle [\gamma_0^4]^L \right\rangle + 0.649579 \left\langle [\gamma_0^2]^L \right\rangle - 0.649579(\left\langle [\gamma_2^2]^L \right\rangle + \left\langle [\gamma_{-2}^2]^L \right\rangle)$$
$$+0.25(\left\langle [\gamma_4^4]^L \right\rangle + \left\langle [\gamma_{-4}^4]^L \right\rangle) - 0.188982(\left\langle [\gamma_2^4]^L \right\rangle + \left\langle [\gamma_-^4 2]^L \right\rangle) + 0.631476 \left\langle [\gamma_0^0]^L \right\rangle . \quad (4.9)$$

The matrix elements for γ_m^j's with $m = \pm 2$ and ± 4 include $\Delta M = \pm 2, \pm 4$ coherences, however these are paired with any of the possible ΔK coherences including $\Delta K = 0$. As we discovered in the previous chapter a measure of 3D alignment must be sensitive only to coherences in which M and K change together. One may hope however that the coupled terms dominate, but each term is weighted by the cartesian-to-spherical conversion coefficients and components of the molecular hyperpolarizability making the terms hard

to untangle. This becomes even harder when we consider that the relevant quantities are squares of the matrices. Further, from the experimental data it appears that χ^2_{XXXX} decreases as the molecules align with the Z-axis, and then beings to increase after the second pulse when presumably the molecules approach some degree of 3D alignment. A similar but opposite inversion behavior is also observed in χ^2_{ZZZZ}. Neither of these therefore is a suitable measure of 3D alignment, but perhaps some combination of the two will suffice.

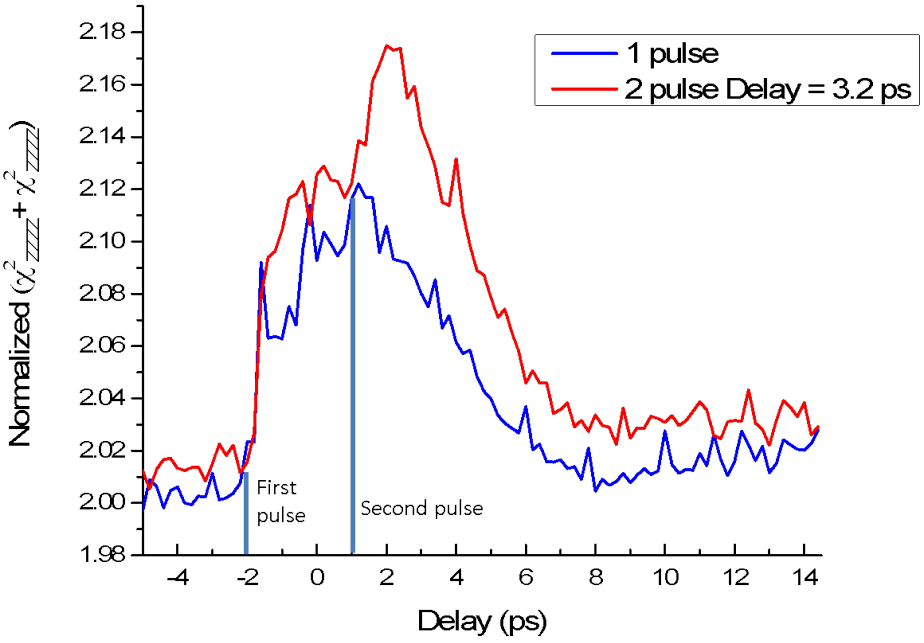

Figure 4.8: *Normalized DFWM signals for the ZZZZ and XXXX susceptibility components added together from iodobenzene aligned with one pulse and two orthogonally time delayed pulses.*

We explore the most obvious combination – $(\chi^2_{XXXX} + \chi^2_{ZZZZ})$. Since calculating the squares is an expensive proposition we calculate $(\chi_{XXXX} + \chi_{ZZZZ})$ for pulse intensities used in the experiment, but for a pulse seperation of 2.6 ps at a temperature of 0.05 K. This is plotted in Fig. 4.7 with $\langle \cos^2 \delta \rangle$ for the same pulse parameters and temperature. Clearly, both curves peak at the same time delay of about 3.7 ps. This indicates that

terms in $(\chi_{ZZZZ} + \chi_{XXXX})$ relevant for 3D alignment do in fact dominate for iodobenzene. Fig. 4.8 shows the corresponding measured curves for 1 pulse and 2 pulses. The behavior is qualitatively similar to the calculation with the signal increasing after second pulse. However it does fall away much faster after the peak, likely to due the 8 K rotational temperature as opposed to 0.05 K. Though preliminary, this is an indication that $(\chi^2_{XXXX} + \chi^2_{ZZZZ})$ may directly reflect the 3D alignment of the distribution.

4.3 Summary and Conclusion

In this chapter we explored the possibility of using DFWM as a measure of 3D alignment. We measured delay dependent changes in components of the third order susceptibility tensor of a molecular gas rotationally excited by a separate pump beam. Selecting polarizations of the DFWM and signal beams allowed us to select the measured susceptibility component. We found that the component for which the DFWM and signal beams have the same polarization as the pump beam $-\chi_{ZZZZ}$ – increases in concert with the degree of a-axis alignment and exhibits K-type revivals which indicates that it is sensitive to the rotational motion of the b and c axes as well. Matrix elements of the component in the $|JKM\rangle$ basis explain why these revivals are observed, however they also show that this component alone cannot serve as a measure for 3D alignment. We then measured the component for which the DFWM and signal beams are polarized perpendicular to the pump beam – the χ_{XXXX} component. Without rigorous proof, but through numerical simulation and qualitative comparison with measurement we found that the sum of the measured components $-\chi_{ZZZZ} + \chi_{XXXX}-$ may serve as a measure of 3D alignment.

An essential advantage of developing such a measurement scheme is that since a single measurement (1000 cycles) of the DFWM signal takes about 350 ms, it can be combined with a feedback algorithm which shapes the aligning pulse in such a way as to optimize the signal and therefore the alignment of the molecules. Further, a measure of 3D alignment

in a dense sample is needed if processes such as high harmonic generation, which require a dense sample, are to be measured from 3D aligned molecules.

Chapter 5

Angle-Resolved Ionization and Fragmentation in a Strong Field

To fuel our imagination we look for limitations of the work presented thus far. Though the scheme detailed in chapter 3 produces strong FF3DA, as was the case with 3D alignment experiments mentioned in the introduction, the experimental geometry precludes angle dependent measurements resolved in the Euler angle χ. For instance, in the case of strong field ionization of linear molecules it has been shown that the ion yield as a function of the angle between the molecular axis and the polarization of the ionizing laser pulse reflects the symmetry of the orbital from which the electron is removed[45,15]. In the case of the aligned distribution of DFIB in chapter 3 or iodobenzene in chapter 4 the polar alignment angle θ can be controlled by the polarization of the aligning pulses, but χ cannot. How then can one make similar yield measurements for an asymmetric top molecule as a function of θ and χ ?

In this chapter we attempt to break this impasse. It is always possible to measure the delay dependence of the process with respect to a pump pulse that rotationally excites the molecules. As shown in chapter 2, the wave packet excited by such a pump pulse is a function of both the polar angle θ and the rotation angle of the molecular plane χ (cf Fig. 5.1). This

unique property of asymmetric tops allows the extraction of the fully resolved alignment dependence of the process. In the following sections we develop and apply this idea to the strong field ionization of ethylene to measure, for the first time, the fully angle resolved yield of an asymmetric top molecular ion. From the results of the measurement we are able to ascertain the electronic states populated in the ion. Similarly, angle resolved yields of charged fragments indicate from which ionic state the fragmentation processes initiated.

5.1 Alignment angle dependent yields

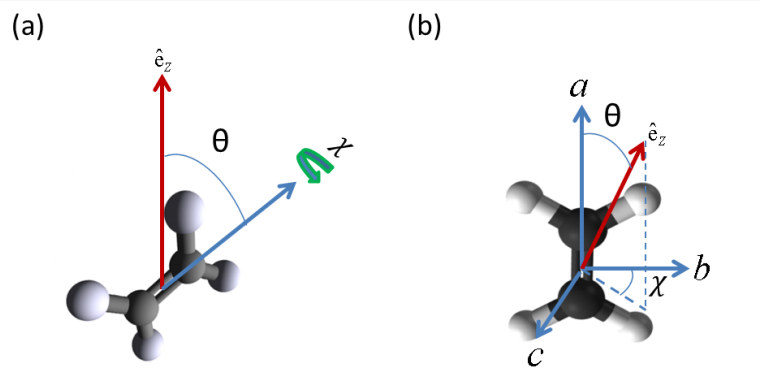

Figure 5.1: *(a) and (b) show the alignment angles in the lab and molecule fixed frames respectively.*

The experiment we would perform if it were possible would be to rotate 3D aligned molecules to any molecular orientation and measure the probability that a specific light induced process will occur. Although the following discussion applies to any process which allows the separation of rotational and vibronic degrees of freedom, to maintain fluidity in the following discussion we assume the process is photionization – removal of a single electron from the valence orbital(s) of an asymmetric top molecule. We only deal with linearly polarized light, in which case cylindrical symmetry about the polarization axis dictates that the ion yield must be independent of the azimuthal Euler angle ϕ. Panel (a) in Fig. 5.1 shows the relevant alignment angles θ and χ, for ϕ fixed such that the molecular

a axis is in the plane of the page. Fig 5.1(b) shows the same angles in the molecular frame, where χ becomes the azimuthal angle of the laser polarization vector. Since the Wigner functions $D^j_{m,k}(\theta,\phi,\chi)$ are an irreducible representation on the rotation group SO(3)[52] the angle dependent ion yield can be expanded as

$$S(\theta,\chi) = \sum_{j,k} C_{j,k} D^j_{0,k}(\theta,\chi), \tag{5.1}$$

where $m = 0$ reflects the cylindrical symmetry about the Z axis in the lab frame, and equivalently the absence of a third angle in the molecular frame. We may therefore consider our task as measurement of the coefficients $C_{j,k}$. We can qualitatively investigate how these coefficients relate to the physics of photionzation.

In the experiments that follow we use laser pulses with a significantly lower photon energy than the ionization potential (I.P.) of the molecule, but intense enough to result in ionization via the absorption of multiple photons. In general the differential ionization rate for multiphoton ionization for a molecule aligned at $\mathbf{\Omega} = \{\theta,\chi\}$ in an initial state $|i\rangle$ to a final state $|f\rangle$ emitting an electron in with momentum $\mathbf{k} = k\hat{\mathbf{k}}$ is given by a sum over all squared n-photon ionization amplitudes[92,93],

$$\begin{aligned} \frac{dW}{d\mathbf{\Omega} d\hat{\mathbf{k}}} &= 2\pi \sum_{n=n_0}^{\infty} |A_{k_n}(\mathbf{\Omega},\hat{\mathbf{k}})|^2 k_n \\ A_{k_n} &= \frac{1}{T}\int_0^T (\langle f|\, V\, |i\rangle)_t dt, \end{aligned} \tag{5.2}$$

where V is the dipole potential felt by all electrons in the laser electric field, k_n is the momentum of the ionized electron after the absorption of n photons and the subscript t indicates that everything in the brackets is time dependent. A number of approximation are usually made to make calculations in strong fields tractable. In general the states $|i\rangle$ and $|f\rangle$ must be dressed by the time dependent field, however the initial state is usually considered to be the field-free ground state of the neutral and the final state is considered to

be a product of a field dressed electron, or Volkov state, and the field-free ground state of the ion in which all particles are approximated as frozen. These approximations are collectively referred to as the strong field approximation (SFA)[92,94].

In the limit of large photon orders the SFA rate reduces to the adiabatic tunneling rate, which can be independently derived assuming that the field is static and the rate is given by the square of the wave function of the valence electron beyond the the field dressed potential barrier[95,45]. For a qualitative understanding of Eq. 5.1 we may write a general version of the wave function of the electron beyond the barrier without considering its specific form

$$\Psi(r_e, \theta_e, \chi_e) = \sum_{l,\lambda} A_{l,\lambda} Y_{l,\lambda}(\theta_e, \chi_e) F_{l,\lambda}(r_e), \tag{5.3}$$

where $\{r_e, \theta_e, \chi_e\}$ are coordinates of the valence electron and $F_{l,\lambda}(r_e)$ are radial basis wave functions. $A_{l,\lambda}$ are real coefficients of the basis set expansion and the allowed values of $\{l, \lambda\}$ are decided by the symmetry of the of the valence electron orbital. The $Y_{l,\lambda}$ can be rotated into the lab frame with the Wigner rotation matrices, and the differential ionization rate is then given by the square of the wave function[96],

$$\frac{dW}{d\mathbf{\Omega} d\mathbf{R}} = \sum_{l,m,\lambda} \sum_{l',m',\lambda'} A_{l,\lambda} A_{l',\lambda'} D^{l}_{-m,-\lambda}(\mathbf{\Omega}) D^{l'}_{m',\lambda'}(\mathbf{\Omega}) Y_{l,m}(\Theta, \Phi) Y^{*}_{l',m'}(\Theta, \Phi) F_{l,m}(R) F^{*}_{l',m'}(R), \tag{5.4}$$

where $\{R, \Theta, \Phi\}$ are electronic coordinates in the lab frame. To get the alignment angle dependent yield this must be integrated over the electronic coordinates. Integration of the spherical harmonics product pair gives the Kronecker delta functions $\delta_{l,l'}\delta_{m,m'}$. Reducing the product of Wigner functions to a sum using CG coefficients gives an expression for the

coefficients in Eq. 5.1

$$S(\theta,\chi) = \frac{dW}{d\hat{\mathbf{\Omega}}} = \sum_{j,k} C_{j,k} D^{j}_{0,k}(\theta,\chi),$$
$$C_{j,k} = \sum_{l,m,\lambda,\lambda'} \langle l,-m;l,m|j,0\rangle \langle l,-\lambda;l,\lambda'|j,k\rangle A_{l,\lambda} A_{l,\lambda'} d_{l,m}, \tag{5.5}$$

where $d_{l,m} = \int |F_{l,m}(R)|^2 R^2 dR$. The $D^{j}_{m,k}$ originate solely from rotations between the molecular and lab frames. From the CG coefficients we see the values of j and k are determined by l and λ, both of which are, in turn, determined by the symmetry of the valence electron orbital. The structure of $S(\theta,\chi)$ should therefore reflect the symmetry of the valance orbital from which the electron is ionized. The relative strengths of the $C_{j,k}$ are determined by the square of the radial wave function, which in the tunneling approximation represents the tunneling rate from a particular orbital. Also, since only the square of the l^{th} basis function appears in the expression the yield measurement contains no information about the relative phase between l and l' components, or partial waves.

Now that we have a general idea of the meaning of $S(\theta,\chi)$, we must develop a measurement from which we can extract the $C_{j,k}$. We find that measuring the delay dependent ion yield from a rationally excited molecular gas facilitates this extraction.

5.2 Measuring the coefficients

In the experiment we use a nonresonant pump beam to excite a rotational wave packet in a molecular gas, and measure the ion yield with a time delayed probe pulse. To extract the $C_{j,k}$ we need to understand the connection between $S(\theta,\chi)$ and the measurement. $S(\theta,\chi)$ represents the probability that a molecule aligned at $\{\theta,\chi\}$ will be ionized. However, in the experiment the probe pulse ionizes a molecular gas in which the probability density of

finding a molecule aligned at $\{\theta, \chi\}$ for a time delay t is given by

$$\rho(\theta, \chi, t) = g_i \frac{e^{E_i/kT}}{Z} |\Psi_i(\theta, \chi, t)|^2 \tag{5.6}$$

where $i = \{J_0, \tau_0, M_0\}$ are quantum numbers of the thermally populated initial rotational

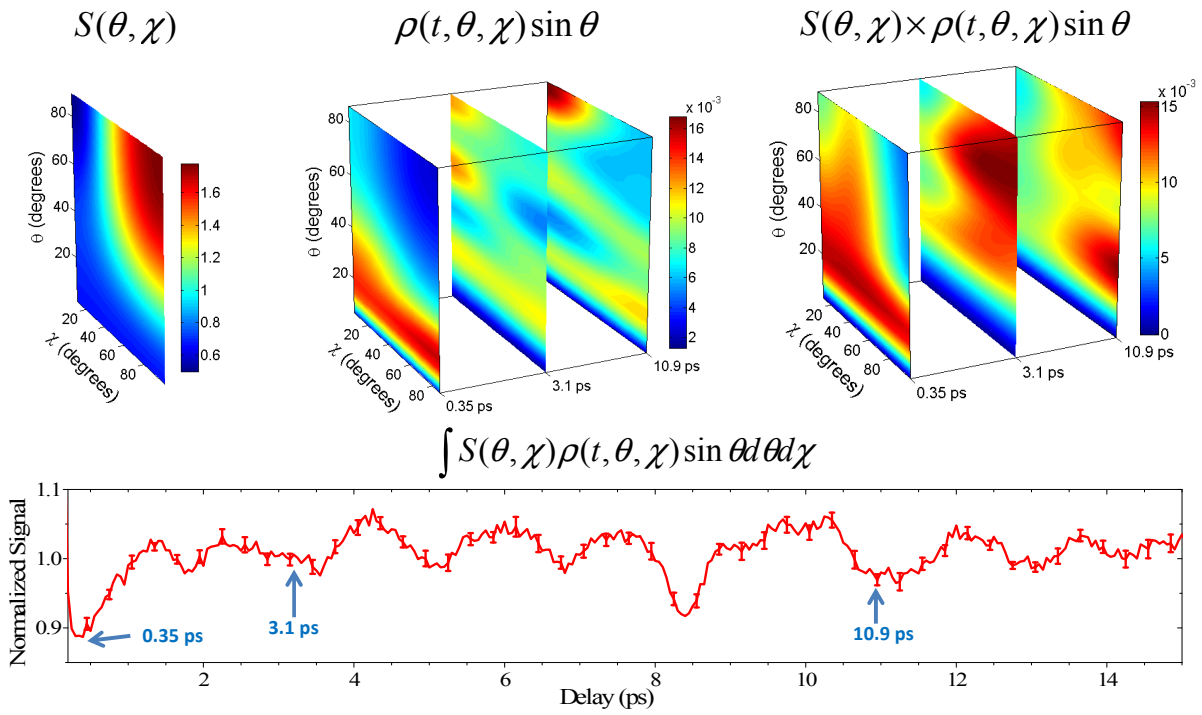

Figure 5.2: *A depiction of the angular averaging leading to the measured time dependent signal. The first column shows the molecular frame angle dependent yield for single, non-dissociative ionization of ethylene. The second shows the molecular axes distributions calculated from the rigid rotor TDSE at 9 K for three different time delays after a 120 fs, 4 TW/cm^2, linearly polarized laser pulse. The ion yield is extracted from experimental data with a 30 fs pulse with an estimated peak intensity of 80 TW/cm^2. The third column shows the product of the two at the three different times. The integral of the product over all angles for each time is shown below all three. The arrows indicate the delays that correspond to the figures in the row above.*

states with energy E_i, spin nuclear statistical weight g_i, and Z is the partition function. Therefore, in the experiment the probability density for producing a molecular ion aligned

at $\{\theta, \chi\}$ at delay t is given by $\rho(\theta, \chi, t)S(\theta, \chi)$. Integrating this over all angles gives the ion yield as a function of time delay,

$$S(t) = \int \rho(\theta, \chi, t)S(\theta, \chi) \sin\theta d\theta d\chi = \sum_{jk} C_{j,k} \int \rho(\theta, \chi, t) D^j_{0k} \sin\theta d\theta d\chi = \sum_{jk} C_{j,k} \left\langle D^j_{0k} \right\rangle (t). \tag{5.7}$$

Fig. 5.2 is a depiction of the averaging with the probability densities calculated using the TDSE as described in chapter 2 shown for three time delays. If $S(t)$ and the $\left\langle D^j_{0,k}(t) \right\rangle$ are known the above equation is linear in the $C_{j,k}$ and equivalent to the matrix equation $A \cdot \vec{x} = \vec{b}$, the column vector $\vec{b}$ representing the measured data. The $S(\theta, \chi)$ shown in the Fig. 5.2 is extracted by solving eq 5.7 for $C_{j,k}$ using the measured data for $S(t)$ and calculated $\left\langle D^j_{0,k}(t) \right\rangle$ for laser parameters estimated by fitting the data. The data therefore also provides the probability distribution of molecular axesl.

In the following section we detail the experimental setup used to measure the data shown in Fig. 5.2 as well as the numerical method used to solve Eq. 5.7. We also present additional data taken at different intensities for non-dissociative ionization, and measurements of fragment yields for dissociative ionization occurring at higher intensities.

5.2.1 Experimental Setup, Data and Analysis

The KLS beam is split into a pump and probe arm using a 60/40 beam splitter (BS). The probe beam is delayed using the same 2 ns delay stage as in previous chapters. The beams are recombined co-linearly on a 2 inch diameter 50/50 BS and focused into the VMI chamber with a 35 cm focusing lens. The pump beam is shrunk in diameter such that the probe diameter is 1.6 times that of the pump. Ethylene (C_2H_4) molecules, cooled by supersonic expansion from a high pressure jet (20% ethylene and balance helium at a total pressure of 70 bar) skimmed into the VMI spectrometer, are rotationally excited by a single non-ionizing pump pulse. The molecules are then ionized with a probe pulse that is delayed with respect to the pump pulse by up to 50 ps. The intensity of the probe pulse is initially

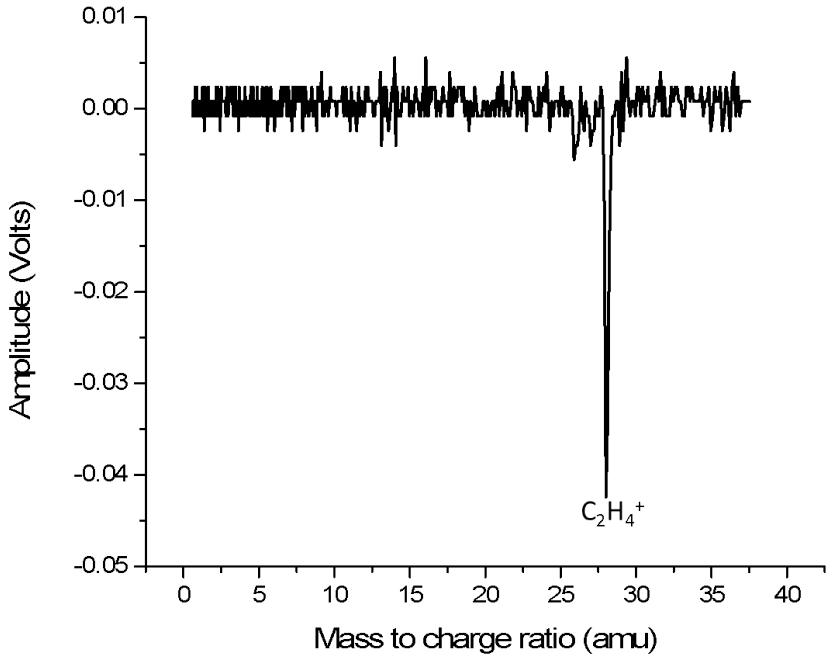

Figure 5.3: *A typical TOF spectrum for non-dissociative single ionization of C_2H_4, measured with a 175 TW/cm^2, 30 fs pulse. This is the highest intensity used for the non-dissociative measurement.*

kept low enough that negligible fragmentation or double ionization is observed in the time-of-flight (TOF) spectrum. A typical TOF spectrum is shown in Fig. 5.3, where the molecular ion peak is marked. No peaks at all are observed with just the pump beam.The VMI plate voltages are set by measuring a TOF at a higher intensity at which significant fragmentation is observed and tuning the voltages till fragments that differ in mass by 1 amu are clearly resolved. The resulting TOF spectrum is shown in Fig. 5.4.

For non-dissociative ionization the yield of $C_2H_4^+$ is recorded as a function of pump-probe delay by setting the gate of a boxcar integrator on the molecular ion peak in the time-of-flight spectrum. No momentum information is recorded in this experiment. By using an optical chopper and the acquisition scheme used previously for degenerate four wave mixing (cf. chapter 4 section 4.2), the ionization rate from unaligned ethylene and from background

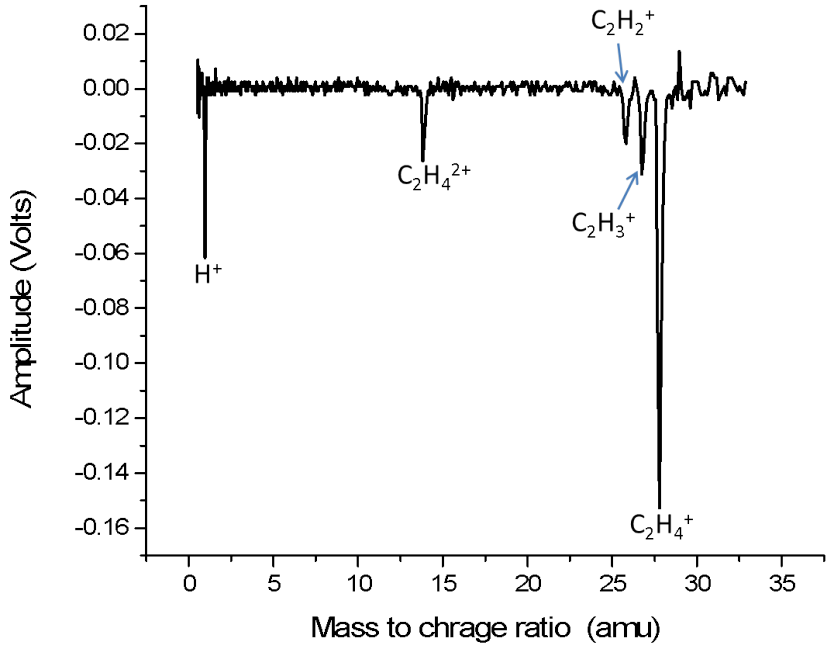

Figure 5.4: *A TOF spectrum for dissociative ionization of C_2H_4 at 250 TW/cm^2*

gas is recorded at the same time. The yield from the aligned molecules is then normalized to the yield from unaligned molecules after background has been subtracted from both. To reduce the effect of drifts in laser and jet conditions during the scan, multiple scans are performed and then averaged. Since the experimental error bars contribute to the reliability of the extracted $C_{j,k}$ (Eq. 5.10) this measurement technique proves to be an essential tool resulting in data with small standard deviation. The data are shown in Fig. 5.5 averaged over 20 scans with each point in a single scan averaged over 200 four-pulse cycles; the error bars show the statistical standard deviation.

From this data, we extract the coefficients $C_{j,k}$ as well as the molecular axis distribution seen by the probe pulse. First we can reduce the number of independent $C_{j,k}$ by considering the symmetry of the interaction. Fig 5.1 can serve as an aide when trying to form a mental image of these symmetries. As already stated, cylindrical symmetry about the laser

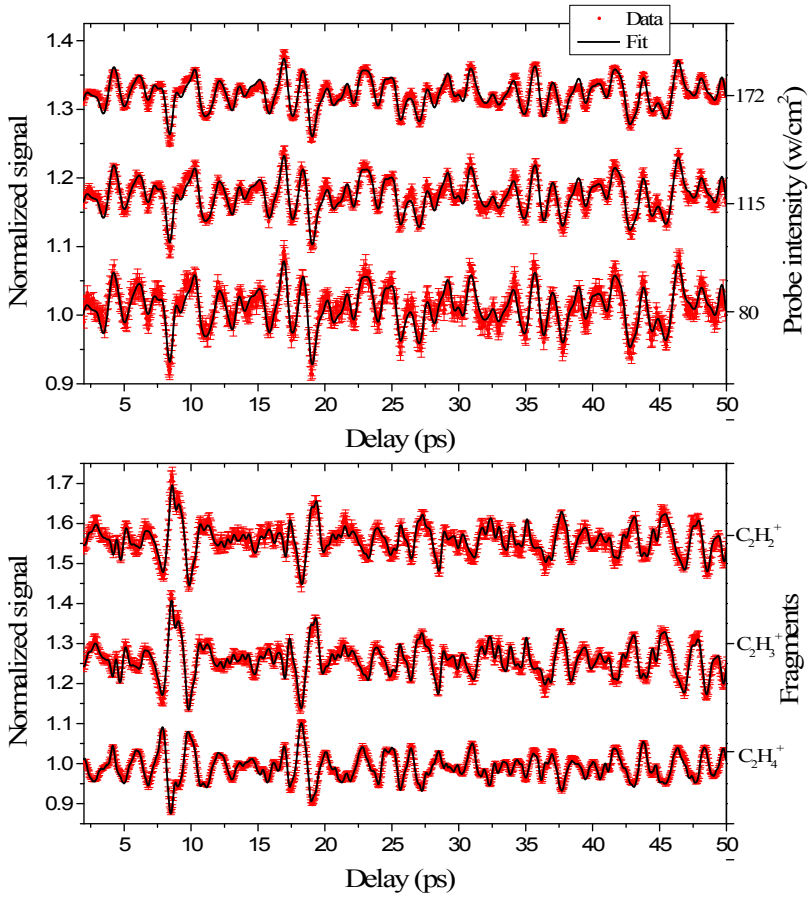

Figure 5.5: *Above - the normalized yield of $C_2H_4^+$ with three different probe intensities and the same pump intensity, below - the normalized yield for different fragments of C_2H_4 at a probe intensity of 250 TW/cm^2.*

polarization axis dictates that S be independent of ϕ, requiring that $m = 0$. Further, any two fold rotation about θ or χ must leave S unchanged. Applying these symmetries to $D^j_{m,k}(\theta, \chi, \phi)$ (see Zare[50] chapter 3) reduces the sum to be over only even j and k and requires that $k = -k$,

$$S(\theta, \chi) = \sum_{jk} C_{j,k}(D^j_{0k}(\theta, \phi, \chi) + D^j_{-k0}(\theta, \phi, \chi)). \tag{5.8}$$

Note that in order to extract the $C_{j,k}$ the corresponding $\langle D_{jk} \rangle$ — the average of the

$D^j_{k0}(\theta, \phi, \chi)$'s over the molecular axis distribution — must be non-zero. This is determined by the symmetry of the molecular axis distribution. In this particular case a linearly polarized laser pulse sets up a molecular axis distribution with just the right symmetry. Only moments with even j and k are non-zero and $\langle D_{j,k} \rangle = \langle D_{j,-k} \rangle$ allowing, in principle, the extraction of all non-zero $C_{j,k}$. Formally stated, the group of symmetry operations of the interaction Hamiltonian that determines the molecular axis distribution — the alignment Hamiltonian — is isomorphic to the group of symmetry operations of the measured signal $S(\theta, \chi)$. It is generally required that the alignment Hamiltonian be either isomorphic to, or contained in the symmetry group of $S(\theta, \chi)$ in order to be able to extract all the $C_{j,k}$. This can be decided by the nature of the aligning laser pulse. However, even if this condition is not satisfied, a symmetrized version of $S(\theta, \chi)$ can still be determined.

We use linear regression to solve Eq. 5.7 and determine the $C_{j,k}$ for a table of laser parameters and gas temperatures .Eq. 5.7 can be written as the matrix equation,

$$\vec{s} = D \cdot \vec{c} \tag{5.9}$$

where $\vec{s}$ is a vector containing the measured delay scan, D is a matrix of column vectors with each column containing a calculated $\left\langle D^j_{0k} \right\rangle$ as a function of delay and $\vec{c}$ is the unknown vector of coefficients $C_{j,k}$. Provided the columns of D are linearly independent the above equation has a unique solution which can be determined using linear regression. The details of the linear regression algorithm used can be found in *Numerical Recipes in C++*[54]. The elements of the matrix D and the vector $\vec{s}$ are divided by the experimental error at each time delay yielding D_e and $\vec{s}_e$. $\vec{c}$ is then obtained by solving the so called 'normal equation' which minimizes the error between the data and the model defined as $|\vec{s} - (D \cdot \vec{c})|^2$,

$$\vec{c} = \alpha^{-1} \cdot \vec{\beta} \tag{5.10}$$

where $\alpha = D_e^T \cdot D_e$ and $\vec{\beta} = D_e^T \cdot \vec{s}_e$. Additionally, the diagonal elements of α^{-1} provide

the variances of the fit parameters. $\vec{c}$ is found in this way for a 10×10 grid of intensities and pulse durations; and for each of these grid points the states are thermally averaged as needed to scan the temperature from 1 to 20 K in 1 K steps. For this purpose, we first solve the TDSE on a 10×10 laser intensity and pulse duration grid, and for 985 initial rotational states (these suffice to construct thermal distributions for any temperature below 50 K). The expectation values for all Wigner functions up to $j = 4$, $k = 4$ for each initial rotational state are calculated as a function of delay (up to 50 ps) and stored. For each pulse duration, intensity and temperature we determine the values of $C_{j,k}$ that minimizes the squared difference between the measured and computed signal by linear regression.

In Figure 5.5, the best fit curves for the $C_2H_4^+$ yield are shown superimposed on the data for three different probe laser intensities. The pump pulse parameters obtained independently from the three fits are identical – 4 TW/cm^2 and 120 fs – and compare well with measured values of 6 TW/cm^2 and 100 fs. The lower intensity for the best fit likely results from the lack of averaging over the volume of the interaction region in the calculation. The extracted temperature from the fitting procedure is 9 K, again the same for all three traces. A representation of the resulting error surface for the $C_2H_4^+$ yield at a probe intensity of 80 TW/cm^2 is shown in Fig. 5.6 and $\vec{c}$ for the corresponding minimum error solution is shown in Table 5.1 with standard deviations.

Fit coefficients	Extracted values
$C_{0,0}$	1.022± 0.0008
$C_{2,0}$	-0.434 ± 0.007
$C_{2,2}$	-1.564 ± 0.02
$C_{4,0}$	-0.334± 0.06
$C_{4,2}$	-0.359 ± 0.149
$C_{4,4}$	-0.197 ± 0.549

Table 5.1: *Extracted fit coefficients for $C_2H_4^+$ at 80 TW/cm^2.*

As is evident from Table 5.1 the uncertainty in $C_{4,4}$ is much larger than the extracted value of the coefficient precluding the reliable extraction of higher orders. Apart from experimental error bars, this is largely due to a fundamental limit applied by the filtering

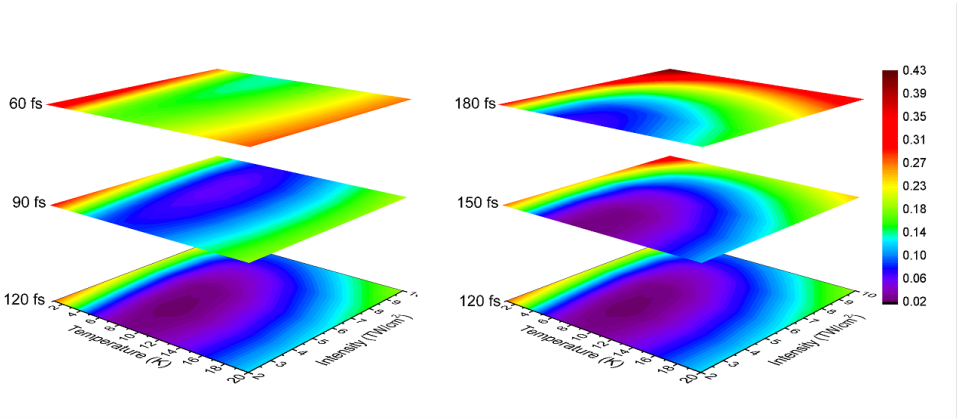

Figure 5.6: *A representation of the error surface for the fit to the $C_2H_4^+$ yield at 80 TW/cm^2. Contour maps of the surface for pulse durations on each side of the minimum error solution at 4 TW/cm^2, 120 fs and 9 K are shown.*

of S through the rotational wave packet, as suggested by Eq. 5.7. To better understand this we can examine the $\left\langle D^j_{0,k} \right\rangle (t)$, which can be written out using Eq. 2.21 and 2.22 in chapter 2 as a sum over the matrix elements $\langle JKM| D^j_{0,k} |J'K'M\rangle$ where $|JKM\rangle$ are basis states of the rotational packet. In terms of CG coefficients,

$$\left\langle JKM|D^j_{0,k}(\theta,\phi,\chi)|J'K'M\right\rangle = \sqrt{\frac{2J+1}{2J'+1}} \left\langle J,M;j,0|J',M\right\rangle \left\langle J,K;j,k|J',K'\right\rangle . \qquad (5.11)$$

This determines rotational selection rules for $S(\theta,\chi)$ – $\Delta J = 0,1,2...,j$, $\Delta K = k$ and $\Delta M = 0$ where the highest value of j is determined by the complexity of $S(\theta,\chi)$. The model described earlier suggests that this depends on the angular structure of the valence orbitals. However, if the rotational wave packet contains no states with $\Delta J > 4$, the corresponding matrix elements cannot be accessed and their contributions will not be observed. Even if the wave packet is broad enough such that there are several pairs of states with $\Delta J = 4$ or greater, beats generated by each pair will interfere in the resulting signal. Further, beats from states separated by the same ΔJ but excited out of different thermally populated states will be averaged over incoherently. The combination of these factors determines to what extent S will be filtered and consequently the highest order $C_{j,k}$ that can

be extracted from the measurement. The consequence of this is a loss in angular resolution in the extracted $S(\theta, \chi)$ preventing the measurement of fine angular structure. However, as will be explained in the next section the extracted coarse grained functions help illuminate some of the essential physics of the process in question.

We can also increase the intensity of the probe pulse till fragment peaks are observed in the time-of-flight mass spectrum, as shown in Fig. 5.4. We then measure delay dependent yields for each fragment from the rotationally excited molecules by moving the gate of the boxcar integrator from one peak to the next. Time dependent yields for $C_2H_4^+$, $C_2H_3^+$ and $C_2H_2^+$ are shown in Fig. 5.5 with the fits superimposed. Though the delay scans for the ion and the fragments are considerably different, the pump parameters extracted independently from each fit are identical – 16 TW/cm^2, 90 fs – and compare well with the independently measured parameters of 17 TW/cm^2 and 106 fs. We would like to note here that in cases where averaging of the spatial intensity distribution of the pump beam plays a significant role, the best fit laser parameters may not coincide with those measured in the lab. We try to minimize the effect of intensity averaging in this experiment by expanding the probe beam and shrinking the pump beam so that the probe diameter is increased to a factor of 2.5 larger than the pump before focusing. Additionally, the 35 cm focusing lens is replaced by a 25 cm focusing mirror to provide additional intensity needed to fragment the molecules. This results in the significantly higher pump intensity quoted above; however still no TOF peaks are observed from the pump. Finally, the extracted temperature from fitting each of these traces independently is 9 K, identical to that extracted in the non-dissociative measurement.

5.3 Results and Discussion

The 2D angle dependent ionization yield extracted from the 115 TW/cm^2 probe pulse scan from Fig. 5.5 is shown in Fig. 5.7. To the best of our knowledge this is the first measurement

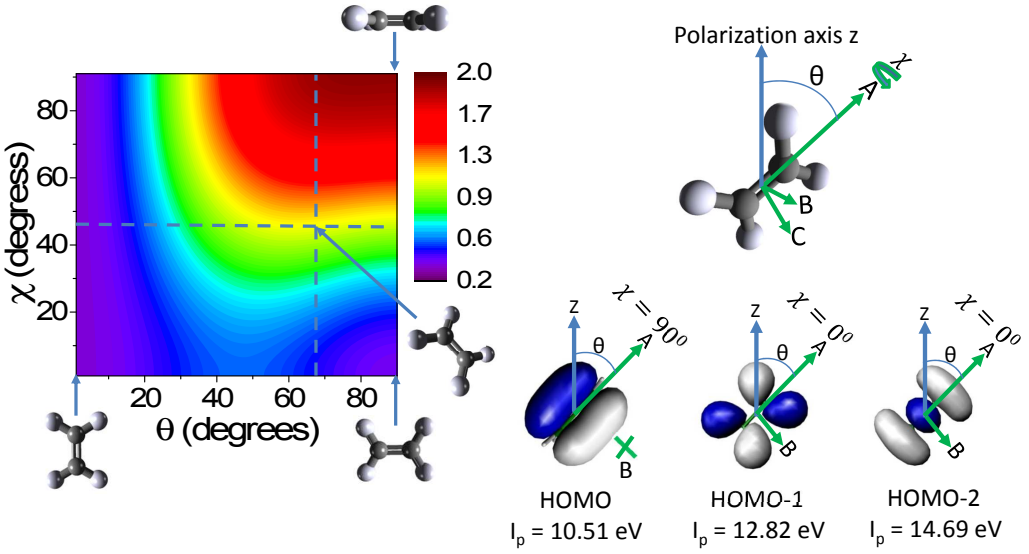

Figure 5.7: *To the left, the experimentally determined molecular frame angle dependent $C_2H_4^+$ yield. The ball and stick figures surrounding the data depict the orientation of the molecule at several points. To the right, the density profiles of the three highest occupied molecular orbitals of ethylene and a drawing of the coordinates. θ is the angle between the laser polarization and χ is the angle between the plane in which C=C axis and the laser polarization lie and the molecular plane.*

of the 2D angular dependence of non-dissociative ionization and illustrates the power of the technique. The density profiles of the two highest occupied molecular orbitals calculated by A.T. Le using the Gaussian quantum chemistry package are shown beside the angular dependence. The ion yield has a maximum at θ and $\chi = 90°$, consistent with the density profile of the highest occupied molecular orbital (HOMO). At $\chi = 0°$, where the laser polarization is in the nodal plane of the HOMO, we see a modulation with peaks near 45°, consistent with the density profile of HOMO-1. Removal of a HOMO electron puts the ion in the ground $\tilde{X}\ ^2B_{3u}$ and removal of a HOMO-1 electron puts it in the excited $\tilde{A}\ ^2B_{3g}$ state. We refer the interested reader to appendix D for a discussion on symmetry labeling of molecular states and the electronic configuration of the ethylene cation. a) and b) in Fig. 5.8 show the retrieved 2D yields for all three probe pulse intensities as well as calculations—in the strong field approximation—of the ionization rates from HOMO, HOMO-1 and HOMO-

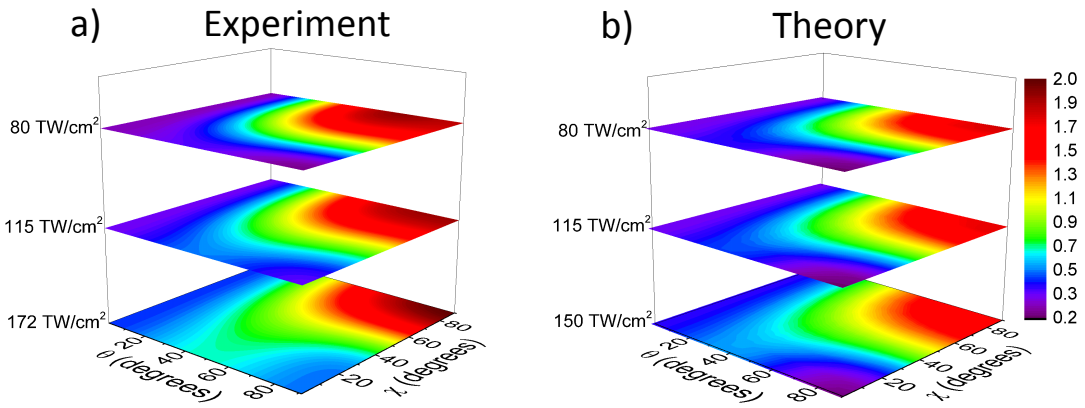

u

Figure 5.8: *a) Experimentally determined and b) theoretically calculated molecular frame, angle dependent $C_2H_4^+$ yields.Calculations performed by A.T. Le*

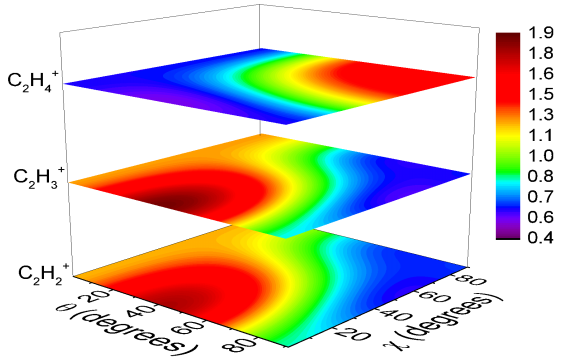

Figure 5.9: *Experimentally determined molecular frame, angle dependent yields for fragments of ethylene.*

2. As the intensity is increased the strength of the modulation at $\chi = 0°$ gets amplified, indicating that the contribution from HOMO-1 relative to that from HOMO increases with probe intensity and is responsible for the variation of the angle dependence. It was also necessary to include HOMO-2 in the calculations to account for the non-zero yield at the nodes of the HOMO and HOMO-1 orbitals[11], though its contribution is not large.

Shown in Fig. 5.9 are the angle dependent yields for $C_2H_4^+$, $C_2H_3^+$ and $C_2H_2^+$. These

data were taken at an intensity of about 250 TW/cm^2 where no charged carbon fragments are detected.In photoelectron spectroscopy, the appearance threshold for these fragments is correlated with the excitation of the $\tilde{A}\ ^2B_{3g}$ and $\tilde{B}\ ^2A_g$ state of the molecular ion[97,98]. In an intense field we observe that the fragmentation process preferentially selects molecules aligned near $\theta = 45°$, $\chi = 0°$. The yield is also somewhat enhanced when the C=C bond is aligned with the laser polarization for any value of χ. The former is consistent with ionization into the $\tilde{A}\ ^2B_{3g}$, and the latter with ionization into the $\tilde{B}\ ^2A_g$ state. The molecular ion yield is markedly weaker near alignment angles where the fragment yields are enhanced, however molecules aligned perpendicular to the laser polarization are preferentially ionized into the $\tilde{X}\ ^2B_{3u}$ state and remain bound. Furthermore at intensities below $\sim$ 180 TW/cm^2 the ion yield exhibits evidence of ionization into the $\tilde{A}\ ^2B_{3g}$ state (cf. Fig. 5.8), thus leaving stable ions in the excited state. This may be explained by the fact that the removal of H/H_2 requires 0.68/0.75 eV additional energy over the ionization threshold of the $\tilde{A}\ ^2B_{3g}$ and depends on the vibrational modes excited in the ionic state[99,97,98,100]. Higher intensity data in which the C=C bond is broken are pending analysis and are not presented here. However we expect that these will exhibit features related to fragmentation in the di-cation[101] and features related to field excited states[102,101].

5.4 Summary and conclusion

In this chapter we developed and demonstrated a technique to measure the alignment angle dependence of light induced processes in asymmetric top molecules. Unlike 3D alignment experiments such as the one presented in chapter 3 this technique allows the process to be resolved as a function of both Euler angles θ and χ. Also, unlike coincidence measurements this technique does not require that the molecule fragment in order to measure the direction of the molecular axes. As a demonstration of the technique we presented the first fully angle resolved alignment dependent measurement of strong field, single ionization of

an asymmetric top – ethylene, which does not fragment as a result of ionization. At higher intensities where the molecule does fragment we made analogous measurements of the fragment yields. The measurements allowed for the identification of ionic states involved in the processes. Though the angle dependent yields contain a wealth of information about the ionization and fragmentation processes, Eq. 5.5 indicates that the relative phase between partial waves is washed out. This occurs primarily due to integration over the emission angles of the electron. Measuring the emission angles of the electron or fragment in the lab frame using our VMI spectrometer can to some extent mitigate this averaging. In the next chapter we attempt to untangle the information contained in delay dependent VMI images measured from a rotational wave packet, and explore the possibility of extracting the alignment dependent phase of the ionization dipole.

Chapter 6

Works in Progress : Preliminary and Collaborative work

6.1 Introduction

In this chapter we discuss possible applications of the method developed in the previous chapter. In chapter 1, Fig. 1.4 we show data collected by Williams *et al.*[5]. The figure shows measured angular distributions of photoelectrons emitted from the K-shell of methane for different molecular orientations. Can we produce a similar figure for the ionization of a valence orbital in a strong field? While the necessary analysis and data collection is still in progress, we describe the collection of preliminary experimental data and its analysis. We measure delay dependent photoelectron spectra from a rotational wave packet in ethylene. From the data we extract alignment angle dependent yields at different photoelectrons energies using the method described in the previous chapter. We also describe the additional analysis required to generate the alignment dependent angular distributions resolved in the polar emission angle, and further experimental efforts needed to resolve both emission angles. While chapter 1, Fig. 1.4 shows measured ionization cross sections, we discuss the possibility of using our rotational wave packet technique to extract the complex ionization amplitude.

We also discuss the possibility of alignment-angle-resolved measurements of high harmonic generation (HHG) from ethylene using the rotational wave packet method. Data collected in collaboration with Carlos Trallero's group towards this goal is shown and the necessary steps towards completing the measurement are discussed. In another collaboration with the group of Martin Centurion at the University of Nebraska the possibility of reconstructing the 3D structure by electron diffraction from a 1D aligned asymmetric top molecule was demonstrated[103]. Our role in this collaborative effort is discussed. Finally, a collaborative experiment with the group of Artem Rudenko to measure the evolution of an electronic wave packet in the carbon dioxide ion is discussed. The experiment was performed using the pump-probe setup used for the experiments described in the previous chapter.

6.2 The Measurement of Photoelectron Spectra

6.2.1 VMI Spectrometer Upgrade

We used velocity map imaging (VMI) to measure the spectra of photoelectrons from ethylene. The VMI spectrometer described in chapter 2 was upgraded to a thick lens VMI spectrometer described in Kling *et al.*[104]. The initial design was provided by Nora Kling, and modified using SIMION by Aram Vajdi to ensure that the distance between the interaction region and the focusing plane conformed to the chamber dimensions [i]. Fig 6.1 shows a 3D rendering of the design provided by Al Rankin. The primary advantage of this spectrometer is that it provides high energy resolution over a wide energy range. This is achieved by replacing the extractor plate with a stack of plates over which the voltage is sequentially dropped by hard-wired 100 MΩ resistors. The entire spectrometer is surrounded by a μ-metal (highly permeable alloy) cylinder intended to shield electrons from stray magnetic fields and the field-free flight region is covered by an aluminum cylinder to shield stray electric fields. The 40 mm detector of the previous setup is replaced by a 80 mm diameter

[i] Technical details of the design will be provided in Aram Vajdi's thesis.

detector assembly purchased from Photonis consisting of three MCP detectors stacked together (a Z-stack) and coupled to a phosphor screen. The focusing voltages used are 2 kV for the repeller and 1.8 kV for the extractor, and 2.1 kV is applied across the MCP plates with 3.6 kV on the phosphor screen.

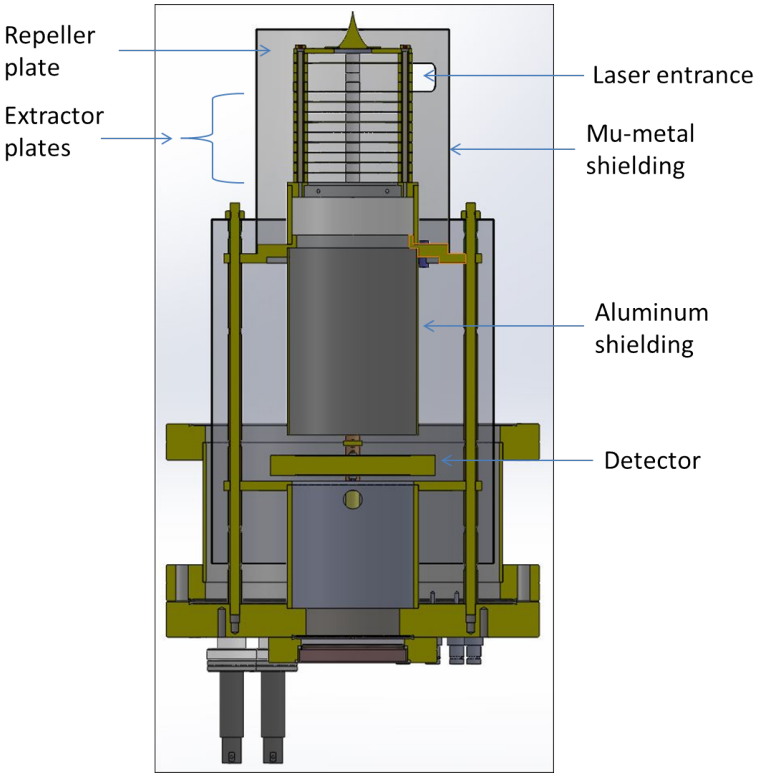

Figure 6.1: *The upgraded thick lens VMI spectrometer used for photoelectron measurements.*

The CMOS camera is replaced by a TEC (thermo-electric cooler) cooled EMCCD [ii] camera (Andor Luca S) with a 658×496 pixel chip, 10×10μm pixel area and substantially lower background noise levels than the CMOS chip. The hit counting and single-shot operation of the previous setup is replaced by averaging over multiple images, each collected with a 50 ms exposure.

[ii] *electron-multiplying charged coupled device*, a technology invented by Andor

6.2.2 Photoelectron Spectra for Ethylene

Fig. 6.2 shows a raw VMI image for photoelectrons from ethylene ionized by a 65 TW/cm^2, 30 fs linearly polarized laser pulse. The clearly visible periodic outer rings are a manifestation of above threshold ionization(ATI)[30]–the ionization of an electron with more than the minimum number of electrons required for ionization. The ionization potential (I_p) for the valence electron of ethylene is 10.51 eV[105], requiring at least seven photons (1.56 eV each) for ionization. Each ring represents the absorption of an additional photons above this threshold. While it is understood that a free electron cannot absorb a photon since momentum conservation is violated, the ionized electron in this case is still in the field of ion which recoils with each additional absorption thus conserving momentum[30,106]. This effect is unique to ionization in strong fields and is emphatically non-perturbative as evidenced by measurements that show that later ATI peaks can be significantly stronger than earlier ones[107]. An electron having absorbed n photons to reach the ionization threshold then gets driven by the laser. The average quiver energy (U_p) adds to the binding potential leaving the electron trapped in the ionic potential, effectively still bound. The electron then needs to absorb an additional s photons to escape the binding potential. Effectively, this can be thought of as a shift in the I_p by $U_p = eE_0^2/4m\omega^2$, e and m being the charge and mass of the electron, E_0 and ω the peak field strength and angular frequency of the laser pulse. This is the ponderomotive energy and can also be given by the practical expression $U_p = 9.33 \times 10^{-14} I_0 \lambda^2$, I_0 being the peak pulse intensity in W/cm^2 and λ the laser wavelength in microns giving U_p in eV. Given this information the kinetic energy of the ionized electron is given by,

$$E_{kin} = (n + s)\hbar\omega - (I_p + U_p) \tag{6.1}$$

As is evident from Eq. 6.1 and the origin of ATI the rings ought be spaced by the energy of a single photon, providing a reference for the calibration of the spectrum. However, Fig 6.2 is

Below the first ATI peak the structure is significantly more complicated. As the electron absorbs photons on its way to the continuum, it can hit an excited state that is brought into n-photon resonance with the ground state after being Stark shifted by the field. These are referred to as Freeman resonances and are known to be responsible for the intricate low energy structure of the spectrum[108,106,109].

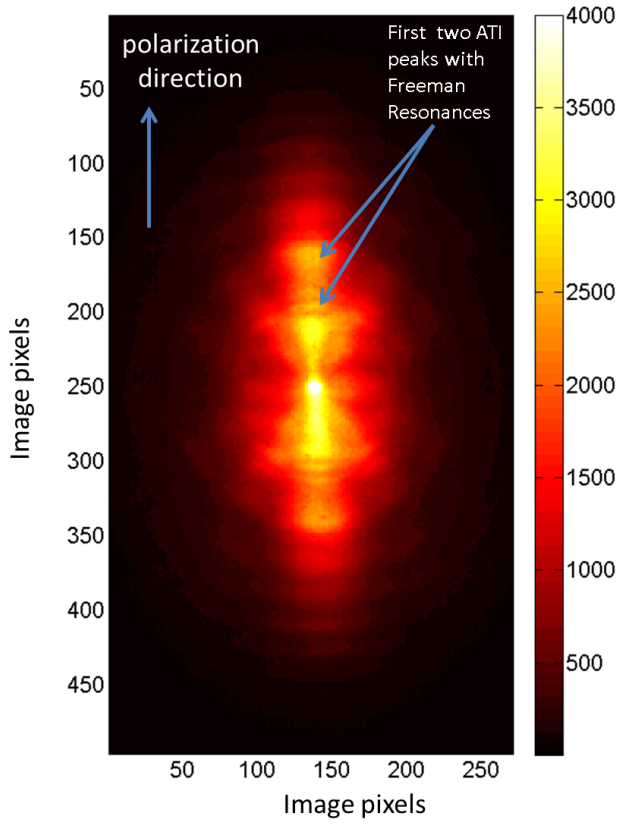

Figure 6.2: *VMI image of photoelectrons from ethylene in a 65 TWcm^2, 30 fs laser pulse. ATI peaks and Freeman resonances are observed.*

not an energy spectrum but a 2D projection of the momentum distribution. Before any real information can be gleaned from this image it must be transformed into the 3D momentum distribution. If a distribution is cylindrically symmetric an inverse Abel Transformation of a single 2D projection, such as the VMI image in the figure, gives the corresponding 3D distribution[110]. Details about the Abel transformation and the algorithm used to perform are provided in appendix E. We use the pbasex algorithm[110] in which the 3D distribution is written as a weighted sum of products of Legendre Polynomials and radial Gaussian

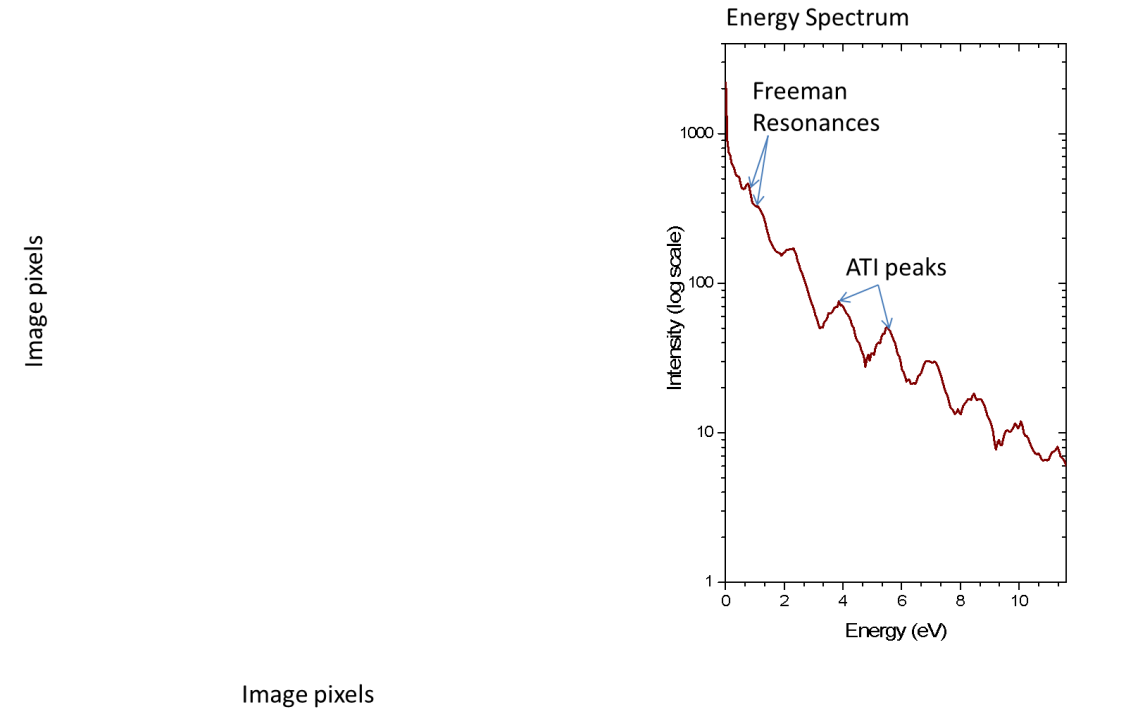

Figure 6.3: *An Abel inversion of the image in Fig. 6.2 giving the central slice of the 3D momentum distribution. Integration of the emission angle gives the energy spectrum on the right with ATI peaks and Freeman resonances marked.*

functions, with unknown weight coefficients. Projecting the sum onto a plane requires only projecting the basis functions and leaves the weight coefficients unaffected. Using linear regression the weight coefficients that best reproduce the data are then found and used to reconstruct the 3D distribution. Fig 6.3 shows the central slice of the reconstructed 3D distribution, with the X and Y axes representing the X and Y projections of the momentum. Shown alongside is an integral over the emission angle with the energy axis calibrated such that the spacing between the ATI peaks is 1.56 eV and using the fact the energy is proportional to the radius squared. The correct Jacobian factors for the angular integration and conversion to energy are also provided in appendix E. Given that $U_p = 3.96$ eV for the ionizing pulse Eq. 6.1 suggests that the first ATI peak should appear at 1.1 eV, though it appears at 0.74 eV requiring $U_p = 4.36$ eV. This difference suggests an

intensity measurement error of 9 %, par for the course for intense field experiments.

6.3 ATI from a Rotational Wave Packet

Figure 6.4 shows photoelectron spectra measured from a rotational wave packet in ethylene excited by a 10 TW/cm^2, 100 fs pump pulse as a function of pump-probe delay. The optical setup is the same as that used in the previous chapter for non-dissociative ionization, with the chopper removed and a 25 cm focal length concave mirror used instead of the focusing lens. The VMI images were collected over 40 scans, with 10 images collected per point for a single scan at an exposure of 50 ms. The images were averaged over the all scans for each delay point resulting in a single image for each delay averaged over 400 images, the same as the image in Fig. 6.2. This mode of data collection allows for averaging over the long term drift in laser intensity and number density of the gas pulse. The images were Abel inverted and converted to energy spectra as described above.

Shown alongside are delay dependent yields for three individual channels normalized to the isotropic values with fits calculated using exactly the same method as in the previous chapter superimposed. As is evident the fits do not faithfully reproduce the data. Additionally, the fourth coefficient C_{44} which gave the largest uncertainty for the ion yield measurements in the previous had to be removed. The primary reason for this is that the finer structure in the measurement appears to be on the level of the noise, therefore the fitting algorithm artificially inflates higher order coefficients attempting to fit the noise. The nature of the analysis does not allow for a simple error estimate in the data, thus precluding an uncertainty estimate for the coefficients.

The resultant angle dependent yield for the 13-photon peak is shown in Fig. 6.5 with isosurfaces for the three valence orbitals shown alongside. Other channels are not shown as the coarse structure is much the same and given the quality of the fits we are not in a position to comment on finer details. Tentatively, as in the case of ion yield measurements, the

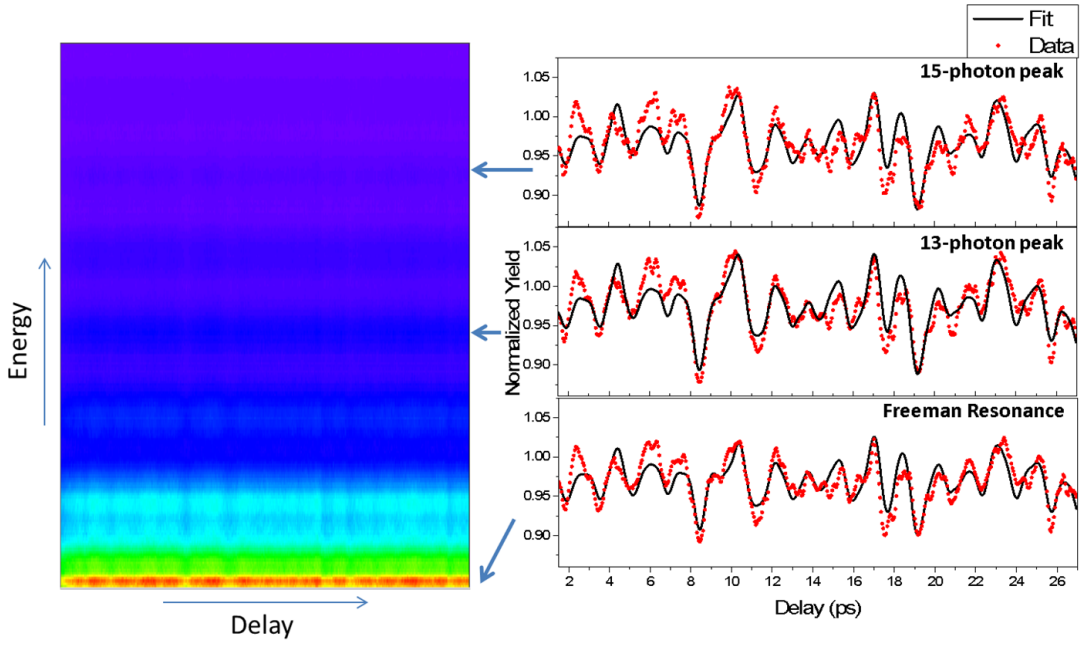

Figure 6.4: *Delay dependent photoelectron energy spectra for rotationally pumped ethylene with the traces integrated over specific peaks shown alongside.*

contributions of the orbitals may be inferred by comparing their shapes to the data, however calculations are required to confirm the interpretaion. As concluded in the previous chapter, all three orbitals appear to be involved in non-dissociative strong field ionization of ethylene. However while the contribution of the HOMO-2 orbital in the yields was not apparent without comparison with SFA calculations, the enhancement at $\theta = 0°$ indicating a HOMO-2 contribution appears to be much stronger here. Additionally, orbital nodes are sharply visible as the signal drops nearly to zero in the nodal positions. While these results are promising significant improvement needs to be made to the data quality such that differences in the alignment dependences for different ATI channels can be observed. Specifically, since the Freeman resonance peaks come from electrons that encounter a resonant excited state on the way to the continuum, the signature of this excited state should be identifiable in the angle dependent data.

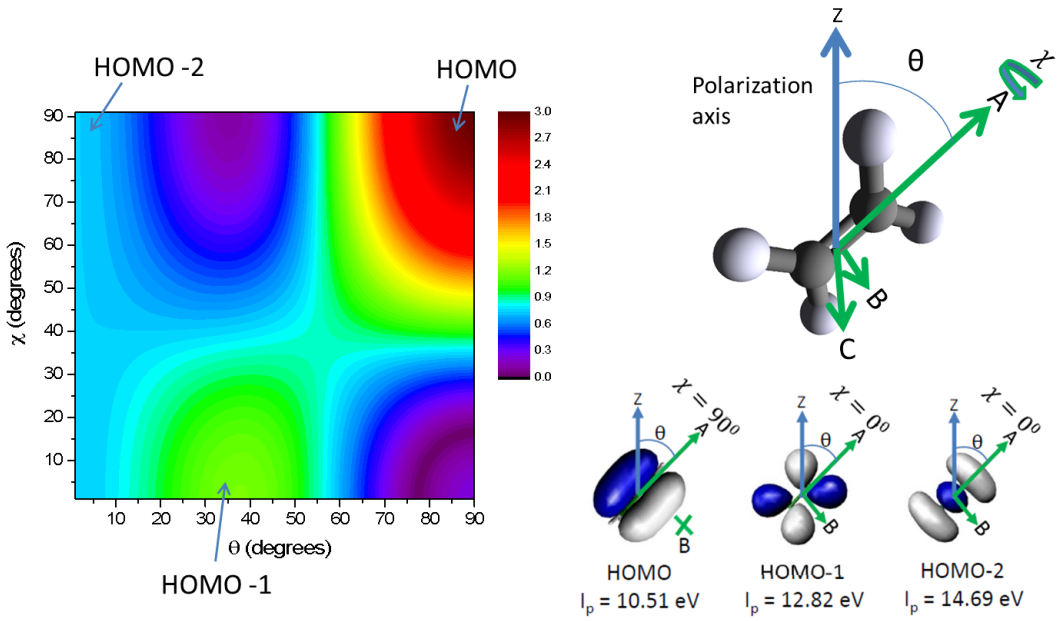

Figure 6.5: *Alignment dependent yield for the 13-photon ATI peak with the individual orbital contributions marked and the orbitals and coordinate system shown alongside.*

6.3.1 A Rotational Wave Packet as an Interferometer

Since we were interested in extracting alignment angle dependent yields for each n-photon channel we integrated the momentum distributions over the emission angle of the electron. However, we need not perform this integration which in principal presents the possibility of extracting the photoelectron angular distribution (PAD) for every molecular orientation. To do this we have to consider the relative phase between electrons emitted in the same direction from molecules aligned at different angles. Since the molecules are part of a coherent wave packet, the electron wave functions ionized from molecules at different alignment angles will interfere. The measured momentum distribution is the resulting interference pattern. In other words the complex n-photon ionization amplitude (rather than its square as in the yield case) must be averaged over the molecular axis distribution[44,111]. This represents a phase retrieval problem similar to that solved in the frequency resolved optical gating (FROG) pulse measurement technique[112]. The delay dependent n-photon ionization amplitude can

be written as,

$$\tilde{S}_n(t,\theta_k) = \int \rho(\mathbf{\Omega},t)\tilde{A}_n(\mathbf{\Omega},\theta_k)d\mathbf{\Omega} \tag{6.2}$$

where $\mathbf{\Omega}$ represents the Euler angles, t the time delay, $\rho(\mathbf{\Omega})$ the molecular axes distribution and θ_k is the polar emission angles of the electron with respect to the laser polarization. Since the molecular axis distribution is cylindrically symmetric about the polarization axis the integration makes $\tilde{S}$ independent of the azimuthal emission angle ϕ_k (cf. discussion of symmetry conditions chapter 5,section 5.2), making it impossible to extract the full PAD. $\tilde{A}_n(\mathbf{\Omega},\theta_k)$ will necessarily inherit all the symmetries of the molecular axis distribution, which can be manipulated by changing the polarization of the pump pulse.

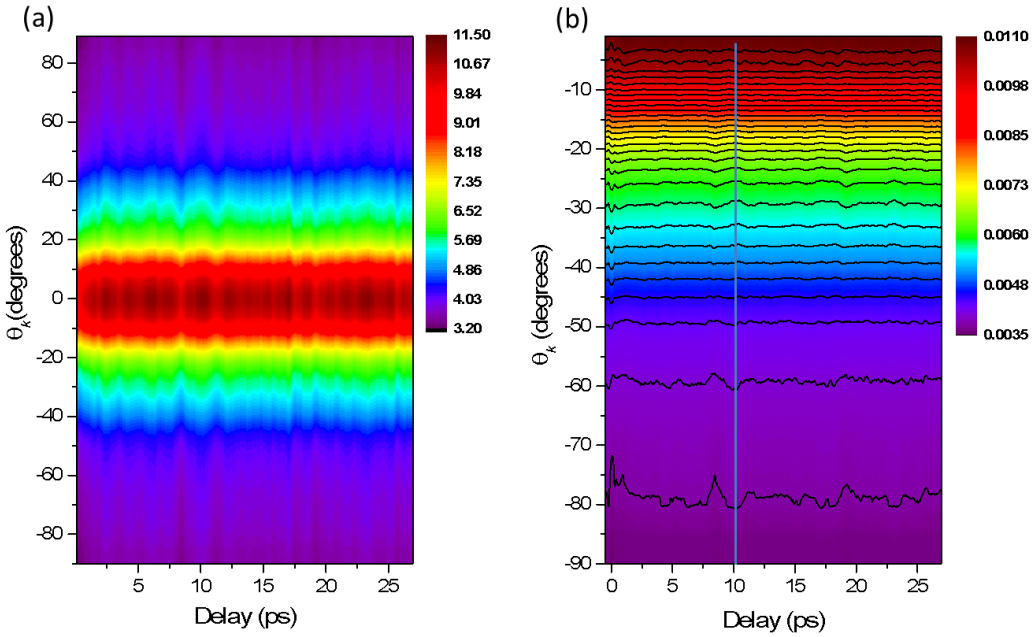

Figure 6.6: *Delay dependent PADs of the 13-photon peak for ATI from ethylene.*

The measured delay dependent PAD for the 13-photon peak is equal to $|\tilde{S}_{13}(t,\theta_k)|^2$, the square root of which is shown in Fig. 6.6(a). If the laser parameters can be determined from

the yield fits, $\rho(\mathbf{\Omega})$ can be calculated. Then, using a phase retrieval algorithm similar to that of Vozzi *et al.*[113] or numerous FROG algorithms[112] it should be possible to retrieve the function $\tilde{A}_n(\mathbf{\Omega}, \theta_k)$. Also, while the yield of the distribution in θ_k changes substantially as a function of delay, small changes in the angle (θ_k) dependent structure as a function of delay are also observable. In Fig. 6.6(b) the angular distribution at each delay is normalized to its integral, essentially removing the contribution of the changing yield. The figure is also plotted only for half the emission angles since it is symmetric about the laser polarization direction. The contour lines are intended as a guide for the eye to follow the changes in the angle dependent structure. These structural changes contain the desired phase information. Evidently electrons emitted closer to the polarization axis behave oppositely to those emitted further away. This behavior is most apparent during the first J-type revival, marked by the vertical line. We would like to note here that while the relative phase between electron partial waves of different angular momentum can be measure from a thermal ensemble and have been for single photon ionization[114], the alignment angle dependent phase can only be measured by ionization from a coherent wave packet.

6.4 Collaborative Work

Here we present brief descriptions of work performed in collaboration with other groups with an emphasis on our contribution to the work.

6.4.1 High Harmonic Generation

In this experiment performed in collaboration with Carlos Trallero's group we attempted to apply the technique developed in chapter 5 to measure the alignment angle dependent yield of high order harmonics generated from ethylene. The process of HHG is often described by the three step model[115]. A valence electron is first ionized by the laser field. When the field reverses direction the ionized electron is sent crashing back into the ion with which it

may recombine and emit a photon shedding the energy gained in the field. This processes repeats every half cycle of the laser field resulting in a periodic train of VUV pulses. In the frequency domain this corresponds to spectral teeth spaced by twice the photon energy. HHG is an intricate and complicated process, a detailed discussion of which is much beyond the scope of this thesis. We direct the interested reader to a recent thesis dedicated to the study of HHG from molecules[116].

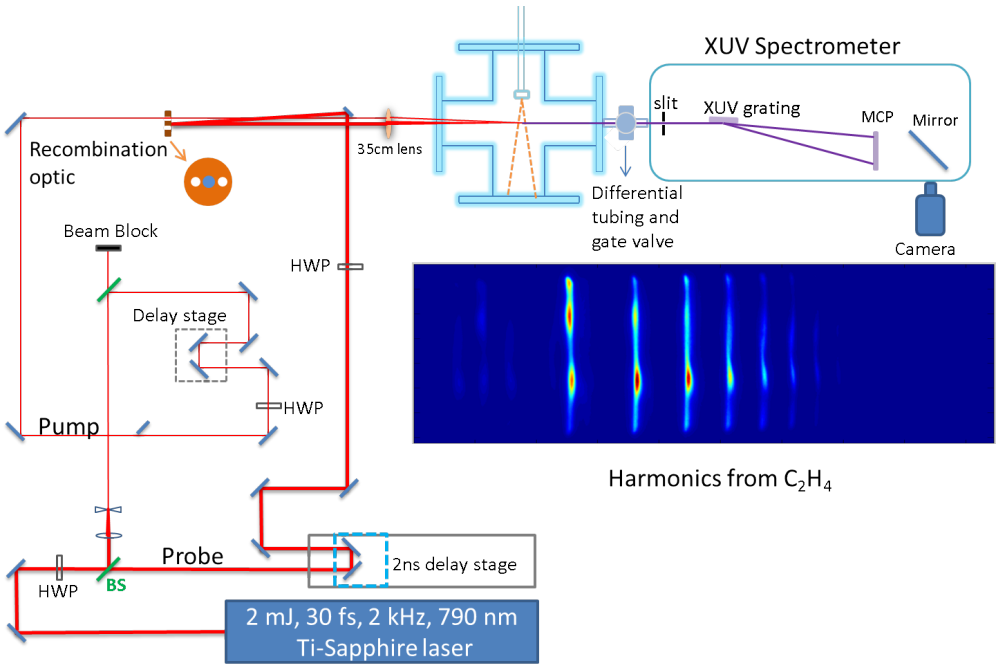

Figure 6.7: *The experimental setup for the HHG experiment.*

For the experiment a VUV spectrometer designed by Carlos Trallero was attached to the source chamber containing the gas jet and the laser was focused 1 mm from the nozzle where harmonics were generated. The experimental setup is shown in Fig. 6.7. The generated harmonics are sent into the spectrometer through a variable slit (1 mm for most experiments) onto a concave variable line density grating which disperses the harmonics such that they all focus in the same plane. An MCP detector with a phosphor screen behind it is placed in this plane and a CCD camera images the phosphor screen. A typical spectrum generated by averaging over 20 images each taken with the camera exposed for 0.6 s from ethylene is

shown alongside the experimental setup.

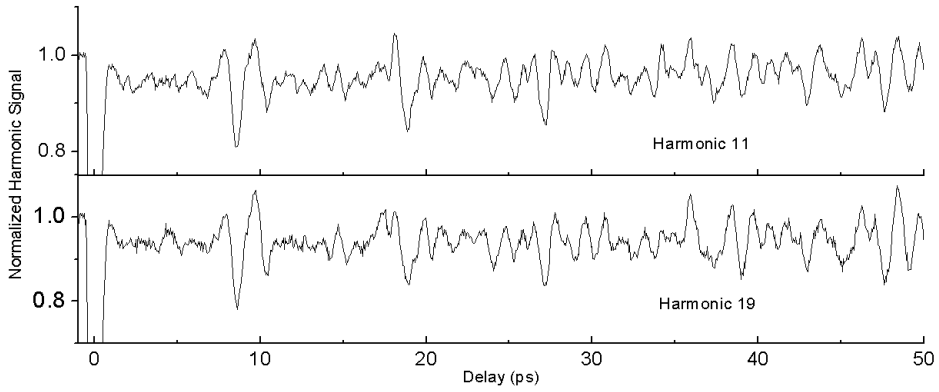

Figure 6.8: *The 11th and 13th harmonics as a function of delay generated from a rotational wavepacket in ethylene.*

Similar to previous experiments, the pump beam excited a rotational wave packet and a time delayed probe generated harmonics. Fig. 6.8 shows the delay dependent harmonic yield for harmonics 11 and 19. While small differences in the delay dependences of the harmonics are observable, attempts to fit these in a manner similar to the ion yield proved unsuccessful. We believe the reason for this is that, much like the photoelectrons, harmonics emitted from molecules aligned at different angles must be added coherently[117]. While this is also a 2D measurement (harmonic frequency and delay), attempts at phase retrieval were also unsuccessful. This is due to the fact that while photoelectrons emitted at different angles overlap generating an interference pattern harmonics at different frequencies do not, therefore no relative phase information is available from this measurement. This leads us to conclude that an independent phase measurement is required.

An interesting avenue presented by harmonic generation is the possibility of measuring dynamics occurring in the molecular ion during the electrons excursion in the field. Lower energy harmonics result from shorter excursions in the field and higher energy harmonics from longer excursions. This allows the frequency axis to be mapped to time after ionization

with a resolution of attoseconds[118]. While nuclear dynamics have been tracked using this method[118] access to electronic dynamics requires angular resolution, which the method developed in chapter 5 can provide. However, an independent measurement of the phase is required.

6.4.2 Diffractive Imaging of Molecules

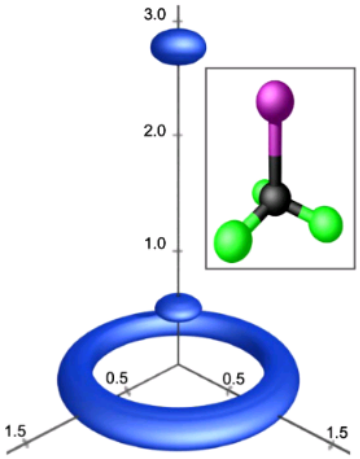

Figure 6.9: *The structure of CF_3I measured by Hensley* et al. *by gas phase diffraction of laser aligned molecules with the known structure in the inset.The black atom is carbon, purple iodine and green fluorine. The positions of the F atoms cannot be resolved.*

In a seminal experiment Martin Centurion's group at the University of Nebraska, Lincoln demonstrated that bond angles and bond lengths can be measured by diffracting electrons from 1D aligned molecules[119]. Though numerous molecular bond lengths were measures using gas phase electron diffraction prior to this experiment[120]; and elegant studies of dynamic changes in bond lengths were carried out[121,122,123], no previous measurements of bond angles using gas phase diffraction existed. The extracted structure of the CF_3I molecule extracted from their experiment is shown in Fig. 6.9 with the known structure shown in the inset. Note that while the I-C-F bond angle could be determined the positions of the fluorine atoms could not be determined as the in the experiment the molecule was free to rotate

about the C-I axis.

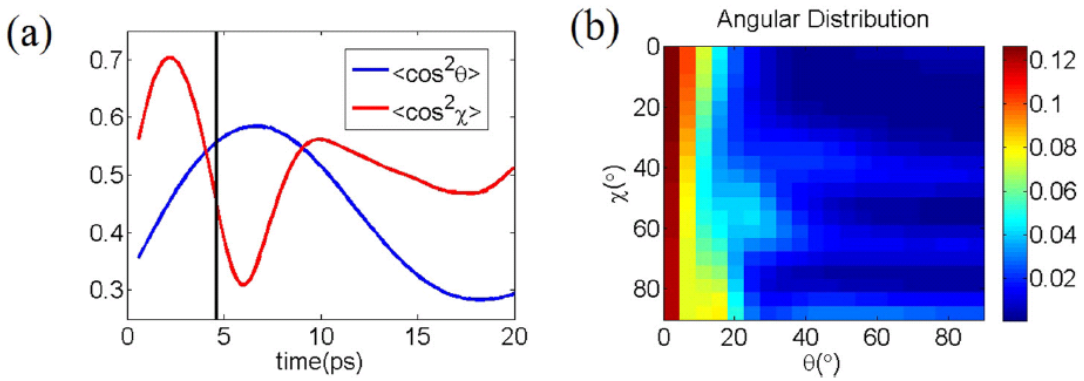

Figure 6.10: *Molecular axis distribution for and* $\langle cos^2\theta \rangle$ *and* $\langle cos^2\chi \rangle$ *for laser aligned* $C_6H_5CF_3$

We participated in a theoretical collaboration with the Nebraska group in which a scheme to measure the full 3D structure of an asymmetric top molecule was numerically demonstrated[103]. The molecule in question was trifluorotoluene, a prolate asymmetric top with a prolate type polarizability. Our part in the collaboration was the calculation of the molecular axis distribution as a function of time after a linearly polarized pump pulse. This was done using the theoretical methods detailed in chapter 2. Fig 6.10(a) shows the initial time evolution of $\langle \cos^2\theta \rangle$ and $\langle \cos^2\chi \rangle$ after a 50 fs, 15 TW/cm^2 aligning pulse. Fig 6.10(b) shows the molecular axis distribution 1.5 ps before the peak alignment as marked by the vertical line in (a). This time delay was chosen as the distribution is nearly isotropic in χ thus approximating 1D alignment, which is a requirement of the reconstruction algorithm developed by the Nebraska group.

The 'measured' diffraction pattern for electrons diffracting from this distribution of $C_6H_5CF_3$ was simulated using known scattering cross sections and phases[103]. A genetic algorithm developed in Martin Centurion's group was then used to retrieve the diffraction pattern for perfectly 1D aligned molecules. From this they were able to reconstruct the 3D structure of the molecule. Fig. 6.11 shows the result of this reconstruction with the known

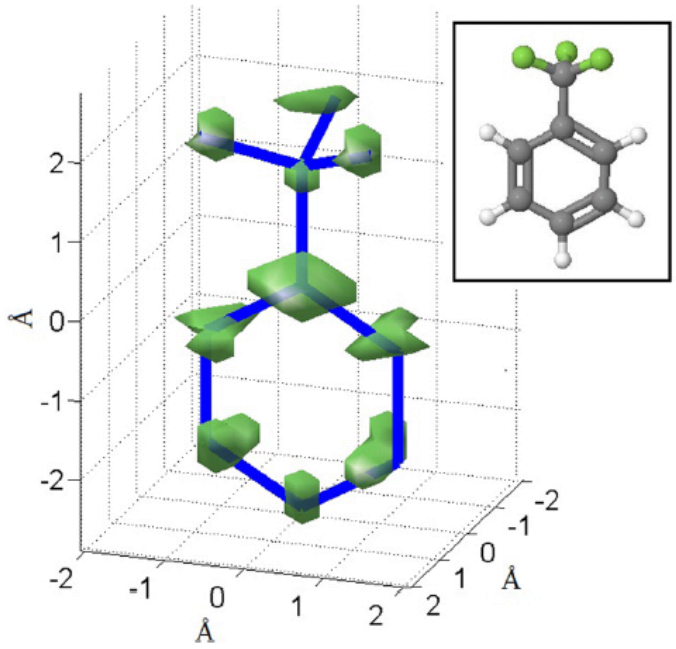

Figure 6.11: *The structure of trifluorotoluene from simulated gas phase electron diffraction with the known structure shown in the inset. Grey atoms are carbon, white are hydrogen and green are fluorine.*

molecular structure in the inset. The intension of the Nebraska group is to use this reconstruction technique on experimental samples when the molecular geometry is *unknown*, such as in evolving electronically excited states[124].

6.4.3 Electronic Wave Packets

This experiment strays from the central theme of this thesis to some extent, but is nonetheless related. It was carried out in collaboration with Artem Rudenko using the experimental setup used for the dissociative ionization yield measurements. However, no extra dispersion was added to the pump so as to keep both pulse durations near 30 fs and the diameters of both beams were also kept the same. The pump beam, with an estimated intensity of 73 TW/cm^2, intersected a gas of CO_2 molecules in the VMI chamber and a time of flight spectrum of the ions was measured. The intensity was controlled with an iris and set just

below the double ionization threshold by ensuring that no doubly charged ions were observed in the TOF spectrum. The time delayed probe with an estimated intensity of 84 TW/cm^2 produced doubly charged ions the normalized and background subtracted yield of which was measured as a function of the time delay.

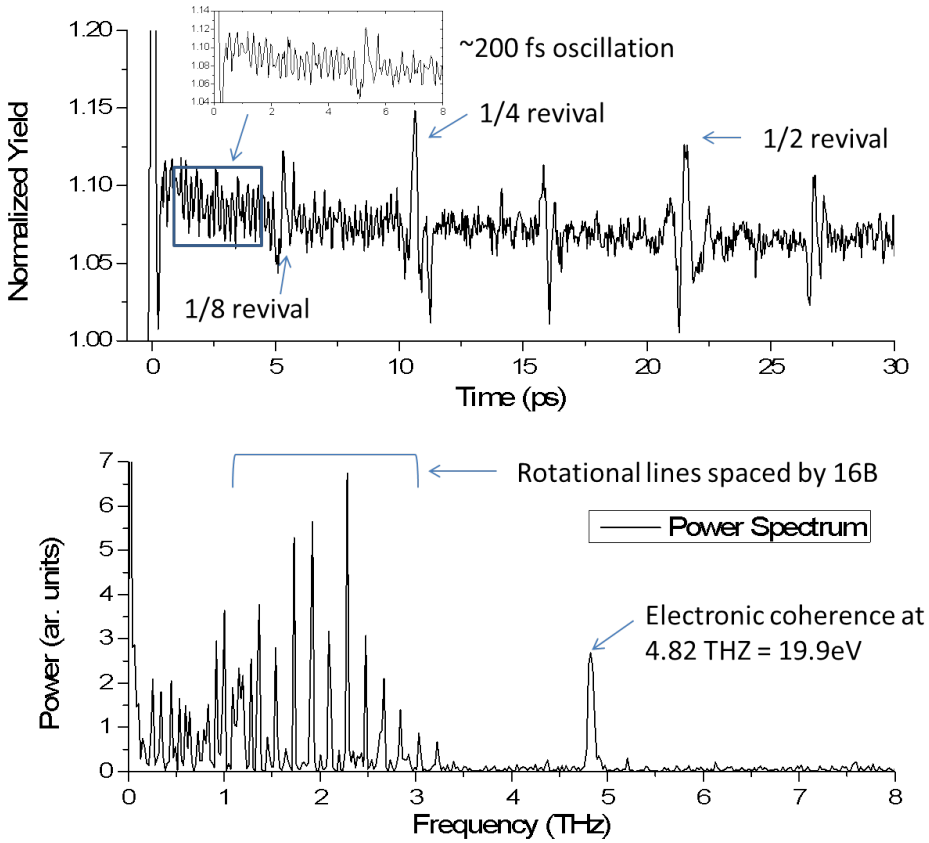

Figure 6.12: *Top– the delay dependent yield of CO_2^{2+} and Bottom– the power spectrum of the delay dependent yield, both showing electronic and rotational coherences originating in the singly charged ion or the neutral.*

Fig. 6.12 shows the yield over a 30 ps window measured with a 20 fs step, with the Fourier transform power spectrum shown below. The approximately 200 fs oscillations can be attributed to a wave packet of fine structure splitting in the ground electronic state of CO_2^+. From photoelectron spectroscopy the fine structure states are know to be split by 19.9 meV[125]. The power spectrum in Fig. 6.12 shows a peak at 19.9 meV(207 fs period and

4.82 THz frequency), in the vicinity of the fine structure splitting energy. The rotational revival structure of CO_2 is also present, with fractional revivals at $1/8^{th}$ of the rotational period clearly observable[126]. Corresponding rotational structure is observed in the power spectrum as lines spaced by $16B$[127], $B = 11.6$ MHz [iii]being the rotational constant of CO_2. Since the ground state geometries of the ion and neutral are essentially the same (symmetric 1.17 angstrom C=O bonds), it is difficult to determine whether the rotational wave packet is populated in the neutral or the ion.

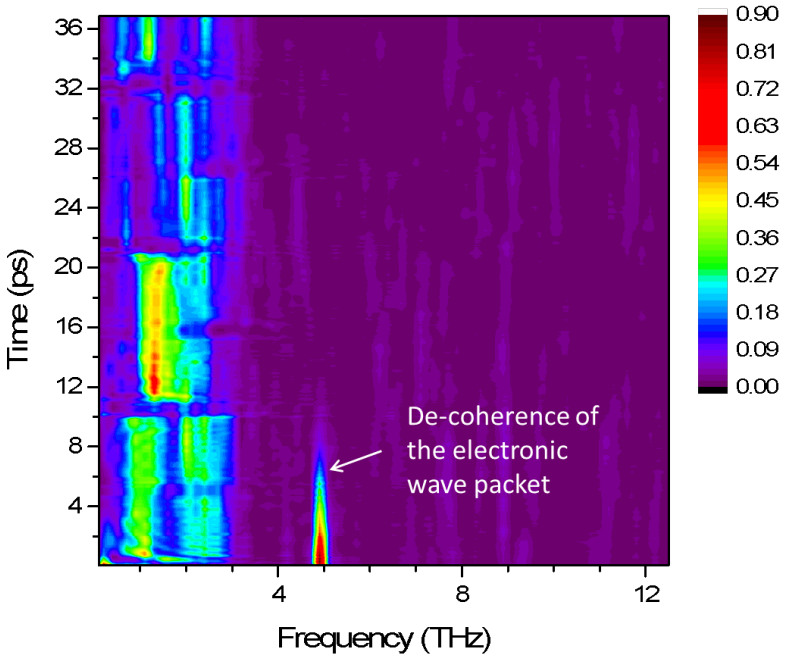

Figure 6.13: *A sliding window Fourier transform of the time dependent CO_2^{2+} yield showing the decay of the electronic coherence resulting from mixing with the rotational states.*

As evident from the delay dependent data the electronic coherence significantly deteriorates after the first rotational revival. To resolve this decay Fourier transforms are performed in sliding 2 ps windows over the entire range of delays. The sliding window Fourier trans-

[iii]B and bond lengths from the NIST computational chemistry comparison and benchmark database -CCCBDB

form is plotted in Fig. 6.13, where the Y axis is the initial delay point for each 2 ps window and the X axis is the frequency. By about 8.5 ps the electronic coherence is almost completely gone. The source of this decay is the rotational motion. Loosely, one can think of this as the electronic wave packet being 'shaken' by the rotational motion of the molecule. Recent HHG measurement from neutral nitric oxide showed a very similar fine structure coherence, which calculations showed decayed as a result of rotation[128]. In fact, since different harmonics differ in their relative sensitivity to rotational and electronic coherences, mixed electronic-rotational coherences were observable in the power spectrum of certain harmonics.

Numerous questions remain to be answered here. Why does strong field ionization coherently populate the fine structure states? Why is the coherence observable in the second ionization step? Why is the 16B rotational line spacing dominant in the rotational spectrum? Are the wave packets (both electronic and rotational) populated in the ion or the neutral? Some of these questions, such as the last one, may be answered by delay dependent measurement of the entire TOF spectrum which can be carried out in the same experimental setup.

6.4.4 Summary and Conclusions

This chapter was a survey of work in progress. We presented two possible applications of the rotational wave packet method detailed in chapter 5 – measuring the amplitudes and phases for n-photon ATI and HHG dipoles. Preliminary data for both experiments were collected and an initial analysis of the photoelectron yield of one ATI channel indicated sensitivity to orbital symmetry like the ion yields measured in the previous chapter. While the ATI data contain alignment angle dependent phase information which can in principle be extracted by a retrieval algorithm, the HHG data do not and an independent phase measurement needs to be made. The HHG data were taken in collaboration with the group of Carlos Trallero. We also presented work done in collaboration with the group of Martin

Centurion at the University of Nebraska. Here, theoretical calculations showed that the 3D structure of a 1D aligned asymmetric top molecule could be measured by electron diffraction in the gas phase. The Nebraska group aims to implement such measurements and apply them to measure dynamically evolving structure in excited states. Finally we discussed a collaboration with Artem Rudenko which departs from the theme of rotational wave packets in asymmetric top molecules. Here we populate a wave packet of electronic fine structure states and rotational states in CO_2^+. We observe the decay of the electronic coherence as a result of the rotational motion.

The intent of this chapter was not only to present the spate of collaborations resulting from the experimental and theoretical work detailed in prior chapters, but also a small selection of the numerous possible experiments that this author will not get the opportunity to perform and are left to future student and postdocs. As such we feel that this is a suitable concluding chapter to this thesis. A brief summary of the thesis follows.

Chapter 7

Summary and Concluding Remarks

7.1 Summary

In the introduction of this dissertation the goal was defined as the development of techniques that will allow fully differential measurements to be made on molecules in the gas phase. Specifically, we aimed to develop such methods for asymmetric top molecules and such that the measurements could be made under field-free conditions. We must now examine the work presented in the dissertation and ask if this goal was in fact accomplished. In the following we recap the development of the two essential contributions of the work presented here and set them in the context of fully differential measurement.

We took the view that understanding the rotational dynamics of laser excited asymmetric top molecules was essential to the development of fully differential measurements. Initially, the examination of these dynamics through a metric for 3D alignment enabled the design of a multi-pulse scheme leading to substantial field-free 3D alignment(FF3DA). First the metric was determined with the fundamental idea that in a 3D aligned distribution molecules are found in four equivalent target orientations each separated by a π rotation about the X, Y or Z axis – a 3D aligned distribution has D_2 symmetry. The squared sum of the cosines of the rotation angles from any orientation into each of the four targets was shown to be a

good metric for 3D alignment. This metric required coordinated motion of the molecules about the z and Z axes for an improvement in the degree of 3D alignment.

The metric was used to examine the two pulse method used by Lee *et al.* to generate FF3DA. In this method a linearly polarized laser pulse impulsively aligns the most polarizable axis of the molecules and a time delayed perpendicularly polarized pulse spins the molecular planes into alignment. TDSE calculations of the metric as a function of time after such a pulse pair interacting with iodobenzene molecules revealed the moment of strongest FF3DA, rotational revivals which require the coordinated motion about the z and Z axes and a substantial revival of the initial FF3DA.

In a related effort we attempted to find a measurable quantity that reflected the degree of 3D alignment of gaseous molecules. For this we turned to an optical measurement of alignment. Specifically, we measured the degenerate four-wave-mixing signal from a rotationally excited molecular gas. The measured signal was proportional to a component of the susceptibility tensor of the gas, which in turn is dependent on the symmetry of the gas. Though we were not able to definitively show that 3D alignment can be measured this way, we did observe that the measurement is sensitive to the 3D rotational motion of the molecule.

A crucial limitation of the two pulse method of FF3DA is that the second pulse degrades the alignment of the most polarizable axis, precluding the use of multiple pulses to improve the alignment. An examination of the interaction potential of the laser pulse with the molecule showed that an elliptically polarized pulse with a $\epsilon_X^2 < 2/3$ would enhance rather than degrade the alignment of the most polarizable axis, permitting the use of multiple pulses. Numerical calculations of the metric showed that a linearly polarized pulse followed by four elliptically polarized pulses with $\epsilon_X^2 = 0.35$ induce strong FF3DA in iodobenzene.The pulses were timed to arrive just before the peak FF3DA induced by the previous pulses. In an experimental implementation of the method we demonstrated strong FF3DA of (3,5) difluoroiodobenzene with three of the five pulses. A report of this experiment was published

in *Physical Review Letters*[42].

While FF3DA enables field-free molecular frame measurements of molecules with D_{nh} ($n < 3$) point group symmetry, the experimental geometry makes it unfeasible to control the Euler angle χ. Therefore, the measurement cannot be made for an arbitrary molecular orientation and fully differential information is not available. We developed a technique to overcome this limitation. A linearly polarized laser pulse excites coherent rotations about both θ and χ. Measurements made from such a 2D wave packet were then used to extract the 2D angle dependence of the non-dissociative strong field ionization yield of the ethylene molecular ion. The structure of the angle dependent yield allowed the identification of the orbitals from which the electron was ionized. To the best of our knowledge this is the first fully angle resolved measurement from an asymmetric top molecule. We also applied the technique to the dissociative ionization of ethylene. In this case the angle resolved yields of the charged fragments indicated from which ionic states the fragmentation initiated.

As another application of this technique, we measured the delay dependent photoelectron momentum distribution for non-dissociative strong field ionization of ethylene. Only a preliminary analysis of the data was presented. First, the distributions were integrated over the emission angle of the electron and the yields of different multi-photon ionization peaks as a function of delay were analyzed. The preliminary 2D angle dependence of these peaks also indicated the orbitals involved in the ionization process. Since electrons ejected in the same direction from molecules in different orientations should interfere coherently, the measured momentum distributions may be interpreted as interference patterns. The implications of such an interpretation were discussed and the possibility of extracting the alignment-angle dependent ionization phase was considered.

We also discussed a related experiment carried out in collaboration with Carlos Trallero's group in which higher order harmonics were measured as a function of delay from a rotational wave packet in ethylene. Like photoelectrons, harmonics from molecules in different orientations interfere, however since neighboring harmonics do not overlap, a separate exper-

iment is required to measure the phase. Other collaborative work with Martin Centurion's group to demonstrate that the structure of 1D aligned asymmetric tops could be measured by gas phase electron diffraction. A collaboration with Artem Rudenko to measure an electronic wave packet of fine structure states in the CO_2 ion is also described. While these do not conform to the theme of differential measurements form asymmetric tops, they result from the theoretical and experimental methods developed towards this goal.

7.2 Concluding Remarks

These experimental and theoretical developments encompass our efforts to make fully differential measurements with asymmetric tops possible. While FF3DA offers an opportunity to make dynamic, molecular frame measurements on molecules in excited electronic states, measurements as a function of both alignment angles are prohibitively difficult. Our method of extracting alignment-angle dependent information from pump-probe time delay dependent measurement provides a way to overcome this difficulty. This technique allows the measurement of the alignment angle dependence of any process that permits the separation of vibronic and rotational degrees of freedom. In doing so it certainly provides a route to differential measurements with respect to the alignment angles. Since alignment-angle resolution is an essential part of a fully differential measurement, this method represents substantial progress towards making such measurements.

Bibliography

[1] D. Dill, J. Chem. Phys. **65**, 1130 (1976), URL http://scitation.aip.org/content/aip/journal/jcp/65/3/10.1063/1.433187.

[2] E. Shigemasa, J. Adachi, M. Oura, and A. Yagishita, Phys. Rev. Lett. **74**, 359 (1995), URL http://link.aps.org/doi/10.1103/PhysRevLett.74.359.

[3] B. Friedrich and D. Herschbach, Phys. Rev. Lett. **74**, 4623 (1995), URL http://link.aps.org/doi/10.1103/PhysRevLett.74.4623.

[4] T. Weber, A. Czasch, O. Jagutzki, A. Müller, V. Mergel, A. Kheifets, J. Feagin, E. Rotenberg, G. Meigs, M. H. Prior, et al., Phys. Rev. Lett. **92**, 163001 (2004), URL http://link.aps.org/doi/10.1103/PhysRevLett.92.163001.

[5] J. B. Williams, C. S. Trevisan, M. S. Schöffler, T. Jahnke, I. Bocharova, H. Kim, B. Ulrich, R. Wallauer, F. Sturm, T. N. Rescigno, et al., Phys. Rev. Lett. **108**, 233002 (2012), URL http://link.aps.org/doi/10.1103/PhysRevLett.108.233002.

[6] E. Hamilton, T. Seideman, T. Ejdrup, M. D. Poulsen, C. Z. Bisgaard, S. S. Viftrup, and H. Stapelfeldt, Phys. Rev. A **72**, 043402 (2005), URL http://link.aps.org/doi/10.1103/PhysRevA.72.043402.

[7] E. Péronne, M. D. Poulsen, C. Z. Bisgaard, H. Stapelfeldt, and T. Seideman, Phys. Rev. Lett. **91**, 043003 (2003), URL http://link.aps.org/doi/10.1103/PhysRevLett.91.043003.

[8] J. G. Underwood, B. J. Sussman, and A. Stolow, Phys. Rev. Lett. **94**, 143002 (2005), URL http://link.aps.org/doi/10.1103/PhysRevLett.94.143002.

[9] K. F. Lee, D. M. Villeneuve, P. B. Corkum, A. Stolow, and J. G. Underwood, Phys. Rev. Lett. **97**, 173001 (2006), URL http://link.aps.org/doi/10.1103/PhysRevLett.97.173001.

[10] T. Osipov, M. Stener, A. Belkacem, M. Schöffler, T. Weber, L. Schmidt, A. Landers, M. H. Prior, R. Dörner, and C. L. Cocke, Phys. Rev. A **81**, 033429 (2010), URL http://link.aps.org/doi/10.1103/PhysRevA.81.033429.

[11] L. H. et al., Nature Physics **6**, 428 (2010), URL http://www.nature.com/nphys/journal/v6/n6/full/nphys1666.html.

[12] J. Maurer, D. Dimitrovski, L. Christensen, L. B. Madsen, and H. Stapelfeldt, Phys. Rev. Lett. **109**, 123001 (2012), URL http://link.aps.org/doi/10.1103/PhysRevLett.109.123001.

[13] J. L. H. et al., J. Phys. B **45**, 015101 (2012), URL http://iopscience.iop.org/0953-4075/45/1/015101.

[14] J. Mikosch, A. E. Boguslavskiy, I. Wilkinson, M. Spanner, S. Patchkovskii, and A. Stolow, Phys. Rev. Lett. **110**, 023004 (2013), URL http://link.aps.org/doi/10.1103/PhysRevLett.110.023004.

[15] I. V. Litvinyuk, K. F. Lee, P. W. Dooley, D. M. Rayner, D. M. Villeneuve, and P. B. Corkum, Phys. Rev. Lett. **90**, 233003 (2003), URL http://link.aps.org/doi/10.1103/PhysRevLett.90.233003.

[16] T. Kanai, S. Minemoto, and H. Sakai., Nature **435**, 470 (2005), URL http://www.nature.com/nature/journal/v435/n7041/full/nature03577.html.

[17] C. Z. Bisgaard, O. J. Clarkin, G. Wu, A. M. D. Lee, O. Gener, C. C. Hayden, and A. Stolow, Science **323**, 1464 (2009), URL http://www.sciencemag.org/content/323/5920/1464.abstract.

[18] D. Griffiths, *Introduction to Quantum Mechanics, Second Edition* (Upper Saddle River, NJ 07458: Pearson Prentice Hall, 2005).

[19] D. R. Herschbach, G. H. Kwei, and J. A. Norris, The Journal of Chemical Physics **34**, 1842 (1961), URL http://scitation.aip.org/content/aip/journal/jcp/34/5/10.1063/1.1701089.

[20] K. H. Kramer and R. B. Bernstein, J. Chem. Phys. **42**, 767 (1965), URL http://scitation.aip.org/content/aip/journal/jcp/42/2/10.1063/1.1696004.

[21] P. R. Brooks and E. M. Jones, J. Chem. Phys. **45**, 3449 (1966), URL http://scitation.aip.org/content/aip/journal/jcp/45/9/10.1063/1.1728128.

[22] S. Kaesdorf, G. Schönhense, and U. Heinzmann, Phys. Rev. Lett. **54**, 885 (1985), URL http://link.aps.org/doi/10.1103/PhysRevLett.54.885.

[23] P. R. Brooks, Science **193**, 11 (1976), URL http://www.sciencemag.org/content/193/4247/11.abstract.

[24] R. B. Bernstein, D. R. Herschbach, and R. D. Levine, The Journal of Physical Chemistry **91**, 5365 (1987), URL http://pubs.acs.org/doi/abs/10.1021/j100305a001.

[25] T. P. Rakitzis, A. J. van den Brom, and M. H. M. Janssen, Science **303**, 1852 (2004), URL http://www.sciencemag.org/content/303/5665/1852.abstract?sid=41990c5d-d702-4295-be2c-898afe641e4f.

[26] R. N. Zare, Mol. Photochem **4**, 1 (1972), URL http://web.stanford.edu/group/Zarelab/publinks/zarepub60.pdf.

[27] J. D. H. Eland, J. Mass Spectrom. Ion Phys. **8**, 143 (1972), URL http://www.sciencedirect.com/science/article/pii/0020738172800044.

[28] J. H. D. Eland, J. Chem. Phys. **70**, 2926 (1979), URL http://scitation.aip.org/content/aip/journal/jcp/70/6/10.1063/1.437831.

[29] A. V. Golovin, V. V. Kuznetsov, and N. A. Cherepkov, Sov. Tech. Phys. Lett. **16**, 363 (1990).

[30] G. Mainfray and G. Manus, J. Phys. B **54**, L497 (1992), URL http://iopscience.iop.org/0034-4885/54/10/002.

[31] D. Normand, L. A. Lompre, and C. Cornaggia, J. Phys. B **25**, L497 (1992), URL http://iopscience.iop.org/0953-4075/25/20/001.

[32] W. Kim and P. M. Felker, J. Chem. Phys. **104**, 1147 (1996), URL http://scitation.aip.org/content/aip/journal/jcp/104/3/10.1063/1.470770.

[33] H. Sakai, C. P. Safvan, J. J. Larsen, K. M. Hilligsøe, K. Hald, and H. Stapelfeldt, J. Chem. Phys. **110**, 10235 (1999), URL http://scitation.aip.org/content/aip/journal/jcp/110/21/10.1063/1.478039.

[34] J. J. Larsen, H. Sakai, C. P. Safvan, I. Wendt-Larsen, and H. Stapelfeldt, J. Chem. Phys. **111**, 7774 (1999), URL http://scitation.aip.org/content/aip/journal/jcp/111/17/10.1063/1.480112.

[35] J. J. Larsen, K. Hald, N. Bjerre, H. Stapelfeldt, and T. Seideman, Phys. Rev. Lett. **85**, 2470 (2000), URL http://link.aps.org/doi/10.1103/PhysRevLett.85.2470.

[36] A. H. Zewail, The Journal of Physical Chemistry A **104**, 5660 (2000), URL http://pubs.acs.org/doi/abs/10.1021/jp001460h.

[37] T. Seideman, Phys. Rev. Lett. **83**, 4971 (1999), URL http://link.aps.org/doi/10.1103/PhysRevLett.83.4971.

[38] C. H. Lin, J. P. Heritage, and T. K. Gustafson, Applied Physics Letters **19**, 397 (1971), URL http://scitation.aip.org/content/aip/journal/apl/19/10/10.1063/1.1653745.

[39] J. P. Heritage, T. K. Gustafson, and C. H. Lin, Phys. Rev. Lett. **34**, 1299 (1975), URL http://link.aps.org/doi/10.1103/PhysRevLett.34.1299.

[40] P. M. Felker, The Journal of Physical Chemistry **96**, 7844 (1992), URL http://pubs.acs.org/doi/abs/10.1021/j100199a005.

[41] F. Rosca-Pruna and M. J. J. Vrakking, Phys. Rev. Lett. **87**, 153902 (2001), URL http://link.aps.org/doi/10.1103/PhysRevLett.87.153902.

[42] X. Ren, V. Makhija, and V. Kumarappan, Phys. Rev. Lett. **112**, 173602 (2014), URL http://link.aps.org/doi/10.1103/PhysRevLett.112.173602.

[43] J. Ullrich, R. Moshammer, A. Dorn, R. Dörner, L. P. H. Schmidt, and H. Schmidt-Böcking, Reports on Progress in Physics **66**, 1463 (2003), URL http://stacks.iop.org/0034-4885/66/i=9/a=203.

[44] A. Stolow and J. G. Underwood, *Time-Resolved Photoelectron Spectroscopy of Nonadiabatic Dynamics in Polyatomic Molecules* (John Wiley and Sons, Inc., 2008), pp. 497–584, URL http://dx.doi.org/10.1002/9780470259498.ch6.

[45] X. M. Tong, Z. X. Zhao, and C. D. Lin, Phys. Rev. A **66**, 033402 (2002), URL http://link.aps.org/doi/10.1103/PhysRevA.66.033402.

[46] T. K. Kjeldsen, C. Z. Bisgaard, L. B. Madsen, and H. Stapelfeldt, Phys. Rev. A **71**, 013418 (2005), URL http://link.aps.org/doi/10.1103/PhysRevA.71.013418.

[47] D. Tong (2012), from online lecture notes on classical dynamics, URL http://www.damtp.cam.ac.uk/user/tong/dynamics.html.

[48] C. Townes and A. Schawlow, *Microwave Spectroscopy* (Mineola, New York: Dover Publications Inc., 1975).

[49] P. R. Bunker and P. Jensen, *Molecular Symmetry and Spectroscopy, Second Edition* (Ontario: NRC Research Press, 1998).

[50] R. N. Zare, *Angular Momentum: Understanding Spatial Aspects in Chemistry and Physics* (Hoboken, NJ 07030: John Wiley and Sons - Wiley Interscience, 1988).

[51] C. V. Winter, Physica **20**, 274 (1954), URL http://www.sciencedirect.com/science/article/pii/S0031891454800413.

[52] E. E. P. Wigner and I. Edition, *Group Theory and its Application to the Quantum Mechanics of Atomic Spectra* (New York, NY 10003: Academic Press Inc., 1959).

[53] D. M. Brink and G. R. Satchler, *Angular Momentum, Third Edition* (Oxford OX2 6DP: Oxford University Press., 1993).

[54] W. H. Press, S. A. Teukolsky, W. T. Vetterling, and B. P. Flannery, *Numerical Recipes 3rd Edition: The Art of Scientific Computing* (Cambridge University Press, 2007).

[55] C. W. Misner, Phys. Rev. Lett. **22**, 1071 (1969), URL http://link.aps.org/doi/10.1103/PhysRevLett.22.1071.

[56] B. L. Hu, Phys. Rev. D **8**, 1048 (1973), URL http://link.aps.org/doi/10.1103/PhysRevD.8.1048.

[57] J. S. Dowker and D. F. Pettengill, Journal of Physics A: Mathematical, Nuclear and General **7**, 1527 (1974), URL http://stacks.iop.org/0301-0015/7/i=13/a=007.

[58] V. Kumarappan, C. Z. Bisgaard, S. S. Viftrup, L. Holmegaard, and H. Stapelfeldt, The Journal of Chemical Physics **125** (2006), URL http://scitation.aip.org/content/aip/journal/jcp/125/19/10.1063/1.2388273.

[59] U. Even, J. Jortner, D. Noy, N. Lavie, and C. Cossart-Magos, J. Chem. Phys. **112**, 8068 (2000), URL http://scitation.aip.org/content/aip/journal/jcp/112/18/10.1063/1.481405.

[60] G. Scoles, *Atomic and Molecular Beam Methods, Volume 1* (New York, New York:Oxford University Press, 1988).

[61] K. Luria, W. Christen, and U. Even, The Journal of Physical Chemistry A **115**, 7362 (2011), URL http://pubs.acs.org/doi/abs/10.1021/jp201342u.

[62] X. Ren, V. Makhija, and V. Kumarappan, Phys. Rev. Lett. **112**, 173602 (2014), URL http://link.aps.org/doi/10.1103/PhysRevLett.112.173602.

[63] X. Ren, Ph.D. thesis, Kansas State University, Department of Physics (2013), URL https://krex.k-state.edu/dspace/handle/2097/15954.

[64] A. T. J. B. Eppink and D. H. Parker, Review of Scientific Instruments **68**, 3477 (1997), URL http://scitation.aip.org/content/aip/journal/rsi/68/9/10.1063/1.1148310.

[65] D. R. Baum and J. M. Winget, SIGGRAPH Comput. Graph. **24**, 67 (1990), URL http://doi.acm.org/10.1145/91394.91420.

[66] H. Haus, IEEE Journal of Quantum Electronics, **12**, 169 (1976), URL http://ieeexplore.ieee.org/xpls/abs_all.jsp?arnumber=1069112.

[67] E. W. Moon, Ph.D. thesis, Kansas State University, Department of Physics (2009), URL https://krex.k-state.edu/dspace/handle/2097/1125.

[68] P. Maine, D. Strickland, P. Bado, M. Pessot, and G. Mourou, IEEE Journal of Quantum Electronics **24**, 398 (1988), URL http://ieeexplore.ieee.org/xpls/abs_all.jsp?arnumber=137.

[69] M. Artamonov and T. Seideman, The Journal of Chemical Physics **128**, 154313 (2008), URL http://scitation.aip.org/content/aip/journal/jcp/128/15/10.1063/1.2894876.

[70] S. S. Viftrup, V. Kumarappan, S. Trippel, H. Stapelfeldt, E. Hamilton, and T. Seideman, Phys. Rev. Lett. **99**, 143602 (2007), URL http://link.aps.org/doi/10.1103/PhysRevLett.99.143602.

[71] S. Pabst, P. J. Ho, and R. Santra, Phys. Rev. A **81**, 043425 (2010), URL http://link.aps.org/doi/10.1103/PhysRevA.81.043425.

[72] A. Rouzée, S. Guérin, O. Faucher, and B. Lavorel, Phys. Rev. A **77**, 043412 (2008), URL http://link.aps.org/doi/10.1103/PhysRevA.77.043412.

[73] V. Makhija, X. Ren, and V. Kumarappan, Phys. Rev. A **85**, 033425 (2012), URL http://link.aps.org/doi/10.1103/PhysRevA.85.033425.

[74] D. Huynh, Journal of Mathematical Imaging and Vision **35**, 155 (2009), ISSN 0924-9907, URL http://dx.doi.org/10.1007/s10851-009-0161-2.

[75] H. Goldsetin, *Classical Mechanics, Second Edition* (Reading, MA:Addison-Wesley., 1980).

[76] N. Takemoto and K. Yamanouchi, Chemical Physics Letters **451**, 1 (2008), URL http://www.sciencedirect.com/science/article/pii/S0009261407015655.

[77] S. Pabst and R. Santra, Phys. Rev. A **81**, 065401 (2010), URL http://link.aps.org/doi/10.1103/PhysRevA.81.065401.

[78] M. Wollenhaupt, M. Krug, J. Khler, T. Bayer, C. Sarpe-Tudoran, and T. Baumert, Applied Physics B **95**, 647 (2009), URL http://dx.doi.org/10.1007/s00340-009-3513-0.

[79] C. T. Middleton, K. de La Harpe, C. Su, Y. K. Law, C. E. Crespo-Hernndez, and B. Kohler, Annual Review of Physical Chemistry **60**, 217 (2009), URL http://dx.doi.org/10.1146/annurev.physchem.59.032607.093719.

[80] H. R. Hudock, B. G. Levine, A. L. Thompson, H. Satzger, D. Townsend, N. Gador, S. Ullrich, A. Stolow, and T. J. Martnez, The Journal of Physical Chemistry A **111**, 8500 (2007), URL http://pubs.acs.org/doi/abs/10.1021/jp0723665.

[81] J. R. Lalanne, A. Ducasse, and S.Kielich, *Laser-Molecule Interaction* (Hoboken, NJ 07030: John Wiley and Sons - Wiley Interscience, 1996).

[82] V. Renard, M. Renard, S. Guérin, Y. T. Pashayan, B. Lavorel, O. Faucher, and H. R. Jauslin, Phys. Rev. Lett. **90**, 153601 (2003), URL http://link.aps.org/doi/10.1103/PhysRevLett.90.153601.

[83] A. Rouzée, V. Renard, S. Guérin, O. Faucher, and B. Lavorel, Phys. Rev. A **75**, 013419 (2007), URL http://link.aps.org/doi/10.1103/PhysRevA.75.013419.

[84] Y.-H. Chen, S. Varma, A. York, and H. M. Milchberg, Opt. Express **15**, 11341 (2007), URL http://www.opticsexpress.org/abstract.cfm?URI=oe-15-18-11341.

[85] R. W. Boyd, *Nonlinear Optics, Third Edition* (Burlington, MA 01803: Academic Press, Elsevier, 2008).

[86] R. F. Begley, A. B. Harvey, and R. L. Byer, Applied Physics Letters **25**, 387 (1974), URL http://scitation.aip.org/content/aip/journal/apl/25/7/10.1063/1.1655519.

[87] . . Harvey, Analytical Chemistry **50**, 905A (1978), URL http://pubs.acs.org/doi/abs/10.1021/ac50031a774.

[88] I. R. Beattie, T. R. Gilson, and D. A. Greenhalgh, Nature **276**, 378 (1978), URL http://scitation.aip.org/content/aip/journal/apl/25/7/10.1063/1.1655519.

[89] J. A. Shirley, R. J. Hall, and A. C. Eckbreth, Opt. Lett. **5**, 380 (1980), URL http://ol.osa.org/abstract.cfm?URI=ol-5-9-380.

[90] R. P. Davis, A. J. Moad, G. S. Goeken, R. D. Wampler, and G. J. Simpson, The Journal of Physical Chemistry B **112**, 5834 (2008), URL http://pubs.acs.org/doi/abs/10.1021/jp709961k.

[91] N. Matsuzawa and D. A. Dixon, The Journal of Physical Chemistry **98**, 2545 (1994), URL http://pubs.acs.org/doi/abs/10.1021/j100061a008.

[92] H. R. Reiss, Phys. Rev. A **22**, 1786 (1980), URL http://link.aps.org/doi/10.1103/PhysRevA.22.1786.

[93] G. F. Gribakin and M. Y. Kuchiev, Phys. Rev. A **55**, 3760 (1997), URL http://link.aps.org/doi/10.1103/PhysRevA.55.3760.

[94] M. Lewenstein, P. Balcou, M. Y. Ivanov, A. L'Huillier, and P. B. Corkum, Phys. Rev. A **49**, 2117 (1994), URL http://link.aps.org/doi/10.1103/PhysRevA.49.2117.

[95] L. Keldysh, Sov. Phys. JETP **20**, 1307 (1965).

[96] C. D. Lin, *AMO physics 2*, Class lecture notes (2011).

[97] J. C. Lorquet, C. Sannen, and G. Raseev, Journal of the American Chemical Society **102**, 7976 (1980), URL http://pubs.acs.org/doi/abs/10.1021/ja00547a045.

[98] M. H. Kim, B. D. Leskiw, and A. G. Suits, The Journal of Physical Chemistry A **109**, 7839 (2005), URL http://pubs.acs.org/doi/abs/10.1021/jp053143m.

[99] R. Stockbauer and M. G. Inghram, JCP **62**, 4862 (1975), URL http://scitation.aip.org/content/aip/journal/jcp/62/12/10.1063/1.430398.

[100] B. Joalland, T. Mori, T. J. Martnez, and A. G. Suits, The Journal of Physical Chemistry Letters **5**, 1467 (2014), http://pubs.acs.org/doi/pdf/10.1021/jz500352x, URL http://pubs.acs.org/doi/abs/10.1021/jz500352x.

[101] X. Xie, S. Roither, M. Schöffler, E. Lötstedt, D. Kartashov, L. Zhang, G. G. Paulus, A. Iwasaki, A. Baltuška, K. Yamanouchi, et al., Phys. Rev. X **4**, 021005 (2014), URL http://link.aps.org/doi/10.1103/PhysRevX.4.021005.

[102] E. Wells, C. Rallis, M. Zohrabi, R. Siemering, B. Jochim, P. Andrews, U. Ablikim, B. Gaire, S. De, K. Carnes, et al., Nature communications **4**, 3895 (2013), URL http://www.nature.com/ncomms/2013/131206/ncomms3895/full/ncomms3895.html?message-global=remove.

[103] J. Yang, V. Makhija, V. Kumarappan, and M. Centurion, Structural Dynamics **1**, 044101 (2014), URL http://scitation.aip.org/content/aip/journal/sdy/1/4/10.1063/1.4889840.

[104] N. G. Kling, D. Paul, A. Gura, G. Laurent, S. De, H. Li, Z. Wang, B. Ahn, C. H. Kim, T. K. Kim, et al., Journal of Instrumentation **9**, P05005 (2014), URL http://stacks.iop.org/1748-0221/9/i=05/a=P05005.

[105] G. R. Branton, D. C. Frost, T. Makita, C. A. McDowell, and I. A. Stenhouse, The Journal of Chemical Physics **52**, 802 (1970), URL http://scitation.aip.org/content/aip/journal/jcp/52/2/10.1063/1.1673058.

[106] A. Rudenko, K. Zrost, C. D. Schrter, V. L. B. de Jesus, B. Feuerstein, R. Moshammer, and J. Ullrich, Journal of Physics B: Atomic, Molecular and Optical Physics **37**, L407 (2004), URL http://stacks.iop.org/0953-4075/37/i=24/a=L03.

[107] F. Yergeau, G. Petite, and P. Agostini, Journal of Physics B: Atomic and Molecular Physics **19**, L663 (1986), URL http://stacks.iop.org/0022-3700/19/i=19/a=005.

[108] R. R. Freeman, P. H. Bucksbaum, H. Milchberg, S. Darack, D. Schumacher, and M. E. Geusic, Phys. Rev. Lett. **59**, 1092 (1987), URL http://link.aps.org/doi/10.1103/PhysRevLett.59.1092.

[109] R. M. Potvliege and S. Vui, Journal of Physics B: Atomic, Molecular and Optical Physics **42**, 055603 (2009), URL http://stacks.iop.org/0953-4075/42/i=5/a=055603.

[110] G. A. Garcia, L. Nahon, and I. Powis, Review of Scientific Instruments **75**, 4989 (2004), URL http://scitation.aip.org/content/aip/journal/rsi/75/11/10.1063/1.1807578.

[111] P. Hockett, ArXiv e-prints (2014), provided by the SAO/NASA Astrophysics Data System, 1404.3559, URL http://adsabs.harvard.edu/abs/2014arXiv1404.3559H.

[112] R. Trebino, K. W. DeLong, D. N. Fittinghoff, J. N. Sweetser, M. A. Krumbgel, B. A. Richman, and D. J. Kane, Review of Scientific Instruments **68**, 3277 (1997), URL http://scitation.aip.org/content/aip/journal/rsi/68/9/10.1063/1.1148286.

[113] C. Vozzi, M. Negro, F. Calegari, G. Sansone, M. Nisoli, S. De Silvestri, and S. Stagira, Nature Physics **7**, 822 (2011), URL http://www.nature.com/nphys/journal/v7/n10/abs/nphys2029.html.

[114] K. L. Reid, D. J. Leahy, and R. N. Zare, Phys. Rev. Lett. **68**, 3527 (1992), URL http://link.aps.org/doi/10.1103/PhysRevLett.68.3527.

[115] P. B. Corkum, Phys. Rev. Lett. **71**, 1994 (1993), URL http://link.aps.org/doi/10.1103/PhysRevLett.71.1994.

[116] N. L. Wagner, Master's thesis, University of Colorado,Boulder (2008), URL https://jila.colorado.edu/publications/high-order-harmonic-generation-molecules.

[117] C. B. Madsen, A. S. Mouritzen, T. K. Kjeldsen, and L. B. Madsen, Phys. Rev. A **76**, 035401 (2007), URL http://link.aps.org/doi/10.1103/PhysRevA.76.035401.

[118] S. Baker, J. S. Robinson, C. A. Haworth, H. Teng, R. A. Smith, C. C. Chiril, M. Lein,

J. W. G. Tisch, and J. P. Marangos, Science **312**, 424 (2006), URL http://www.sciencemag.org/content/312/5772/424.abstract.

[119] C. J. Hensley, J. Yang, and M. Centurion, Phys. Rev. Lett. **109**, 133202 (2012), URL http://link.aps.org/doi/10.1103/PhysRevLett.109.133202.

[120] P. W. Allen and L. E. Sutton, Acta Crystallographica **3**, 46 (1950), URL http://dx.doi.org/10.1107/S0365110X50000100.

[121] H. Ihee, V. A. Lobastov, U. M. Gomez, B. M. Goodson, R. Srinivasan, C.-Y. Ruan, and A. H. Zewail, Science **291**, 458 (2001).

[122] R. Srinivasan, J. S. Feenstra, S. T. Park, S. Xu, and A. H. Zewail, Science **307**, 558 (2005), URL http://www.sciencemag.org/content/307/5709/558.abstract.

[123] C. I. Blaga, J. Xu, A. D. DiChiara, E. Sistrunk, K. Zhang, P. Agostini, T. A. Miller, L. F. DiMauro, and C. Lin, Nature **483**, 194 (2012), URL http://www.nature.com/nature/journal/v483/n7388/abs/nature10820.html.

[124] M. Centurion, *Division of atomic, molecular and optical physics aps meeting*, personal communication (2014).

[125] F. Merkt, S. R. Mackenzie, R. J. Rednall, and T. P. Softley, The Journal of Chemical Physics **99**, 8430 (1993), URL http://scitation.aip.org/content/aip/journal/jcp/99/11/10.1063/1.466212.

[126] M. J. J. Vrakking, D. M. Villeneuve, and A. Stolow, Phys. Rev. A **54**, R37 (1996), URL http://link.aps.org/doi/10.1103/PhysRevA.54.R37.

[127] B. J. Sussman, J. G. Underwood, R. Lausten, M. Y. Ivanov, and A. Stolow, Phys. Rev. A **73**, 053403 (2006), URL http://link.aps.org/doi/10.1103/PhysRevA.73.053403.

[128] P. M. Kraus, S. B. Zhang, A. Gijsbertsen, R. R. Lucchese, N. Rohringer, and H. J. Wörner, Phys. Rev. Lett. **111**, 243005 (2013), URL http://link.aps.org/doi/10.1103/PhysRevLett.111.243005.

[129] J. L. Neill, S. T. Shipman, L. Alvarez-Valtierra, A. Lesarri, Z. Kisiel, and B. H. Pate, Journal of Molecular Spectroscopy **269**, 21 (2011), URL http://www.sciencedirect.com/science/article/pii/S0022285211001044.

[130] B. Bak, D. Christensen, J. Rastrup Andersen, and E. Tannenbaum, The Journal of Chemical Physics **25**, 892 (1956), URL http://scitation.aip.org/content/aip/journal/jcp/25/5/10.1063/1.1743138.

[131] V. Vaquero, M. E. Sanz, J. C. Lpez, and J. L. Alonso, The Journal of Physical Chemistry A **111**, 3443 (2007), URL http://dx.doi.org/10.1021/jp071642c.

[132] V. V. Ilyushin, L. B. Favero, W. Caminati, and J.-U. Grabow, ChemPhysChem **11**, 2589 (2010), URL http://dx.doi.org/10.1002/cphc.201000223.

[133] M. Oftadeh, S. Naseh, and M. Hamadanian, Computational and Theoretical Chemistry **966**, 20 (2011), URL http://www.sciencedirect.com/science/article/pii/S2210271X11000727.

[134] S. Millefiori and A. Alparone, Chemical Physics **303**, 27 (2004), URL http://www.sciencedirect.com/science/article/pii/S0301010404002083.

[135] R. Chelli and P. Procacci, The Journal of Chemical Physics **117**, 9175 (2002), URL http://scitation.aip.org/content/aip/journal/jcp/117/20/10.1063/1.1515773.

[136] S. Willitsch, U. Hollenstein, and F. Merkt, The Journal of Chemical Physics **120**, 1761 (2004), URL http://scitation.aip.org/content/aip/journal/jcp/120/4/10.1063/1.1635815.

Appendix A

Derivation of matrix elements

Matrix elements used in this thesis are derived by first rewriting the quantity of interest in terms of the Wigner rotation matrices, which are an irreducable representation on the three dimensional rotation group SO(3). We therefore provide the matrix elements of these functions, and rewrite the other quantities of interest in terms of these matrix elements.

A.1 Wigner Rotation Matrices

We require elements of the Wigner matrices $D^j_{m,k}$ in the symmetric top basis $|JKM\rangle$. The basis functions themseleves can be represented in terms of the Euler angles as Wigner matrix elements,

$$\langle \mathbf{\Omega} | JKM \rangle = \sqrt{\frac{2J+1}{8\pi^2}} D^{J*}_{M,K}. \tag{A.1}$$

The desired matrix elements are then,

$$\langle JKM | \, D^j_{m,k} \, | J'K'M' \rangle = \frac{\sqrt{(2J+1)(2J'+1)}}{8\pi^2} \int d\mathbf{\Omega} D^J_{M,K} D^j_{m,k} D^{J'*}_{M',K'}. \tag{A.2}$$

The method for solving the integral is given in Zare[50]. The result is stated here,

$$\int d\mathbf{\Omega} D^{J}_{M,K} D^{j}_{m,k} D^{J'*}_{M',K'} = \frac{8\pi^2}{2J'+1} \langle J, M; j, m | J', M' \rangle \langle J, K; j, k | J', K' \rangle . \tag{A.3}$$

The resulting matrix elements for the $D^{j}_{m,k}$ are then

$$\langle JKM | D^{j}_{m,k} | J'K'M' \rangle = \sqrt{\frac{(2J+1)}{(2J'+1)}} \langle J, M; j, m | J', M' \rangle \langle J, K; j, k | J', K' \rangle . \tag{A.4}$$

This equation can be used to obtain matrix elements of any quantity that can be expressed in terms of the $D^{j}_{m,k}$. This can be done for the polarizability interaction potential as shown in chapter 1 (c.f. Eq. 2.14) and for the hyperpolarizability tensor components as shown in chapter 4 (c.f. Eq. 4.6). Additional matrix elements used for computation in this thesis are those of the direction cosines and the metric. In the following section we show how these can be rewritten in terms of the $D^{j}_{m,k}$.

A.2 Direction Cosines and the Metric

Only expectation values of the direction cosines representing the diagonal elements of the rotation matrix – $\langle \cos^2 \theta_{zZ} \rangle$, $\langle \cos^2 \theta_{yY} \rangle$ and $\langle \cos^2 \theta_{xX} \rangle$ – are computed in the thesis. To write them in terms of the Wigner matrix elements we first write the diagonal elements of the rotation matrix in terms of the Euler angles,

$$\begin{aligned} R_{zZ} &= \cos\theta, \\ R_{yY} &= \cos\phi \cos\chi - \cos\theta \sin\phi \sin\chi, \\ R_{xX} &= \cos\theta \cos\chi \cos\phi - \sin\phi \sin\chi. \end{aligned}$$

The above assumes a definition of the roatation matrix that conforms with that of Zare[50].Using a table of Wigner matrix elements provided by Zare the above can be trivially rewritten as

$$\begin{aligned}
\cos\theta_{zZ} &= D^1_{0,0}, \\
\cos\theta_{yY} &= \frac{1}{2}(D^1_{1,1} - D^1_{-1,1} - D^1_{1,-1} + D^1_{-1,-1}), \\
\cos\theta_{xX} &= \frac{1}{2}(D^1_{1,1} + D^1_{-1,1} + D^1_{1,-1} + D^1_{-1,-1}).
\end{aligned}$$

Squaring these gives products of the $D^j_{m,k}$ which can be reduced to a sum using the following expression[50],

$$D^{j_1}_{m_1,k_1} D^{j_2}_{m_2,k_2} = \sum_{j,k,m} \langle j_1, m_1; j_2, m_2 | j, m\rangle \langle j_1, k_1; j_2, k_2 | j, k\rangle D^j_{m,k}.$$

Applying this to the squares of the direction cosines and using Eq. A.4 gives the expressions for the matrix elements written out explicitly on the following page. Matrix elements of the metric can be easily found using the above expressions and the relation

$$\cos^2\delta = \frac{1}{4}\left(1 + \cos^2\theta_{Xx} + \cos^2\theta_{Yy} + \cos^2\theta_{Zz}\right).$$

Matrix elements of the direction cosines -

$$\begin{aligned}
&\left\langle JKM|\cos^2\theta_{yY}|J'K'M'\right\rangle = \\
&\left[\frac{1}{3}\delta_{JJ'}\delta_{KK'}\delta_{MM'} + \frac{1}{6}\sqrt{\frac{2J+1}{2J'+1}}\left\langle J,M;2,0|J',M'\right\rangle\left\langle J,K;2,0|J',K'\right\rangle\right] \\
&+\left[\frac{1}{2\sqrt{6}}\sqrt{\frac{2J+1}{2J'+1}}\Big\{\left\langle J,M;2,0|J',M'\right\rangle\left[\left\langle J,K;2,2|J',K'\right\rangle + \left\langle J,K;2,-2|J',K'\right\rangle\right]\right. \\
&\left.+\left\langle J,K;2,0|J',K'\right\rangle\left[\left\langle J,M;2,2|J',M'\right\rangle + \left\langle J,M;2,-2|J',M'\right\rangle\right]\Big\}\right] \\
&+\left[\frac{1}{4}\sqrt{\frac{2J+1}{2J'+1}}\Big\{\left[\left\langle J,K;2,2|J',K'\right\rangle + \left\langle J,K;2,-2|J',K'\right\rangle\right]\left[\left\langle J,M;2,2|J',M'\right\rangle\right. \right. \\
&\left.\left.+\left\langle J,M;2,-2|J',M'\right\rangle\right]\Big\}\right]
\end{aligned} \tag{A.5}$$

$$\begin{aligned}
&\left\langle JKM|\cos^2\theta_{xX}|J'K'M'\right\rangle = \\
&\left[\frac{1}{3}\delta_{JJ'}\delta_{KK'}\delta_{MM'} + \frac{1}{6}\sqrt{\frac{2J+1}{2J'+1}}\left\langle J,M;2,0|J',M'\right\rangle\left\langle J,K;2,0|J',K'\right\rangle\right] \\
&-\left[\frac{1}{2\sqrt{6}}\sqrt{\frac{2J+1}{2J'+1}}\Big\{\left\langle J,M;2,0|J',M'\right\rangle\left[\left\langle J,K;2,2|J',K'\right\rangle + \left\langle J,K;2,-2|J',K'\right\rangle\right]\right. \\
&\left.+\left\langle J,K;2,0|J',K'\right\rangle\left[\left\langle J,M;2,2|J',M'\right\rangle + \left\langle J,M;2,-2|J',M'\right\rangle\right]\Big\}\right] \\
&+\left[\frac{1}{4}\sqrt{\frac{2J+1}{2J'+1}}\Big\{\left[\left\langle J,K;2,2|J',K'\right\rangle + \left\langle J,K;2,2|J',K'\right\rangle\right]\left[\left\langle J,M;2,2|J',M'\right\rangle\right. \right. \\
&\left.\left.+\left\langle J,M;2,-2|J',M'\right\rangle\right]\Big\}\right]
\end{aligned} \tag{A.6}$$

$$\begin{aligned}
&\left\langle JKM|\cos^2\theta_{zZ}|J'K'M'\right\rangle = \\
&\frac{1}{3}\delta_{JJ'}\delta_{KK'}\delta_{MM'} + \frac{2}{3}\sqrt{\frac{2J+1}{2J'+1}}\left\langle J,M;2,0|J',M'\right\rangle\left\langle J,K;2,0|J',K'\right\rangle
\end{aligned} \tag{A.7}$$

Appendix B

Spherical tensor conversion coefficients

The conversion coefficients for a second rank cartesian tensor U_{ij} to a spherical tensor U^L_M are given by the follwing equations,

$$U^L_M = C^{LM}_{ij} U_{ij}, \tag{B.1}$$

$$C^{LM}_{ij} = \langle 1M'; 1M'' | LM \rangle \, A_{iM'} A_{jM''}, \tag{B.2}$$

$$A = \begin{pmatrix} 1/\sqrt{2} & -i & 0 \\ 0 & 0 & 1 \\ -1/\sqrt{2} & -i & 0 \end{pmatrix} \tag{B.3}$$

Here the $\langle ..; ..|..\rangle$ are the Clebsch Gordan coefficients and the second index of the matrix A takes the value 1,2 or 3 for $M', M'' = -1$,0 or 1. The conversion coefficients C^{LM}_{ij} apply for any second rank tensor and hence for α^L_M and U^L_M. These expressions are derived in Zare[50]. These tranformation coefficeints are used to convert between cartesian and spherical polarizability tensor components in chapter 2.

This expression can be extended to an n^th rank tensor by correctly adding angular momenta. For a fourth rank tensor we get [i],

$$U_M^L = C_{ij}^{LM} U_{ij}, \tag{B.4}$$

$$C_{ij}^{LM} = \langle 1, m_1; 1, m_2 | L_1 M_1 \rangle \langle 1, m_3; 1, m_4 | L_2 M_2 \rangle \langle L_1, M_1; L_2, M_2 | L, M \rangle A_{im_1} A_{im_2} A_{im_3} A_{im_4}, \tag{B.5}$$

$$A = \begin{pmatrix} 1/\sqrt{2} & -i & 0 \\ 0 & 0 & 1 \\ -1/\sqrt{2} & -i & 0 \end{pmatrix} \tag{B.6}$$

These trasnforamtion coefficients are used to convert between spherical and cartesian susceptibilty tensor components in chapter 4.

[i] we acknowledge Dr. Larry Weaver for a helpful discussion on spherical tensors

Appendix C

Inertia, polarizability and hyperpolarizability tensors

C.1 Intertia Tensors

The following is a table of the rotation constants for molecules studied in this thesis given in GHz.

Molecule	A (GHz)	B (GHz)	C (GHz)
Ethylene[72]	145.82	30.009	24.823
Iodobenzene[129]	5.6719	0.75042	0.66263
3,5 Difluoroiodobenzene[42]	1.48	0.484	0.379
Thiophene[130]	8.0418	5.4182	3.2358
Uracil[131]	3.8839	2.0237	1.3309
Toluene[132]	5.657	0.9462	0.8106

Table C.1: *Rotation constants for molecules studied in this thesis given in GHz.*

C.2 Polarizability Tensors

The following is a table of the diagonal components of the polarizability tensor for molecules studied in this thesis given in Å^3. We assume (3,5) difluoroiodobenzene has the same

Molecule	α_{zz} (Å^3)	α_{xx} (Å^3)	α_{yy} (Å^3)
Ethylene[72]	5.02	15.3	10.2
Iodobenzene[91]	21.5	15.3	10.2
Thiophene[133]	10.6	9.3	5.6
Uracil[134]	13.9	11.1	6.14
Toluene[135]	12.34	14.28	5.67

Table C.2: *Polarizability tensor components for the molecules studied in thesis. The values are in Å^3.*

polarizability tensor as iodobenzene. For all these molecules except Uracil the polarizabaility tensor is diagonal in the principal axes frame.

C.3 Hyperpolarizability Tensors

The DFWM experiment presented in chapter 4 is only carried out with iodobenzene. The unique non-zero components of its second hyperpolarizability tensor as calculated by Matsuzawa and Dixon[91] are tabulated below in units of 10^{-36} esu,

Tensor component	Value ($\times 10^{-36}$esu)
γ_{zzzz}	33.076
γ_{xxxx}	17.303
γ_{yyyy}	9.775
γ_{xxzz}	5.011
γ_{xxyy}	3.981
γ_{yyzz}	3.599

Table C.3: *Unique, non-zero components of the second hyperpolarizability tensor of iodobenzene.*

Since the four beams in the experiment are degenerate, components generated from all

permutations of the indices of the unique components must also be included. For instance, $\gamma_{xxyy} = \gamma_{xyxy} = \gamma_{xyyx} = \gamma_{yxxy} = \gamma_{yxyx} = \gamma_{yyxx}$.

Appendix D

Molecular symmetry and the electronic configuration of ethylene

We refer the interested reader to Bunker and Jensen[49] for a thorough treatment of the labeling of molecular energy levels using molecular symmetry. In general, any Hamiltonian may have a set of operators with which it commutes. These form the symmetry group of the Hamiltonian and the eigenstates are eigenfunctions of these operators. In chapter 2 we classified states of the rigid rotor Hamiltonian based on the eigenvalues generated when each of the symmetry operators acted on the wave functions. The set of eigenvalues thus generated form a representation of the symmetry group which can be used to label the states. The same procedure may be applied to the vibronic Hamiltonian if its symmetry group can be determined. It can be show that in general the geometric point group of the molecule is the symmetry group of the vibronic Hamiltonian[49] for a rigid molecule (no bending or twisting of bonds is allowed). The point group consists of all rotations, reflections and the products of rotations and reflections that leave the molecule unchanged.

Examining panel (b) of Fig. 5.1 indicates that ethylene is unchanged with respect to π rotations about the a,b,and c axes (C_1,C_2 and C_3) , as well with reflections across the ab,ac and bc planes (σ_{ab},σ_{ac} and σ_{bc}) and with respect to inversion about the center of mass

Representation	E	C_1	C_2	C_3	σ_{12}	σ_{13}	σ_{23}
$A_{g,u}$	1	1	1	1	1	1	1
$B_{1g,u}$	1	1	-1	-1	-1	-1	1
$B_{2g,u}$	1	-1	1	-1	-1	1	-1
$B_{3g,u}$	-1	- 1	1	1	1	-1	-1

Table D.1: *Character table for the D_{2h} point group*

(a product of a π rotation about the a-axis and reflection across the bc plane). Together these form the point group D_{2h}, for which table D.1 is the character table where g and u represent even or odd symmetry with respect to the inversion operation. The electronic wave function must generate one of the irreducible representations of D_{2h}. Invoking the Hatree-Fock approximation the total electronic wave function can be decomposed as a product of single electron wave functions symmetrized with respect to permutation to obey the Pauli Exclusion principle. Each molecular orbital must then also generate one of these representations. The orbitals may be constructed using linear combinations of symmetrized orbitals of the carbon and hydrogen atoms. The procedure for the water molecule is detailed in chapter 12 of Bunker and Jensen[49]. For ethylene the ground electronic state configuration is as follows,

$$(1a_g)^2(1b_{1u})^2(2a_g)^2(2b_{1u})^2(1b_{2u})^2(3a_g)^2(1b_{3g})^2(1b_{3u})^2, {}^1A_g. \tag{D.1}$$

where small letters indicate the symmetry of an orbital and the superscripts the number of electrons occupying the orbital. The number preceding the symmetry label differentiates symmetries that occur more than once, and the orbitals are given in order of increasing energy. The energy ordering is not trivial to determine and requires numerical simulation.

${}^1A_g$ represents the total ground state symmetry and the superscript the total spin ($2S+1$, $S = 0$ since there are no unpaired electrons). The total symmetry can be determined by considering the effect each symmetry operation has on the product wave function. For instance, let us consider the effect of the operation C_2. One of the electrons in the highest occupied molecular orbital (HOMO) will contribute a minus sign to the product, however

this will be nullified by the other electron occupying the same orbital. Similarly, since all the orbitals are doubly occupied none of them will contribute a minus sign to the product under C_2 or any other group operation, giving a total symmetry of A_g. Therefore, if one electron is removed the total symmetry changes. In general the states of the ion must be written as a superposition of all possible configurations of the neutral missing one electron, and the relative weight of the configuration is decided by the ionic Hamiltonian. However, in many cases as in ethylene a single configuration is dominant for each ionic state, and all other configurations can be neglected (this is called Koopman's approximation[44]). The ground state of $C_2H_4^+$ results from the removal of a single HOMO electron, thus inheriting the symmetry of the unpaired electron resulting in the $\tilde{X}\ ^2B_{3u}$ state. Similarly the first excited state is $\tilde{A}^2B_{3g}$ (removal of HOMO-1 electron) the next is $\tilde{B}^2A_g$ (removal of HOMO-2 electron) and so on.

Finally we would like to note that the point group for neutral ethylene and the ion in the ground state are *not* the same. In the ionic ground state the molecule is twisted about the C=C bond by an angle of approximately 25°[136] reducing the symmetry to D_2, the same as for the asymmetric rotor Hamiltonian. This keeps the rotational symmetry the same, but the labels g and u corresponding to inversion must be dropped. However since convention has been to keep the inversion labels[98,105], we do the same here.

Appendix E

Abel inversion using pbasex

The projection of a three dimensional cylindrically symmetric distribution onto a plane is described by the Abel transformation. Labeling the symmetry axis as z and the cylindrical radius as ρ, the projection of a distribution $f(z, \rho)$ is given by

$$P(x, z) = \int_x^\infty \frac{F(z, \rho)\rho d\rho}{\sqrt{\rho^2 - x^2}}. \tag{E.1}$$

In a VMI measurement with only linearly polarized pulses, the laser polarization axis is the symmetry axis and the measured velocity distribution corresponds to $P(x, z)$. In this case the above expression can be inverted to retrieve the central slice $F(z, \rho)$ of the 3D velocity distribution. We use the pbasex algorithm to perform this inversion[110]. In this algorithm F is expanded in a spherical basis set,

$$\begin{aligned} F(R, \theta) &= \sum_{k,l} c_{k,l} f_{k,l}(R, \theta), \\ f_{k,l}(R, \theta) &e^{\frac{-(R-R_k)^2}{\sigma}} P_l(\cos\theta). \end{aligned} \tag{E.2}$$

where R and θ are the spherical radius and polar angle and are related to the cylindrical coordinates by the expressions

$$\begin{aligned} R^2 &= \rho^2 + z^2, \\ \theta &= \tan^{-1}(\frac{z}{\rho}. \end{aligned} \tag{E.3}$$

The $c_{k,l}$ are expansion coefficients to be determined from the measurement. Each basis function $f_{k,l}$ is a Gaussian in R centered at R_k with width σ and a Legerndre Polynomial in θ of order l. Inserting Eq. E.2 into the Abel integral gives,

$$\begin{aligned} P(x,z) &= \sum_{k,l} c_{k,l} g_{k,l}(x,z), \\ g_{k,l}(x,z) &= \int_x^\infty \frac{f_{k,l}(z,\rho)\rho d\rho}{\sqrt{\rho^2 - x^2}}. \end{aligned} \tag{E.4}$$

where the basis functions are rewritten in cylindrical coordinates using the relations E.3. After numerically calculating the $f_{k,l}$ on a uniform (z,ρ) grid we perform the Abel integral numerically to get the $g_{k,l}$. The (x,z) coordinates are contracted to convert the measured image, a 2D matrix, into a 1D vector. Contracting the (k,l) into a single index allows the set of $g_{k,l}(x,z)$ to be expressed as a 2D matrix resulting in a matrix equation with the $c_{k,l}$ representing an unknown vector — $\hat{G}\vec{c} = \vec{p}$. This equation can be solved in numerous ways, one of which is presented in chapter 5.

Appendix F

Asymmetric Top Codes

Two numerical codes were written in C++ to solve the TDSE for the work presented in this thesis — one for the asymmetric rigid rotor in a linearly polarized pulse and another for the asymmetric rigid rotor in an elliptically polarized pulse. While there are significant difference between the two, some general aspects are the same and these will be discussed first.

F.1 General Layout of the Codes

The initial part of each code initializes numerous variables used throughout. These include integers intended for use as loop indices and strings intended for use as file names. Then an input file is read to assign values to laser parameters (intensity and pulse duration) and molecular constants (the inertia and polarizazbility tensors and spin statistical weights). Additionally, the rotational temperature, step size and time window for the calculation during and after the pulse are also read from the input file. After being read all these parameters are converted to atomic units.

Since the asymmetric top Hamiltonian cannot be diagonalized analytically, both codes first numerically diagonalize it to get the energies and eigenvectors. Each J manifold is

independently diagonalized as J and τ are looped over and the energies and eigenvectors are saved in 1D and 2D arrays respectively.These arrays are indexed such that the index i runs from 0 to n, n being the number of array elements, as J runs from 0 to J_{max} and K runs from $-J$ to J for each J. This requires that $i = J^2 + J + K$.The value of n (size of the array) is determined by running the same loop (over J and τ) at the top of the program which increments a dummy integer for each loop iteration, the final value of the integer giving the required array size. A function ('Asymmetric Top Hamiltonian.cpp') is used to compute the matrix elements of the field free Hamiltonian using the expression provided by Zare[50](chapter 6 pg. 272), and the matrix is diagonalized using a subroutine from *Numerical Recipes in C++*[54] ('eigen_symm.h').

As the energies and eigenstates are calculated and the corresponding arrays filled, two additional arrays – Jsort and Tausort — are filled. These keep track of the J and τ value that correspond to each array position. The symmetry label of each J,τ state is also determined in this loop using the scheme detailed in chapter 2.

Next the energy array is sorted in ascending order using Numerical Recipe's 'sort.h' routine. The routine also keeps a track of the array positions of the elements before sorting, so the appropriate vales of J and τ can be read from the Jsort and Tausort arrays. The partition function is calculated using the sorted array and the highest energy rotational state is determined for the given temperature using the method detailed in chapter 2. The TDSE is then solved for each state up to the highest energy state in the distribution.

To solve the TDSE we once again use a routine from Numerical Recipes. However, since this routine applies only to real numbers, the coupled equations 2.17 must be separated into real and imaginary parts. Writing $a_{JKM} = x_{JKM} + iy_{JKM}$, gives the following set of equivalent coupled equations

$$\begin{aligned}
\dot{x}_{JKM} &= \sum_{K'} y_{JK'M} H_{K,K'} + \sum_{J'K'M'} y_{J'K'M'} \langle JKM|V(t)|J'K'M'\rangle \,, \\
\dot{y}_{JKM} &= -\sum_{K'} x_{JK'M} H_{K,K'} - \sum_{J'K'M'} x_{J'K'M'} \langle JKM|V(t)|J'K'M'\rangle \,.
\end{aligned} \tag{F.1}$$

The array of values a_{JKM} are indexed such the even indices correspond to the real parts and the odd indices to the imaginary parts.

These coupled differential equations are solved by a Numerical Recipes fifth order Dormand-Price (DP) stepper. However, before entering the TDSE loop the logic of 1D and 3D codes diverge, therefore we must deal with them independently from here on.

F.2 1D Code(s)

Before entering the time loop an empty array the size of the number points in the field, and another with size equal to the number of field free points are initialized. The arrays, named c2t and c2tfree are intended to save $\langle \cos^2\theta \rangle$ at each time. Another version of this code (HHGfitbeocat.cpp) instead defines numerous arrays named Djk with the same size, each to save the $\left\langle D^j_{0,k} \right\rangle$ at each time up to j and $k = 8$. Yet another version (angledist.cpp) is written to calculate the molecular axis distribution $\rho(\theta, \chi, t)$.

$\langle \cos^2\theta \rangle$ and $\left\langle D^j_{0,k} \right\rangle$ are calculated using Eq. 2.22 and expressions for their matrix elements, Eq. A.7 and Eq. A.4 respectively. $\rho(\theta, \chi, t)$ is calculated from the wavefunction (cf. Eq. 5.6), which in turn is expanded as Wigner matrix elements (cf. Eq. 2.9). These functions are pre-calculated using the function available in *Mathematica* on a 20×20 $\{\theta \times \chi\}$ grid. The time dependent coefficients are then used to build the molecular axis distribution at each time step. $\langle \cos^2\theta \rangle$ and $\left\langle D^j_{k,m} \right\rangle$ are built from their matrix elements each of which are calculated by functions called at each time step ('c2t.cpp' and 'HHG.cpp' respectively).

The functions used to calculate the matrix elements require computation of the Clebsch-Gordan coefficients. The subroutines 'CGcoeff0.cpp', 'CGcoeffp2.cpp' and 'CGcoeffm2.cpp' compute these for $\Delta J = 2$ and $\Delta K = 0$,2 and -2 respectively. These are used in 'c2t.cpp'. Higher values of $\Delta J, K$ are handled by the subroutine 'ClebschGordan.cpp' which is used in 'HHG.cpp'. Both use expressions from Zare[50] and 'ClebschGordan.cpp' can only deal with values of J up to 86, restricting the largest J_{max} that can be reliably handled to this value.

This in turn puts restrictions on the temperatures and pulse parameters that be handled by the code. These subroutines are used in the 3D code as well.

The time dependent coefficients during the pulse are calculated using the DP stepper. The differential equations F.1 are programmed into a subroutine called 'rhs_asymschrod.cpp'. In this routine each term in the sums on the right side of Eqs. F.1 allowed by the selection rules are written out explicitly and if-else statements ensure that terms with $J' > J_{max}$ or $J' < 0$ are set to zero. The matrix elements of the potential are computed by a function (V Asymmetric Tops CG.cpp) for each loop iteration of the sums and at each time step.

Finally, the code saves each element of the arrays c2t and c2tfree to the same file, or each of the arrays Djk to different files after the entire propagation for a single initial state is complete. The entire time loop is placed within outer loops that loop over initial states (initial J, τ and M values) up to the highest energy state at the input temperature. The first row of each file is the time in picoseconds. The array elements are also weighted by the correct nuclear spin and Boltzmann weights. The rows of the saved files then need to be summed to generate a thermally averaged trace.

F.3 3D Code

The 3D code is written in such a manner that it can be run for a train of pulses, each of which can have any ellipticity. The peak position in time of each pulse and the ellipticity need to be included in the input file, 'multidata.dat', along with the duration and intensity. The thermal statistics and diagonalization of the rigid rotor Hamiltonian are performed in a manner identical to the 1D code. However, before these are performed the time array 'tval' is defined and saved using an if-else statement. 'tval' is incremented in a loop by the field free step size (an input value) for each increment of the loop index – 'i' — until the start time of a pulse is reached (this is defined as the central position of the pulse minus twice the pulse duration). At the start time the 'else' statement is implemented which steps 'tval'

by the in-field step size in a loop over the number of points in the field. 'i' is then stepped by the number of in-field points and 'j' by 1. 'i' therefore is the time index and 'j' the pulse number.

Another improvement made to the 3D code is that the potential matrix, and all matrices of quantities for which expectation vales are calculated — $\langle \cos^2 \theta_{xX} \rangle$, $\langle \cos^2 \theta_{yY} \rangle$, $\langle \cos^2 \theta_{zZ} \rangle$ and $\langle \cos^2 \delta \rangle$ — are calculated outside the time propagation loop. Each of these quantities are represented by 1D arrays that are initialized with zeros and are filled in nested loops running over $\{J,J',K,K',M,M'\}$. The loops are stepped such that selection rules are taken into account and array indices for matrix elements that are zero are skipped. Matrix elements with $J' > J_{max}$ or $J' < 0$ are skipped as well. A dummy index stepped by 1 for each inner most loop iteration is used to keep track of the angular momentum indices associated with each array element.

Open multi-processing (openMP) is implemented as well.The time loop for each initial state is run independently over a number of processors greatly speeding up the calculation. This implementation most crucially involves designating variables that cannot be accessed by all processors simultaneously as 'private'. In our case these are any array indices that are looped. Since a copy of the loop is run on each processor, memory requirements for the code can be quite large (usually >20 GB RAM for realistic temperature and pulse parameters). The number of processors to be used is an input parameter for the code. The differential equations F.1 are programmed into a subroutine called 'rhs_asymschrod 3d 4.cpp'. This is also done using the same loop structure as for the potential and cosine matrices, precluding the writing of each term in the sums explicitly since the loop itself accounts for the selection rules.

The expectation value calculations also use the same loop structure, however for these and the differential equations an array index is required that increments by 1 as J runs from

0 to J_{max} and K and M run from $-J$ to J. Such an index i is given by,

$$i = \frac{1}{3}(4J^3 + 6J^2 + 5) + M(2J + 1) + K. \tag{F.2}$$

Once the expectation values are calculated they are saved to file in the same manner as in the 1D code, with each expectation value being saved to a different file.